FERMILAB-THESIS-2007-100

# Study of the $t\bar{t}$ in the dilepton channel at $\sqrt{1.96}$ TeV with the Collider Detector at Fermilab

A dissertation presented
by

Victoria Giakoumopoulou

to
The Department of Physics
in partial fulfillment of the requirements
for the degree of
Doctor of Philosophy
in the subject of

Nuclear and Elementary Particle Physics

University of Athens
Athens, Greece
October 2007

Doctoral comitee
Associate Professor Nikolaos Giokaris
Professor Nikolaos Antoniou
Professor Constantinos Papanikolas

# Abstract

This study presents new measurement of the top quark mass in the $t\bar{t}$ to the dilepton decay channel. It is based on the observed linear dependence of the top mass to the transverse momentum $P_T$ of the leptons that are two of the final products of the top-antitop pair decay. It uses data collected by the CDF detector from December 2004 to March 2007 that correspond to an integrated luminosity of 1.8 $fb^{-1}$ .

Two independent and mutually compatible methods have been implemented for this reason, both depending on the leptons' $P_T$. The first method, called the "Straight Line", exploits just the linear relation between the leptons' $P_T$ and the top mass. With the second one, called the "Likelihood", the full $P_T$ spectrum is modeled by an analytical function and the top mass is estimated using the likelihood minimization procedure. A top quark mass of $m_{top}=156\pm20_{(stat)}\pm4.6_{(syst)}$ GeV/$c^2$ is obtained with the Likelihood method and of $149\pm21_{(stat)}\pm5.0$(syst) GeV/$c^2$ is obtained with the Straight Line one.

This study is complementary to other CDF mass studies in the dilepton channel. It differs by the fact that is not dependent on the jets and does not use the b quark secondary vertex b-tagging technique. It is therefore not dependent on the jet energy scale uncertainty that is at this moment the biggest systematic contribution to all other methods.

This method is a simple and straightforward method that aims to a small systematic uncertainty. The statistical uncertainty is still not competitive with respect to the other methods, due to the relatively small sensitivity of the leptons' $P_T$ to the top mass. On the other hand, this study is a very good preview of the method with the upcoming LHC data, where the statistical error is expected to be greatly suppressed. The dominating error will then be the systematic one and this method promises to be

competitive or even better, regarding this point, with respect to the other methods.

# Contents

# List of Figures

# List of Tables

# Acknowledgments

The years that I devoted to my doctoral study have offered me an unforgettable and fascinating experience. It was more than once that I believed that I was lost and I that would never see the "light" again, but finally always something was happening and the "solution" was suddenly appearing, right there on the screen of my laptop! Those were the moments that filled me with happiness and satisfaction and showed me that research is actually what I love. The work during my study was a really learning experience. It taught me how to work with other people, to fight for what I want but also to compromise, to face problems that I had no idea how to treat, to write down my ideas, to give talks. But above all it made me learn a lot of things about myself and realize that it takes a lot of effort and patience to reach goals that may seem inaccessible.

This dissertation would have never been accomplished without the support of my professor Niko Giokari. Prof. Giokaris has always been there for me as a teacher, guiding me in every step, starting from the years that I was just a simple student until now. His deep knowledge of Physics, intuition and novel ideas were always an inspiration for me. But most of all I want to thank him from the bottom of my heart because he has always been encouraging, inspiring and understanding. I also owe sincere acknowledgments to my professors Nikolao Antoniou and Konstantino Papanikola for their support.

I owe sincere thanks to my colleague Konstantino Vellidi, with whom we worked constructively all these years, to make the idea reality. I should also mention here Arkadio Manousaki, as working in the same group with him was an appreciable experience. Also my kind thanks to Thanasi Staveri who was always willing to essentially

help me. I would also like to express my thanks to all the friends that we worked together over the years and mainly to Ariadni Antonaki and Alexi Kalogeropoulo. Finally my thanks to Dimitra Giouroukou, the new blood of our team, for being supportive and thoughtful, wishing her the best of luck.

I would like here to mention my colleagues in CDF. Monica Tecchio that got me involved in the top dilepton cross section analysis. Monica has been very supportive and I owe her much of my knowledge about the dilepton analysis, not to mention the codes she has developed and that we all use in the various CDF dilepton groups. I would also like to thank all the dilepton friends that we still work very harmonically and productively for the top dilepton cross section. So Alexei, Naoki, Dave, Tuula, Yuji, Chang-Seong and Andy thank you all very much. You have all played a very important role in this analysis.

The top and top mass conveners have helped a lot with their comments and interest to bring this analysis to a good result. So sincere thanks to Robin Erbacher, Kirsten Tollefson, George Velev, Nick Van Remortel, Daniel Whiteson but also all the other top enthusiasts that supported this work with their comments.

Most importantly I want to thank my mother Eleni and my brother Christo that always stood next to me, supporting me emotionally and encouraging me to follow my dream. I would not be the person I am without them. And last, but far from least, I want to thank all my good friends that have been next to me. They are always giving me lavishly their love and never get tired hearing me grizzling. Chrysa, all my Christines, Niko and all others who are in my life thank you all.

*Dedicated to the memory of my father*

# Chapter 1

## Introduction

The top quark study is still, 12 years after its discovery, a very stimulating physics topic. It is the most massive elementary particle and its properties are associated to still undiscovered physics, like the existence of the Higgs boson. At this moment two experiments, the Tevatron CDF and D0, work intensively to measure as precisely as possible its properties [1], [2]. Many groups have produced precise measurements of the top quark mass and of the $t\bar{t}$ cross section, that are consistent to the Standard Model theoretical predictions [3], [4]. Furthermore the single top production, that is theoretically predicted, is close to be discovered. The upcoming LHC will literally be a factory of top quarks, producing thousands every year. So still fundamental questions related to the Standard Model like the mass hierarchy and the electorweak symmetry breaking [5] [6] [7] are expected to be resolved.

This dissertation presents a measurement of the top quark mass in the dilepton channel. It uses data selected by the CDF detector corresponding to 1.8 $fb^{-1}$ integrated luminosiy. The top quark mass is measured using only the lepton's $P_T$ information as proposed in [8]

The leptons' $P_T$ is a variable that can be measured very well in the tracker and the calorimeter and can be accurately calibrated against $Z \rightarrow$ dilepton decays. Jets have a minimal involvement in this analysis, i.e. only in the criteria used for the event selection. Therefore the top quark mass as extracted through this method, is not sensitive to the jet energy scale JES uncertainty. The $P_T$ is a simple variable that is common for the dilepton (DIL) and the Lepton+Jets (LJ) channels, a fact that gives the opportunity to combine results but also compare the two channels. A similar measurement has been presented and approved by the CDF for the Lepton+jets channel using 340 $pb^{-1}$ of data [9].

Section 2 describes the Standard Model physics. It concentrates on the properties of the top quark and reviews the measurements of the top mass and the $t\bar{t}$ decay cross section from the different CDF and D0 groups. Finally it introduces the methods that are used for the measurement of the top quark mass in the dilepton channel using the leptons' transverse momentum. Section 3 describes the Tevatron $p\bar{p}$ accelerator system and the subdetectors that form the CDF apparatus. Finally there is also a description of the CDF triggering system.

The following 5 sections discuss the analysis. In detail, section 4 reviews the $t\bar{t}$ to dilepton event selection and the data and Monte Carlo samples that are used for this analysis. Section 5 describes the background studies that are performed and the number of background events that are expected for the given integrated luminosity. Section 6 explains the sensitivity of the leptons' transverse momentum to the top mass. It describes the two independent but mutually compatible methods that are used for measuring the top quark mass. Section 7 discusses the statistical tests

that were performed to assure the validity of the methods. Section 8 discusses the systematic uncertainties that are involved in the methods.

Finally in section 9 the final results of this method are presented and section 10 discusses the conclusions.

# Chapter 2

## The Standard Model and the Top Quark

This chapter describes the Standard Model and the physics of the top quark.

## 2.1 The Standard Model

The Standard Model of the Particle Physics is the theory that describes all the known elementary particles and their electroweak and strong interactions. This model is a combination of the quantum chromodynamics theory [10] [11] and the theory of the eloctroweak interactions of Glashow-Salam-Weinberg (GSW) [5] [6] [7]. The quantum chromodynamic theory describes the strong force and is represented by the SU(3) gauge group. The electoroweak theory describes the weak and electromagnetic forces and is represented by the SU(2)xU(1) gauge group. Therefore the Standard Model is locally invariant under transformations of the group:

$$G = SU(3) \times SU(2)_L \times U(1)_Y \tag{2.1}$$

The Standard Model consists of three families of fundamental fermions with spin $\frac{1}{2}$ and increasing mass. Each family consists of a pair of leptons and a pair of quarks.

The lepton interactions are mediated by the electorweak force though the quark interactions are mediated both by the electroweak and the strong forces. The leptons are combined into three generations, each one consisting of a charged lepton (e, $\mu, \tau$) and its correspondig neutrino ($\nu_{\mathrm{e}}, \nu_{\mu}, \nu_{\tau}$).

$$\begin{pmatrix} \nu_e \\ e \end{pmatrix} \begin{pmatrix} \nu_\mu \\ \mu \end{pmatrix} \begin{pmatrix} \nu_\tau \\ \tau \end{pmatrix}$$

The quarks respectively are combined in three generations of one quark with charge $+\frac{2}{3}e$ and one with $-\frac{1}{3}e$.

$$\begin{pmatrix} u \\ d \end{pmatrix} \begin{pmatrix} c \\ s \end{pmatrix} \begin{pmatrix} t \\ b \end{pmatrix}$$

Taking into consideration that the quarks interact with the strong nuclear forces, they cannot be individually observed but are confined with other quarks inside hadrons that are chromatically neutral. The hadrons consist of mesons (quark - antiquark pairs) and baryons (three quark particles).

All force carriers are bosons (spin 1 particles) and are described by the Standard Model: the photon $\gamma$ for the electromagnetic force, the $W^{+/-}$ and the Z for the weak force and the gluon for the strong force.

The Standard Model describes successfully all of the interactions referred to above. Moreover, many of its predictions have been confirmed with remarkable accuracy. However, in order for the symmetry described in 2.1 to be exact, the W and Z bosons should be massless. In order for the Standard Model to be consistent with the very large boson masses there should be a spontaneous symmetry breaking, that would also explain the mass hierarchy of the fermions. The so called electroweak symmetry

breaking (EWSB) can take place within the SM through the introduction of a scalar field, the Higgs field that is associated with the existence of a heavy Higgs boson [12].

The existence of the Higgs boson has not been experimentally confirmed yet. Nowadays the discovery of the Higgs boson is one of the most exciting challenges in High Energy Physics. Direct searches at LEP set a lower mass limit at $M_{Higgs} = 114\,GeV/c^2$ with 95% confidence level [13]. Of particular interest is the constraint of the Higgs mass from precision measurements of the top quark mass and the W boson mass, as these quantities are sensitive to $lnM_H$ as shown in Figure 2.1.

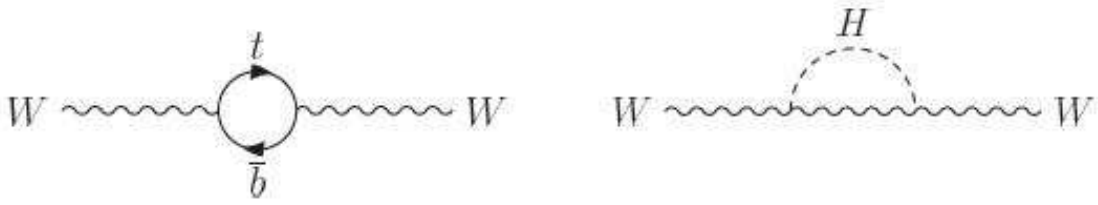


Figure 2.1: W boson mass corrections via loop diagrams where (a) in the fermion loop the top quark mass dominates as it is proportional to $M^2_{top}$ and (b) the Higgs boson loop contributes a correction proportional to $lnM_H$

Figure 2.2 shows the most recent measurements (March 2007) of the W boson mass. The top red values show the direct measurements and the bottom blue values are the indirect constrains valid within the Minimal Standard Model. Separately shown is the recent measurement from the NuTeV collaboration, based on the ratio of neutral current to charged current reactions in neutrino-nucleon scattering. Figure 2.3 illustrates the $\Delta\chi^2$ curve derived from high $Q^2$ precision electroweak measurements at LEP, SLD, CDF and D0, as a function of the Higgs mass. The most probable value, corresponding to the minimum of this curve, is $M_H = 76^{+33}_{-24}$GeV at 68% confidence level, where the error is experimental. For this estimation the theoretical uncertainty,

shown as the blue band, was not taken into account.

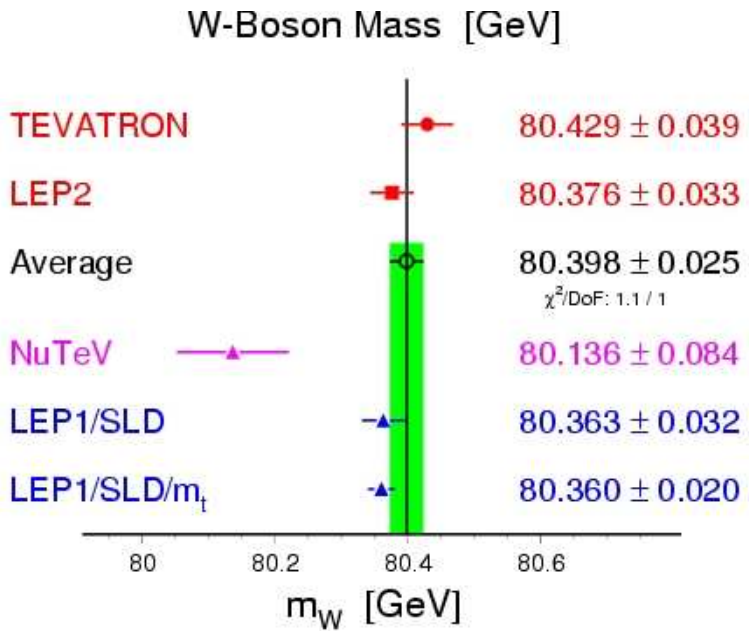


Figure 2.2: W boson mass from direct measurements (red values), indirect constraints valid within the Minimal SM (blue values) and from the NuTeV (pink value)

While this is not a proof that the Higgs boson actually exists, it provides a guideline in what mass range it may lie. Furthermore it makes it very important to also measure the top mass as precisely as possible as its mass is tightly connected to the Higgs mass.

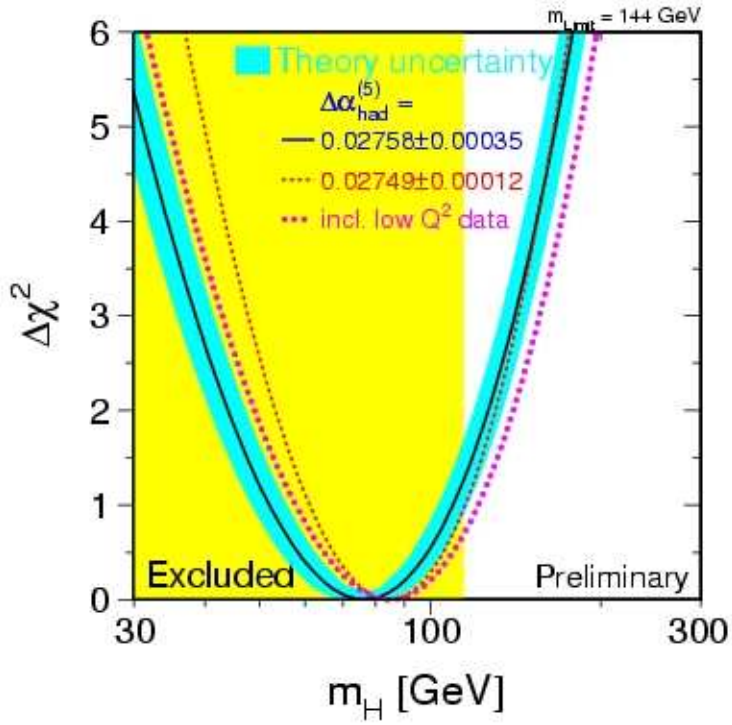


Figure 2.3: $\Delta\chi^2$ curve derived from precision measurements at LEP, SLD, CDF and D0, as a function of the Higgs mass. $M_{Limit}$114 GeV is the LEP-2 direct search limit.

## 2.2 The Top Quark

The Fermi National Laboratory announced the discovery of the top quark in 1995, both from the CDF and the D0 experiments [1], [2]. It was the last undiscovered quark, of the six predicted by the Standard Model, since the b quark discovery in 1977. The top is the third generation quark with charge +2/3e and is by far the most massive of all the known fundamental particles. Its mass is currently measured at 170.9±1.8 GeV/$c^2$ (Figure 2.4) [3] nearly as heavy as a gold nucleus. It interacts primarily by the strong interaction but can only decay via the weak force. It decays almost exclusively to a W boson and a b quark. The Standard Model predicts its life time to be roughly $10^{-24}$ sec. The CDF has recently presented the first direct limit in the top quark lifetime at $c\tau$ <52 $\mu$m at 95% CL [14].

### 2.2.1 Top Quark Production

The top quark is primarily produced in hadron colliders via strong interactions. It is mostly produced in pairs according to the QCD processes quark-antiquark annihilation $q\bar{q} \rightarrow t\bar{t}$ and gluon fusion $gg \rightarrow t\bar{t}$ as seen in Figure 2.5. Though the single top production is predicted in the standard model, there was not significance evidence of its existence [15],[16],[17]. The analysis reported so far are very close to achieve a 3 sigma evidence.

In Tevatron energy of $\sqrt{s}$ = 1.96 TeV, the most recent combined $t\bar{t}$ production cross section is measured to be $7.32 \pm 0.85$ pb for a top mass of 175 GeV/$c^2$ (Figure 2.6) [4]. Figure 2.7 illustrates the calculation of the $t\bar{t}$ cross section as a function of the top mass for $p\bar{p}$ collision for Tevatron center of mass energy $\sqrt{s} = 1.96$ TeV. The

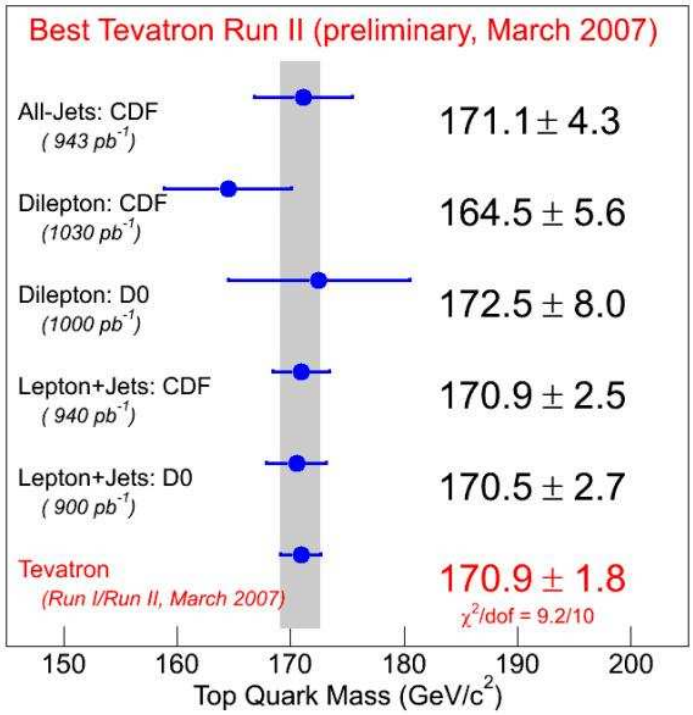


Figure 2.4: A summary of the top mass measurements in Tevatron

NLO theoretical prediction is $\sigma_{t\bar{t}}^{NLO} = 6.7^{+0.7}_{-0.9}$ pb for $M_{top}$=175 GeV/$c^2$ [18].

### 2.2.2 Top Quark Decay

With a top mass greater than the Wb threshold the dominating decay channel is $t \rightarrow Wb$. For the top decay the final Ws and Wd states are considered suppressed with respect to the Wb with the square of the $V_{ts}$ and $V_{td}$ elements of the CKM matrix [19]. Because of its large mass it decays before hadronizing. The b quark from the top decay hadronizes and is identified as a jet and the W boson decays either to a $q\bar{q}$ pair or to lepton and a neutrino (Figure 2.8). Therefore there are 81 possible final states (Figure 2.9) and can be categorized into 3 groups, forming the three $t\bar{t}$

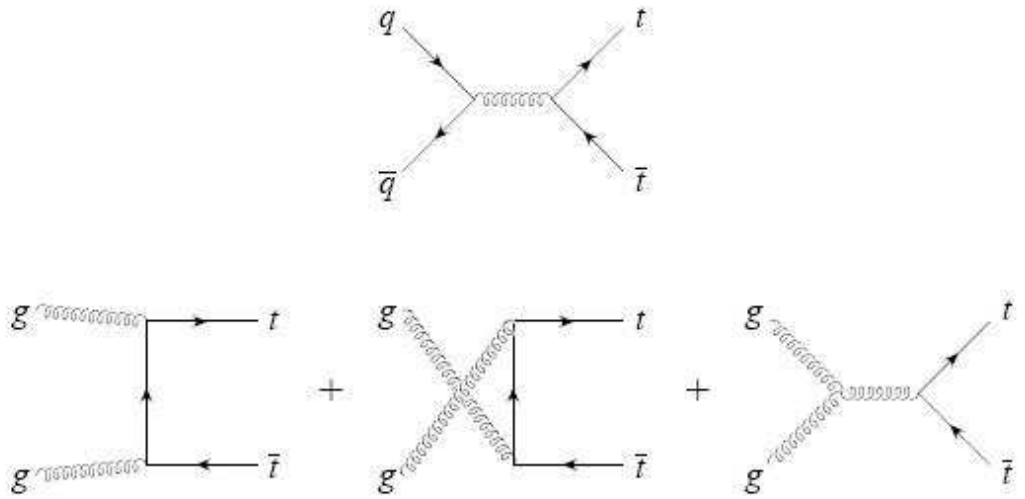


Figure 2.5: Top quark production at hadron colliders.

decay channels.

In the all hadronic channel both W bosons decay to quarks 44.4% of the $t\bar{t}$ decays. In this channel there are six quarks in the final state, four of which come from the hadronic decays of the W bosons and two from the b quarks. The $W^+$ may decay to $u\bar{d}$ or $c\bar{s}$ and the $W^-$ may decay to $\bar{u}d$ or $\bar{c}s$. As each quark may have three color possibilities, the total number for final states for the all hadronic channel is 36. Though this channel has a large branching ratio, it is not favored for precision studies due to its large QCD background.

In the lepton+jets channel the one W decays to a lepton and a neutrino and the other to a pair of quarks. In the final state one expects to observe a lepton, at least four quarks -two from the W decay and two from the b quarks- and large missing

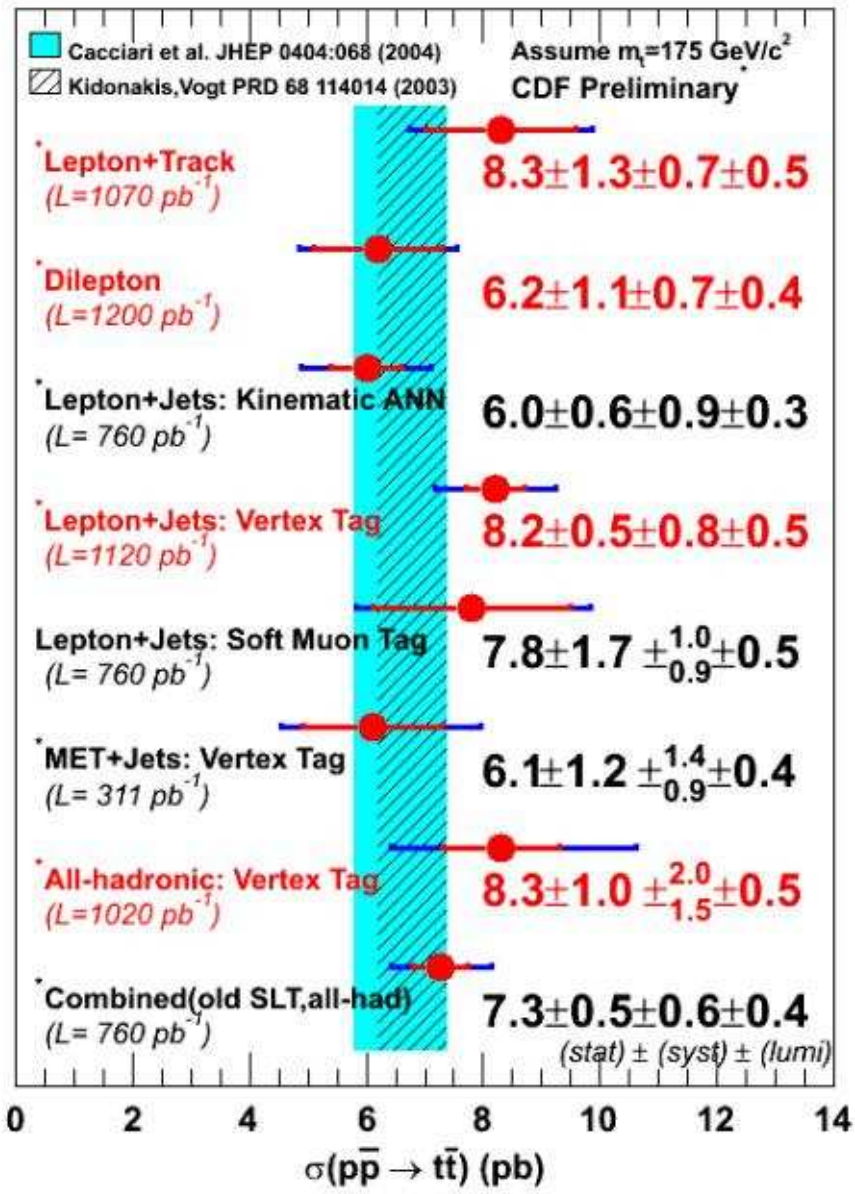


Figure 2.6: A summary of the $t\bar{t}$ cross section measurements in CDF.

transverse energy because of the escaping neutrino. Approximately 44.4% of the $t\bar{t}$ decays are in this channel.

In the dilepton channel both of the W bosons decay to a lepton and a neutrino.

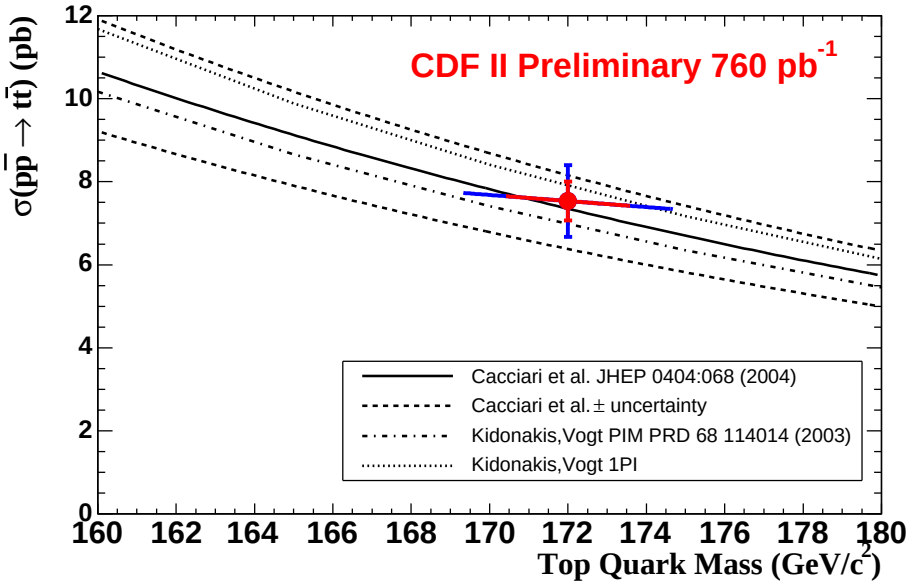


Figure 2.7: Calculation of the $t\bar{t}$ cross section as a function of the top quark mass. The calculation is for $p\bar{p}$ collision for Tevatron energy. The CDF measurement is also shown for comparison

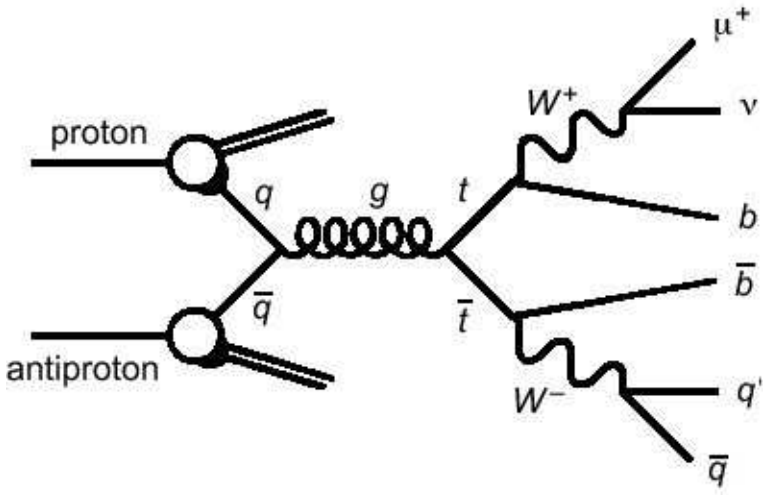


Figure 2.8: Decay of the $t\bar{t}$

The signature of this channel is two leptons with large transverse momentum, two jets from the b quarks and large missing transverse momentum from the two escaping

| Decay channel | $t \to W^+ b$ | $\bar{t} \to W^- \bar{b}$ | Possible states | Total possibility |
|---|---|---|---|---|
| All Hadronic | $u\bar{d}$ | $\bar{u}d$ | 9 | 44.4% |
| | $u\bar{d}$ | $\bar{c}s$ | 9 | |
| | $c\bar{s}$ | $\bar{u}d$ | 9 | |
| | $c\bar{s}$ | $\bar{c}s$ | 9 | |
| Lepton+jets | $u\bar{d}$ | $l\bar{\nu}$ | 9 | 44.4% |
| | $c\bar{s}$ | $l\bar{\nu}$ | 9 | |
| | $\bar{l}\nu$ | $\bar{u}d$ | 9 | |
| | $\bar{l}\nu$ | $\bar{c}s$ | 9 | |
| Dilepton | $e^+$ | $e^-$ | 1 | 11.2% |
| | $e^+$ | $\mu^-$ | 1 | |
| | $e^+$ | $\tau^-$ | 1 | |
| | $\mu^+$ | $\mu^-$ | 1 | |
| | $\mu^+$ | $e^-$ | 1 | |
| | $\mu^+$ | $\tau^-$ | 1 | |
| | $\tau^+$ | $\tau^-$ | 1 | |
| | $\tau^+$ | $e^-$ | 1 | |
| | $\tau^+$ | $\mu^-$ | 1 | |
| | | | 81 | 100% |

Figure 2.9: Possible final states of the $t\bar{t}$ decay

neutrinos. This channel has a branching ratio of about 11.2%. The final states involve all the possible combinations between the three lepton types. In this study only events where the leptons are electrons or muons are selected, a fact that reduces the probability to 5%. Combinations that involve the tau lepton are excluded, as the tau has a very short life time and decays quickly to lighter leptons or hadrons. This channel has the smallest background but comes short because of the large missing $E_T$ and the small branching ratio.

Observation of $t\bar{t}$ pairs has been accomplished in all three channels and the properties of the top quark that have been measured are in general in very good agreement.

### 2.2.3 Top Quark Cross Section

For the TEVATRON energy the NLO theoretical prediction $t\bar{t}$ is $\sigma_{t\bar{t}}^{NLO} = 6.7^{+0.7}_{-0.9}$ pb for $M_{top}$=175 GeV/$c^2$ [18]. The CDF experiment has delivered $t\bar{t}$ cross section measurements in all three decay channels. The most recent published combined result is obtained using the dilepton and lepton+jets channels with 760 $pb^{-1}$ of data [4]. For the dilepton method two high $P_T$ leptons of opposite sign are required, at least two jets and large $\not\!\!E_T$ . The dominant background is associated with jets faking to be leptons. The dominant systematic uncertainty is due to the ambiguity of the number of events from $Z/\gamma*$ decays [20]. For the lepton+jets there are two recent measurements, using artificial neural network technics and secondary vertex b-tags. The cross section measurement using the artificial neural network technique exploits the different kinematics and topology of $t\bar{t}$ and backgrounds from W+jets and QCD multi-jet processes. The major systematic is from the dependence of the leading-order Monte Carlo model for the W+jets background on the scale used to evaluate the strong coupling constant $a_S(Q^2)$ [21]. For the cross section measurement that uses secondary vertex b-tags, displaced secondary vertices are reconstructed to identify b-jets. With this method the W+jets background is greatly suppressed. The b-tagging efficiency for W events with 3 or more jets is 60%. The dominant systematic uncertainty for this method is associated with the uncertainty on the b-tagging efficiency, followed by the uncertainty on the W+heavy flavor, mis-tag and QCD muilti-jet backgrounds [22]. For the combined result also older CDF measurements were used and the cross section measured is $7.32 \pm 0.85$ pb for a top mass of 175 GeV/$c^2$. More recent individual cross section measurements, using richer in luminosity samples present more

accurate measurements [23], [24], [25], [26].

### 2.2.4 Top Quark Mass

One of the more important reasons to perform precise top mass measurements is that the top mass along with the W mass can be used to give a production for the SM Higgs mass. Therefore the better we know the top mass the better we can localize the Higgs mass. Until now, top mass measurements have been performed only in the CDF and D0 Tevatron experiments. The accuracy of these measurements is limited by the respectively low cross section of the top pair production in the Tevatron energies. This problem will be overcome when the LHC experiments will start taking data. In the LHC energies, millions of top pairs will be produced, suppressing the statistical error. The dominating error will therefore be the systematic one.

In CDF and D0 top mass measurements have been delivered in all three $t\bar{t}$ decay channels. The most precise measurements until now are derived from the lepton+jet channel due to its large branching ratio and modest background. The dilepton channel has provided also very precise measurements, compensating the lower statistics with the better signal/background ratio. The most dominant systematic uncertainty in all the channels is associated with the measurement of the jet - jet energy scale. In the dilepton channel the top mass measurement faces additional difficulties because of the presence of the two neutrinos. The neutrinos are not measured in the detector as it appears only as $\not{E}_T$ . The kinematic final state of the $t\bar{t}$ can not be reconstructed using the measured quantities.

At the time of this writing the official combined top mass measurement, using 1

fb$^{-1}$ of data, is 170.9±1.8 GeV/c$^2$ (Figure 2.10) [3]. This includes measurements both from the CDF and D0 experiments, for all three channels. The dominating error as seen from Figure 2.11 is the total jet energy scale uncertainty. One can also observe that there is a tendency for the dilepton top mass measurements to be lower than the ones estimated in the lepton+jet and all hadronic channels, but still all the measurements are within the quoted uncertainty.

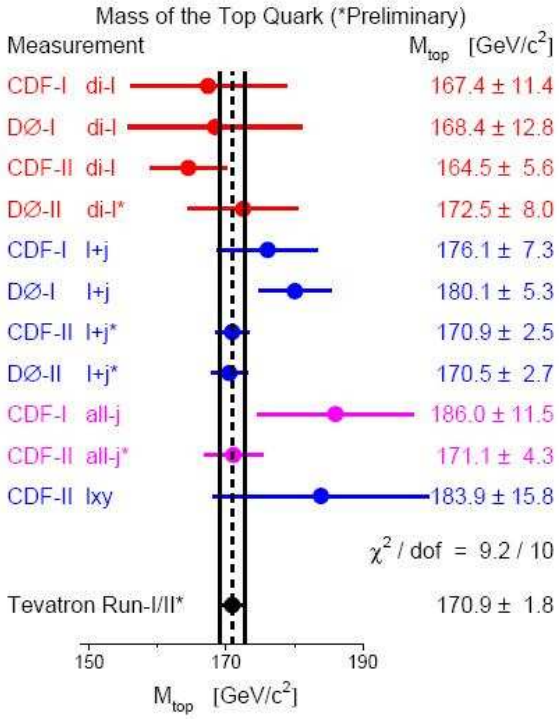


Figure 2.10: Summary of the top mass measurements resulting to the world average

As seen from the figures above both experiments have developed various methods for measuring the top mass. The best single measurement in the world provides a top mass with an accuracy of 1.5%, using 940 pb$^{-1}$ of data [27]. This a matrix element analysis in the lepton+jets channel, where at least one jet is identified as

| | Run-I published | | | | | Run-II preliminary | | | | | |
|---|---|---|---|---|---|---|---|---|---|---|---|
| | CDF | | | DØ | | CDF | | | | DØ | |
| | all-j | l+j | di-l | l+j | di-l | l+j | di-l | all-j | lxy | l+j | di-l |
| Lumi ($fb^{-1}$) | 0.11 | 0.11 | 0.11 | 0.13 | 0.13 | 0.9 | 1.0 | 1.0 | 0.7 | 0.9 | 1.0 |
| Result | 186.0 | 176.1 | 167.4 | 180.1 | 168.4 | 170.9 | 164.5 | 171.1 | 183.9 | 170.5 | 172.5 |
| iJES | 0.0 | 0.0 | 0.0 | 0.0 | 0.0 | 1.4 | 0.0 | 2.4 | 0.0 | 0.0 | 0.0 |
| aJES | 0.0 | 0.0 | 0.0 | 0.0 | 0.0 | 0.0 | 0.0 | 0.0 | 0.0 | 0.6 | 2.0 |
| bJES | 0.6 | 0.6 | 0.8 | 0.7 | 0.7 | 0.6 | 0.6 | 0.4 | 0.0 | 0.5 | 1.8 |
| cJES | 3.0 | 2.7 | 2.6 | 2.0 | 2.0 | 0.0 | 2.8 | 0.0 | 0.0 | 0.0 | 4.3 |
| dJES | 0.3 | 0.7 | 0.6 | 0.0 | 0.0 | 0.2 | 1.6 | 0.0 | 0.0 | 1.6 | 1.9 |
| rJES | 4.0 | 3.4 | 2.7 | 2.5 | 1.1 | 0.0 | 1.3 | 0.0 | 0.3 | 0.0 | 0.0 |
| Signal | 1.8 | 2.6 | 2.8 | 1.1 | 1.8 | 1.1 | 0.9 | 1.3 | 1.4 | 0.6 | 0.7 |
| BG | 1.7 | 1.3 | 0.3 | 1.0 | 1.1 | 0.2 | 0.7 | 1.0 | 2.3 | 0.3 | 0.6 |
| Fit | 0.6 | 0.0 | 0.7 | 0.6 | 1.1 | 0.4 | 0.9 | 0.7 | 4.8 | 0.4 | 0.9 |
| MC | 0.8 | 0.1 | 0.6 | 0.0 | 0.0 | 0.2 | 0.9 | 1.0 | 0.7 | 0.0 | 0.0 |
| UN/MI | 0.0 | 0.0 | 0.0 | 1.3 | 1.3 | 0.0 | 0.0 | 0.0 | 0.0 | 0.0 | 0.0 |
| Syst. | 5.7 | 5.3 | 4.9 | 3.9 | 3.6 | 1.9 | 3.9 | 3.2 | 5.6 | 2.0 | 5.6 |
| Stat. | 10.0 | 5.1 | 10.3 | 3.6 | 12.3 | 1.6 | 3.9 | 2.8 | 14.8 | 1.8 | 5.8 |
| Total | 11.5 | 7.3 | 11.4 | 5.3 | 12.8 | 2.5 | 5.6 | 4.3 | 15.8 | 2.7 | 8.0 |

Figure 2.11: Summary of the top mass systematic uncertainties used for the world average

b quark. Various top mass measurements have been presented up to this moment, exploiting 1.8 $fb^{-1}$ of available data, all resulting to consistent measurements and very compelling systematic uncertainties. Many of the mass measurement analysis are based on template methods, where the top mass is reconstructed using various methods. The top mass analysis that is presented in this thesis is also a template method in the dilepton channel. As it will be described in the next section the method that will be described tries to bypass the problem of the JES uncertainty.

### 2.2.5 Top Quark Mass measurement using the leptons $P_T$

According to what has been demonstrated in the previous section the top mass systematic error is dominated by the jet energy scale uncertainty. This fact was the

main motivation for seeking for a method/variable that does not depend on jet energy scale, does not depend on b-tagging and is the same for both the dilepton and the lepton+jets channels. Such a variable can be the leptons' transverse momentum, a variable that can be measured very well in the tracker and the calorimeter and can be accurately calibrated against Z $\rightarrow$ dilepton decays. Jets have only an indirect involvement in this analysis, i.e. only in the criteria used for the event selection. Therefore the top quark mass as extracted through this method, is not sensitive to JES uncertainty. The $P_T$ is a simple variable that is common for the dilepton (DIL) and the Lepton+Jets (LJ) channels, a fact that gives the opportunity to combine results but also directly compare the two channels.

The $P_T$ of the lepton is sensitive to the top mass. There is a linear dependence between the two variables [8]. Investigating all the possibilities in the dilepton channel, it can be found that also other lepton kinematic variables are linearly dependent to the top mass, as the $P_T$ of the leading lepton, the invariant mass $M_{inv}$ of the two leptons, the momentum P of the leptons, the sum of the momentums $P_1 + P_2$ or the transverse momenta $P_{T1} + P_{T2}$ of the two leptons. Although these choices could give comparable sensitivities, it was decided that the leptons' $P_T$ was the optimum choice, as it is a semi-invariant variable that can be used both in the dilepton and the lepton+jets channels.

This method is especially important as it provides a top mass measurement using just a simple and well measured variable. It can be used essentially unaltered for both the channels and can provide many checks i.e the effect that has been observed that the top mass measured in the dilepton channel is traditionally located in a lower

region than the one measured in the lepton+jets channel. During the process of developing the method, detailed checks on the lepton measurements are performed, as for example how well this variable is off-line reconstructed and how one can optimize this measurement - lepton $P_T$ scale uncertainty. Furthermore it helps the understanding of event selection criteria used by many other analysis of the experiment and the backgrounds, as it can be broken down to top measurements using the individual lepton types, i.e e's and $\mu$'s.

The top mass measurement using the leptons' $P_T$ is in principle a very simple and straightforward analysis, a fact that gives the opportunity to have full control in every step of it. It can actually deliver consistent results using two independent methods. The first method, called the "Straight Line" method, exploits just the linear relation between the leptons' $P_T$ and the top mass. With the second method, called the "Likelihood" method, the full $P_T$ spectrum is modeled by an analytical function and the top mass is estimated using the likelihood minimization procedure. This thesis is concentrated in the top mass measurement in the dilepton channel. A similar measurement has been presented and approved by the CDF for the Lepton+jets channel using 340 $pb^{-1}$ of data [9].

# Chapter 3

## The Tevatron Collider and the CDF Detector

This chapter describes the Tevatron collider and the CDF Detector

## 3.1 The Tevatron Collider

The Tevatron is a circular accelerator at the Fermi National Laboratory and is currently the highest energy particle accelerator in the world. The Tevatron accelerates protons and antiprotons in a 6.4 km circumference ring and collides them to a center of mass energy of $\sqrt{s} = 1.96$ TeV. It has 1000 superconducted magnets that are cooled with liquid helium to -268 $^0$C. An aerial view of the Tevatron complex can be seen in Figure 3.1. The acceleration occures in a number of stages. The first stage is a 750 keV Cockcroft-Walton pre-accelerator, which ionizes hydrogen gas and accelerates the negative ions. The ions then pass into the 150 meter long linear accelerator (linac) that accelerates them to 400 MeV. The ions then pass through a carbon foil to remove the electrons, and the charged protons move into the Booster to obtain the energy of 8 GeV. From the Booster the particles pass into the Main Injector and

then to the Tevatron that accelerates the particles up to 980 GeV. The protons and antiprotons are accelerated in opposite directions, crossing paths in the CDF and D0 detectors to collide at a center of mass (CM) energy of 1.96 TeV.

The details of the accelerators that form the collider complex are described in the following.

Figure 3.1: Aerial view of the Tevatron complex

### 3.1.1 Proton source

The proton source consists of a 750 keV Cockcroft-Walton pre-accelerator, a 400 MeV H-minus linac and a 8 GeV proton synchrotron called the Booster.

1. **Cockcroft-Walton pre-accelerator**

The accelerator process starts with a hydrogen bottle located in the electrostatic pre-accelerator, which is based in the Cockcroft-Walton dome and produces $H^-$ ions at the energy of 750keV. The $H^-$ ions are created in the magnetron that produces short pulses of negative ions. The dome is kept at a negative potential by a voltage multiplier that takes a 75 keV AC input and converts it to a -750 keV DC. Fermilab actually has two Cockcroft-Waltons named the I- Source and the H- Source. These two sources are virtually identical. They allow the lab to continually produce a particle beam without interference due to part failure, normal maintenance, or upgrades [28]

2. **The Linac**

The Linear Accelerator is composed of two different types of accelerating components: drift tubes and side-coupled cavities. There are five drift tube cavities and seven side-coupled cavities in the Linac. The drift tube Linac makes up the first stage of the Linac and the side-coupled Linac is the second stage. The drift tubes are copper tubes positioned inside a Linac RF cavity that protects the particle beam from the sinusoidally varying accelerating field. When the beam travels out of the drift tube and into the accelerating gap the beam sees a positive gradient and is accelerated. The side-coupled cavities give the particles an energy boost for each cavity they go through. Each cell acts as an accelerating cavity that is coupled to another cell. A Fermi cavity module consists of 16 accelerating cells and 15 coupling cells. A particle is accelerated by applying small, but increasingly larger, pulses of RF energy. The Linac takes the 750 keV $H^-$ ions from the pre-accelerator, accelerates them to 400 MeV, and then

sends them on to the Booster [29].

3. **The Booster**

   The Booster is the third accelerator in the Fermi chain of accelerators. It takes 400 MeV $H^-$ ions from the Linac (through the 400 MeV transfer line), strips the electrons off, accelerates the remaining protons to 8 GeV, and then sends them on to the Main Injector. It is the first circular accelerator in the chain of accelerators. It consists of a series of 75 magnets arranged in a 75 m radius ring with 17 RF cavities. This stage of production is repeated every 66 msec, with such a delay that a synchronization with the Linac is achieved [30].

### 3.1.2 Main Injector

The Main Injector, completed in 1999, accelerates particles and transfers beams. It has four functions: (1) it accelerates protons from 8 GeV to 150 GeV in a ring of 528.3 m radius that consists of 18 RF cavities, (2) it produces 120 GeV protons, which are used for antiproton production, (3) it receives antiprotons from the Antiproton Source and increases their energy to 150 GeV, (4) it injects protons and antiprotons into the Tevatron.

To produce antiprotons, the Main Injector sends 120 GeV protons to the Antiproton Source, where the protons collide with a nickel target. The collisions produce a wide range of secondary particles including many antiprotons. The antiprotons are collected, focused and then stored in the Accumulator ring. When a sufficient number of antiprotons has been produced, they are sent to the Main Injector for acceleration and injection into the Tevatron.

### 3.1.3 Antiproton source

The biggest bottle-neck in a proton-antiproton collider is the time required to accumulate the required number of antiprotons [31]. The antiproton source consists of a target station, two rings called Debuncher and Accumulator and the transport lines between the rings and the Main Injector. The antiprotons are produced by bombarding a production Ni target with a high energy proton beam, where the production rate is primarily dependent on the incident beam energy. The $\bar{p}$ beam collected is of 8 GeV, as this is the peak production from a 120 GeV proton beam.

The actual production and collection of antiprotons occur in a specially designed vault. The target is a stuck of nickel disks separated by copper cooling disks with channels of air flow to provide heat transfer. Standard sized disks are about 10 cm in diameter and 2 cm thick. All the disks have a hole in the center to direct the air flow out of the assembly. Immediately after the Target module is the Collection Lens module. The lens collects the secondary particles coming off the target and renders them parallel to each other. A 3-degree pulsed dipole -Pulse magnet- follows the lens. It selects 8 GeV negatively charged particles and bends them into the line that leads to the Debuncher.

The Debuncher accepts pulses of antiprotons and reduces their momentum spread. This procedure is followed to improve the Debuncher to Accumulator transfer due to the limited opening of the Accumulator at the injection. The Debuncher is a rounded triangle divided into 6 sectors. Each sector contains 19 quadrapoles and 11 dipoles.

The purpose of the Accumulator is to accumulate antiprotons. This is accomplished by stacking successive pulses of antiprotons from the Debuncher over several

hours or days. Both RF and stochastic cooling systems are used in the momentum stacking process. The RF decelerates the recently injected pulses of the antiprotons from the injection energy to the edge of the stuck tail. The stack tail momentum cooling system sweeps the beam deposited by the RF away from the edge of the tail and decelerates it towards the dense portion of the stack, called the core. Additional cooling systems keep the antiprotons in the core in the desired momentum and minimize the transverse beam size.

### 3.1.4 The Tevatron

The Tevatron [32] is loaded with 150 GeV proton and antiproton beams, boost them to the energy of 980 GeV and collides them in the center of the CDF [33],[34], [35], [36] and D0 [37], [38] detectors. This accelerator is a superconducting magnet synchrotron housed in a tunnel of 1 km radius. The dipoles, quadrapoles and correction magnets are cooled with liquid Helium to the temperature of 4.6K, where they become superconducting. As seen in Figure 3.2 the ring is divided into six equally spaced sectors, designated A, B, C, D, E and F. Each sector is broken into 4 sections with specialized functions. Each sector starts with a section called "zero". The A0 contains the proton and antiproton beams abort for collider. The B0 (the CDF experiment) and D0 (the D0 experiment) contain the collider detectors. At C0 there is also the proton abort line. The E0 contains the scrapers that remove circulating protons after the collider store. The F0 contains the 8 RF cavities, as well as the injection lines from the Main Injector.

With the Tevatron magnets set at 150 GeV, 36 bunches of protons and antiprotons

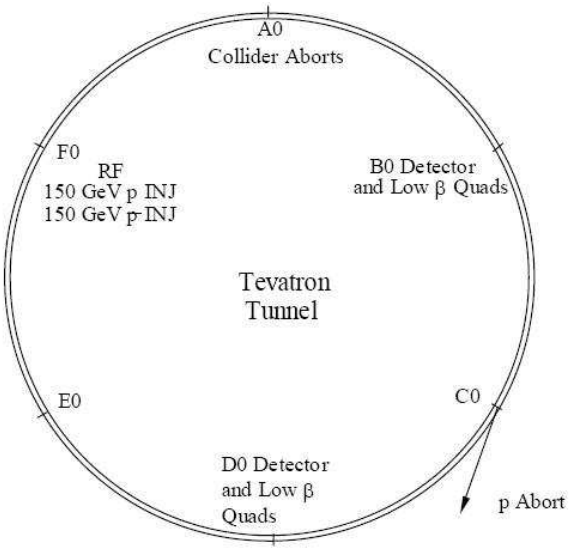


Figure 3.2: The Tevatron ring

are injected from the Main Injector. The bunches are inserted one at a time, spaced such that they cross every 396 ns. The protons and antiproton are then accelerated and they reach the energy of 980 GeV at 85 sec. The protons move clockwise and the antiprotons counterclockwise, in the same ring, under the influence of the magnetic field. The proton and antiproton beams can be used for several hours after their injection. The beam flux is measured with the luminosity. The instantaneous luminosity is given by:

$$\mathcal{L} = \frac{N_B N_p N_{\bar{p}} f}{2\pi\sigma_p^2\sigma_{\bar{p}}^2} \tag{3.1}$$

where $N_B$ is the number of bunches in the accelerator, $N_p$ and $N_{\bar{p}}$ is the number of p and $\bar{p}$ per bunch, $f$ is the bunch revolution frequency and $\sigma_p$ and $\sigma_{\bar{p}}$ are the the effective widths of the p and $\bar{p}$ bunches.

Figure 3.3 shows the Tevatron peak luminosity up to July 2007.

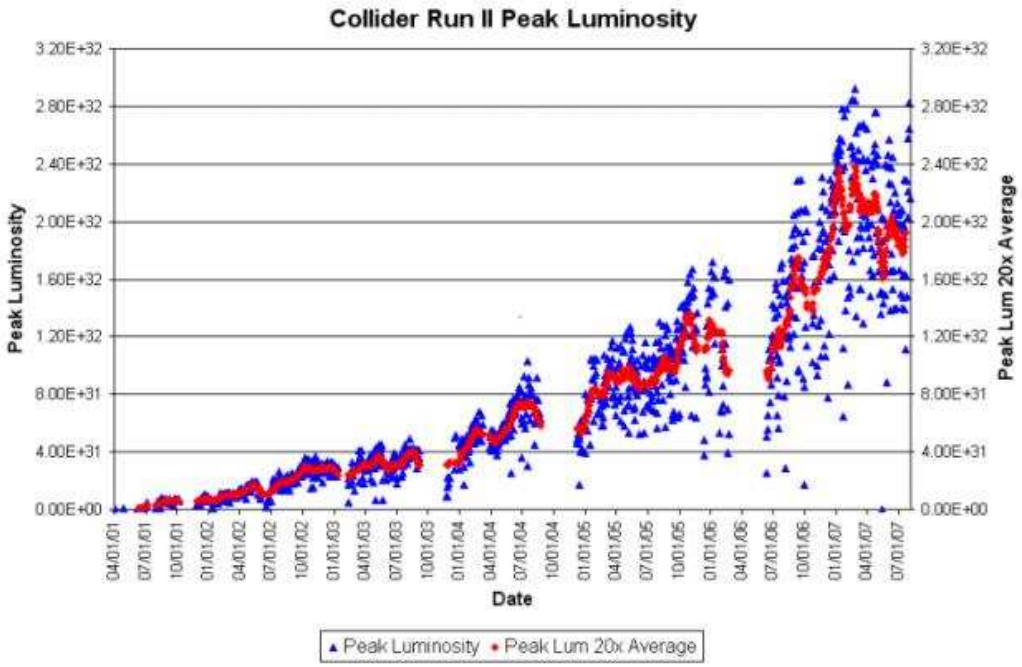


Figure 3.3: The Tevatron peak Luminosity as a function of the time, until the beginning of July 2007.

The integrated luminosity $\int \mathcal{L}dt$ gives a measure of collisions in a given period of time. Figure 3.4 shows the integrated luminosity $\int \mathcal{L}dt$ at CDF as of the end of spring 2007. The analysis presented in this dissertation is performed using 1.8 fb$^{-1}$ of data. By the end of CDF Run II 8-10 fb$^{-1}$ are expected to be available.

The Collider Detector at Fermilab (CDF) is a generic purpose experiment for the study of p$\bar{\text{p}}$ collisions at $\sqrt{\text{s}} = 1.96$ TeV at the Tevatron Collider. The experiment is located at the B0 sector of the Tevatron ring. First collisions took place and were detected in October 1985. Figure 3.5 illustrates the first collision at $\sqrt{s} = 1.96\ TeV$ at CDF as recorded by the Cherenkov Luminosity Counter.

The data yield since the first collisions ever occurred is:

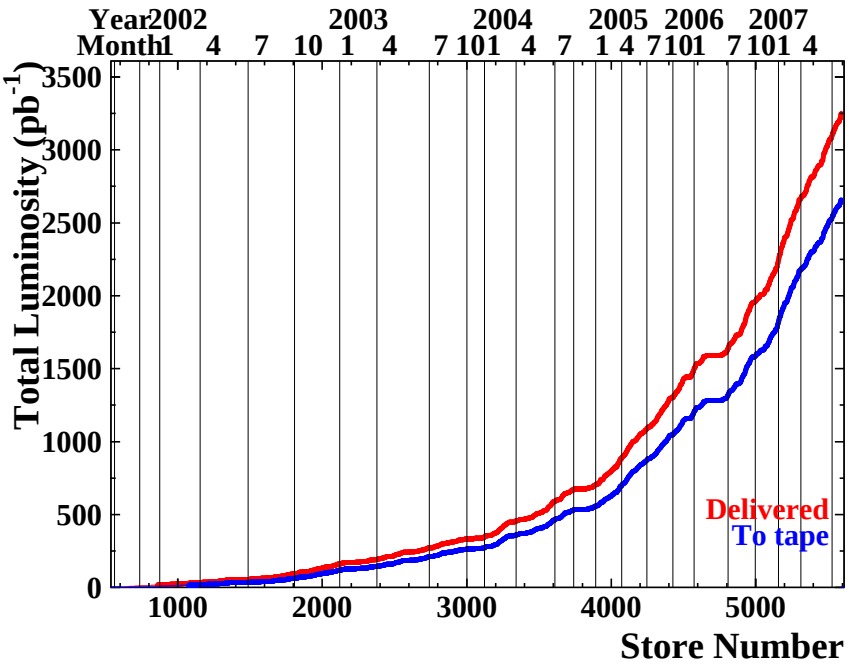


Figure 3.4: The total CDF integrated luminosity $\int \mathcal{L}dt$ as of the end of spring 2007. The red line is the total delivered $\int \mathcal{L}dt$ and the blue line is the $\int \mathcal{L}dt$ written in tape.

- 25 $nb^{-1}$, 1987
- 4.5 $pb^{-1}$, 1988-1989 Run 0
- 19 $pb^{-1}$, 1992-1993 Run Ia
- 90 $pb^{-1}$, 1994-1996 Run Ib
- 1.8 $fb^{-1}$, summer 2007 Run II

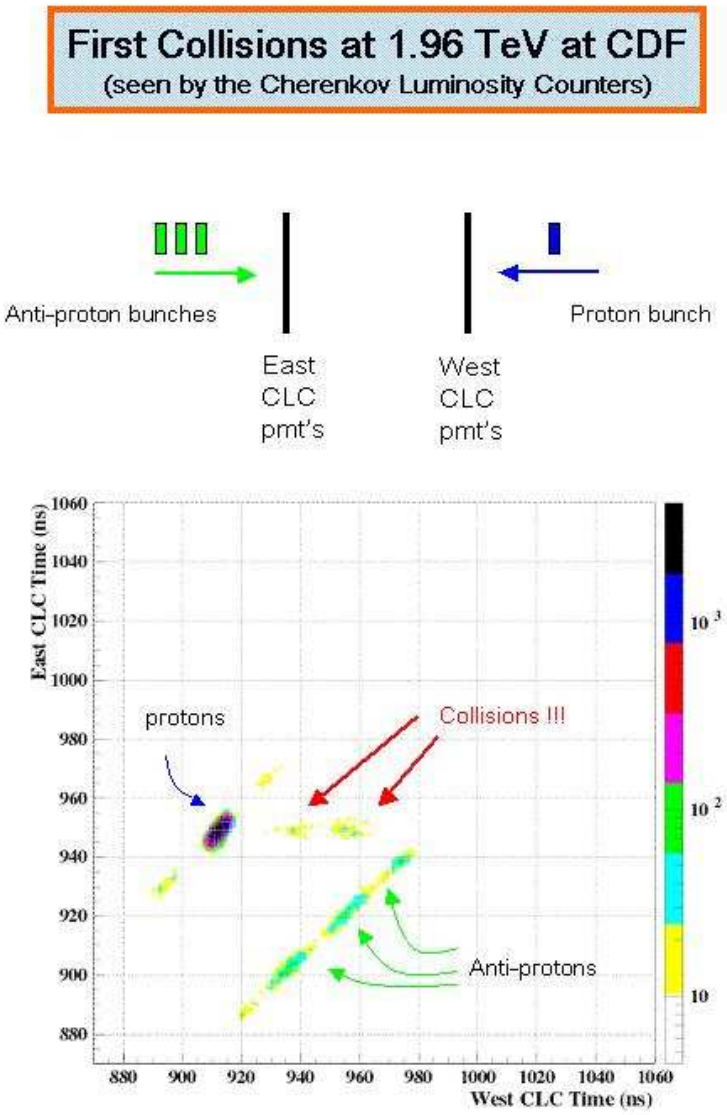


Figure 3.5: The first collision ever at $\sqrt{s} = 1.96\ TeV$ at CDF as recorded by the Cherenkov Luminosity Counter.

## 3.2 The CDF Detector

Figure 3.6 illustrates the CDF Run II Detector which is operating since 2001. It is an azimuthally and farward-backward symmetric apparatus for the study of $p\bar{p}$ collisions at $\sqrt{s} = 1.96\ TeV$ [34], [35], [36].

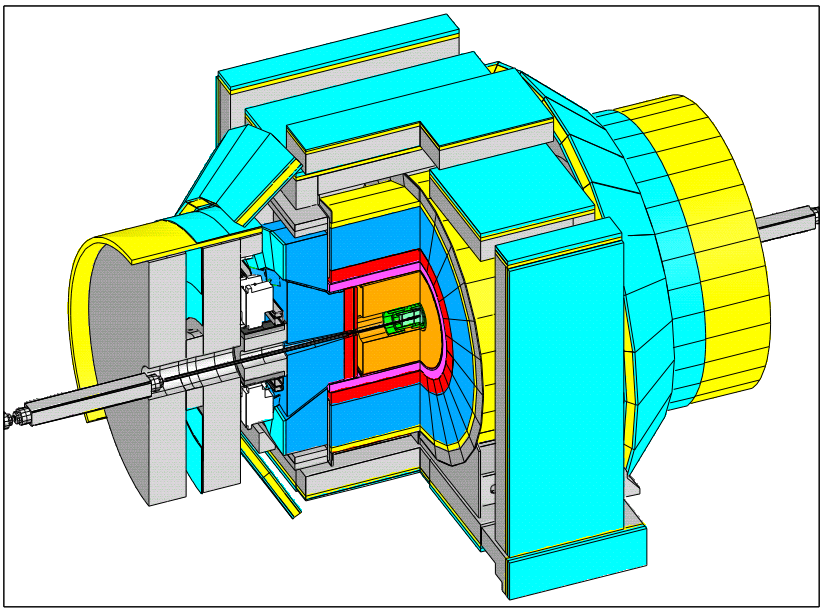

Figure 3.6: Schematic view of the CDF detector

It is a general purpose solenoidal detector that performs precision charged particle tracking, fast projective calorimetry and fine grained muon detection. Its purpose is to do high mass/high $P_T$ physics. It has been designed to distinguish and measure e's, $\mu$'s, partons (as jets), photons and $\nu$'s (from missing $E_T$) (figure 3.7).

The tracking systems are in a magnetic field of 1.4 T parallel to the beam axis, formed by superconducting solenoid 1.5 m in radius and 4.8 m in length. The calorimeters and the muon detectors are outside the solenoid. A solid cutway view of the detector is shown in Figure 3.8. The coordinate system is defined as for the

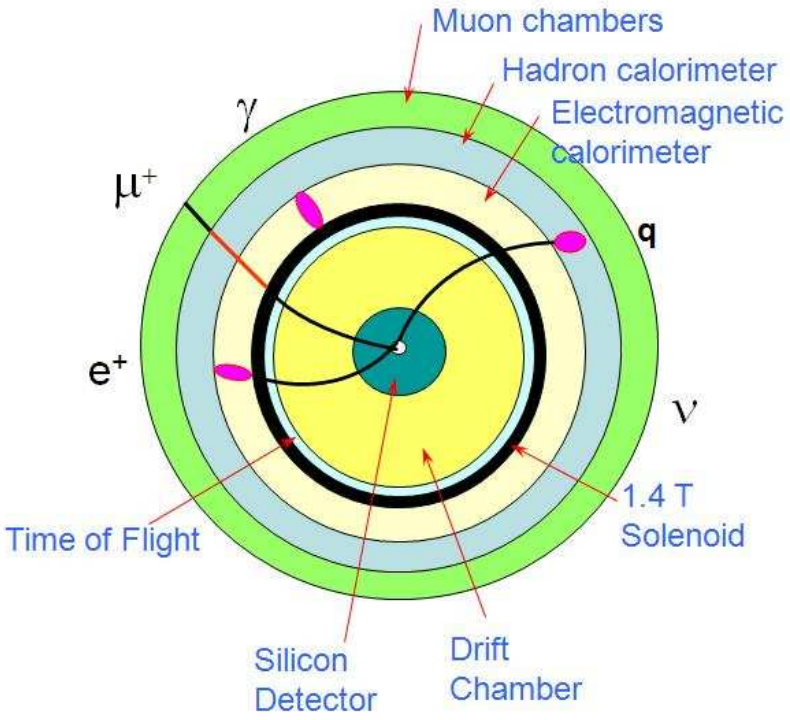


Figure 3.7: Particle paths in the different detector components

polar angle $\theta$ to be measured from the proton direction and the azimuthal angle $\phi$ to be measured from the Tevatron plane. The pseudorapidity $\eta$ is defined as:

$$\eta = -\ln(\tan\frac{\theta}{2}) \tag{3.2}$$

A more detailed description of each subdetector component is given in the following.

### 3.2.1 Tracking Systems

The tracking of the charged particles is one of the most important ingredients of every CDF analysis. The CDF tracking system consists of a silicon microstrip system

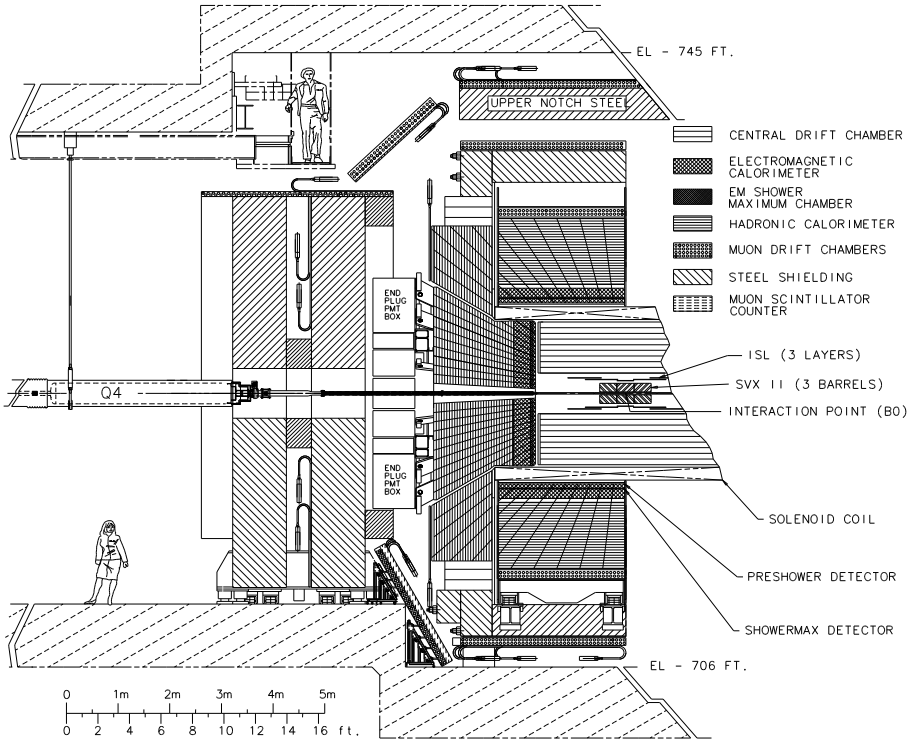


Figure 3.8: Cutway view of the CDF detector

and a drift chamber that surrounds it. The silicon system consists of three subsystems. The first one, Layer L00 is closer to the beam pipe and is a radiation-hard single sided detector. The two other subdetectors consist of layers that are radiation-hard double sided detectors. The first five layers comprise the SVXII system and the three latter the ISL system. The entire system is in a barrel geometry and cover a pseudorapidity range $|\eta| < 2$. It is extended from 1.5 cm from the beam pipe to 28 cm. It provides a three-dimensional track reconstruction. The impact parameter resolution of the SVXII and the ISL is 40$\mu$m. The z0 resolution of the SVXII and the ISL is 70$\mu$m. The drift chamber is called Central Outer Tracker (COT). It covers a pseudorapidity range of $|\eta| \leq 1$ and a radial range from 40 to 137 cm. It is comprised of 96 layers, organized

into alternating axial and $\pm 2^0$ stereo superlayers. The hit position resolution is $140\mu$m and the momentum resolution $\sigma(P_T)/P_T^2 = 0.0015(GeV/c)^{-1}$. Figure 3.9 illustrates a side view of the silicon system.

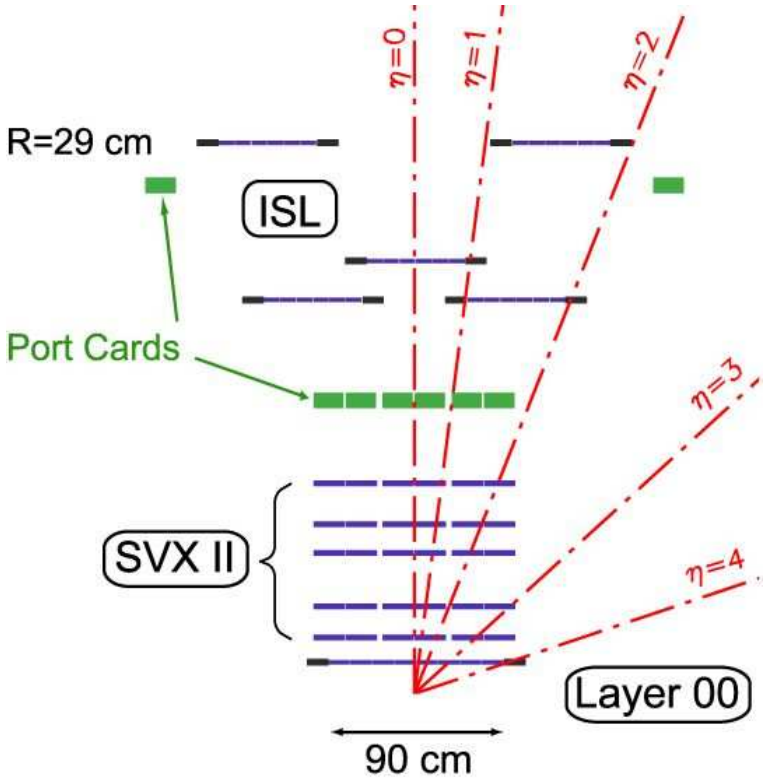


Figure 3.9: Side view of the silicon system

### The L00 Detector

Layer-00 is the first layer of silicon in the tracking system of the CDF detector, added during the CDF II upgrade [39]. It consists of single-sided silicon detectors located between the radius of 1.35 cm and 1.62 cm from the beam line. Alternative strips are read-out giving a hit resolution of $6\mu$m. The purpose of this layer is to improve the impact parameter resolution and enhance the b-tagging recognition.

### The SVX II Detector

The SVX II detector is a central vertexing detector that provides r-z and r-$\phi$ measurements [39], [40]. It consists of double-sided silicon sensors with a combination of both 90-degree and small-angle stereo layers. In more detail the SVXII consists of three barrels, of 29 m length each. Each barrel is divided in 12 wedges in $\phi$, each having 5 layers of silicon. The silicon layers are aligned either with the z axis (axial) of an angle of $90^0$ or $1.2^0$ with respect to the z axis. This permits good resolution in locating the z-position of the secondary vertices and improves the three-dimensional recognition capability. The radius of the innermost and outermost layer is 2.44 cm and 10.6 cm respectively. The electronics are in the form of hybrids that are mounted directly to the silicon surface at each end of each four-sensor mechanical ladder assembly. Schematic views of the detector are shown in Figures 3.10 and 3.11.

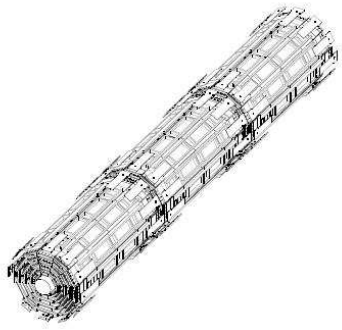

Figure 3.10: Schematic view of the SVXII detector, where the three different barrels can be seen

### The ISL Detector

The Intermediate Silicon Detector comprises the outer detector of the silicon system [39], [41]. Two layers lie at r=20 cm and r=28 cm in the plug region ($1 < \eta < 2$)

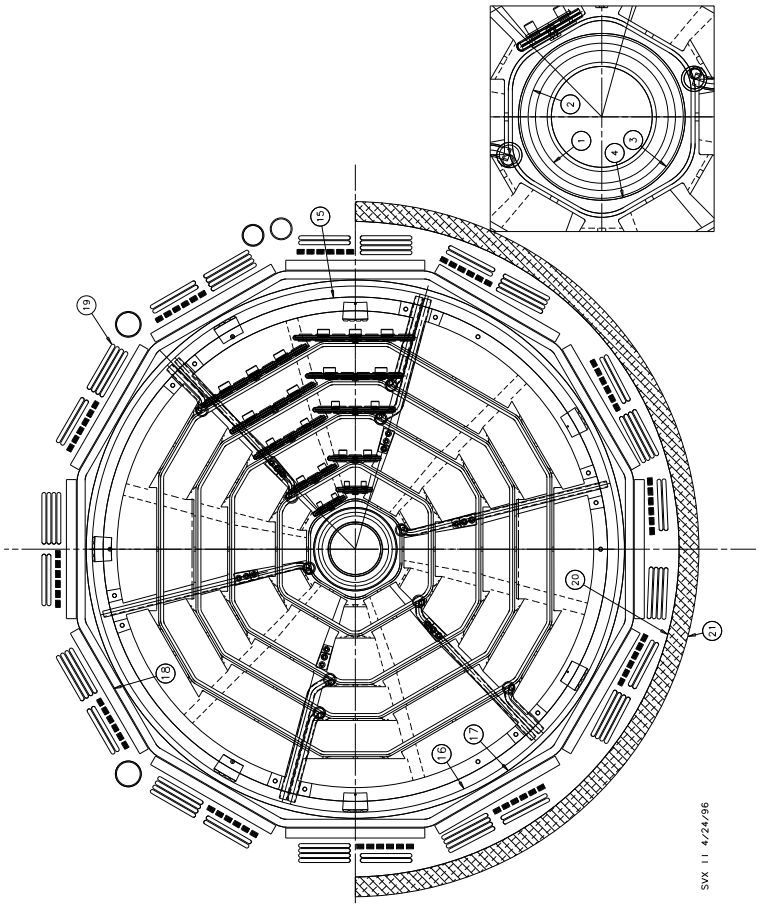


Figure 3.11: Schematic view of the SVXII detector, where the 12 wedges and 5 layers can be seen

and one at = 22 cm in the central region ($|\eta| \leq 1$). The silicon crystals are identical and measure 58mm wide (56.3 mm active) and 74mm long (72.4 mm active). The crystals are double-sided with axial strips in one side and small $1.2^0$ stereo strips on the other, where the total number of strips is 512. The ISL detector is composed of 296 units, called ladders. Each ladder is made of two half-ladders butted end-to-end. The half-ladders are made of three silicon sensors bonded together to form an electrical unit. The axial hit resolution is $\leq 16$ $\mu$m and the stereo hit resolution is $\leq 23$ $\mu$m. Figure 3.12 demonstrates an r-$\phi$ view of the ISL silicon placements in the

large $\eta$ region.

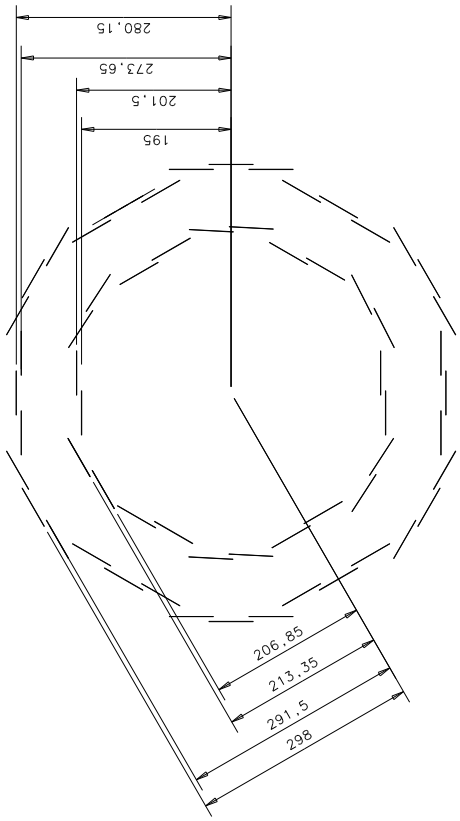


Figure 3.12: An r-$\phi$ view of the ISL silicon placements in the large $\eta$ region

### The COT Detector

The Central Outer Tracker is an open-cell drift chamber designed to perform central tracking with high momentum resolution in the high luminosity environment of the Tevatron [39], [42], [43], [44] . It can provide transverse momentum resolution of $\delta P_T/P_T^2 \leq 0.0015(\mathrm{GeV/c})^{-1}$. The COT consists of 8 super-layers that are divided in to super-cells. Each super-cell consists of 12 wires with a drift distance that is almost the same for all super-layers. The super-layers alternate in the stereo-axial-stereo-

axial pattern, with the stereo angle of $\pm 3^0$. In each of the super-layers the 12 sense wires alternate with 13 potential wires to provide field shaping in a cell. In each cell there are also 4 shaper wires and a Au-mylar sheet to complete the field. The 12 sense wires, the 13 potential wires and the field sheet form a wire plane. In total, there are 30,240 sense and 32,760 potential wires. The sense and potential wires have a diameter of 40 $\mu$m and are made of gold plated tungsten. The Au-mylar sheets are in ground potential, the potential wires are in a 2kV and the sense wires in a positive 3 kV potential. The wire separation is 7.62 mm in the plane of the wires and the maximum drift distance, as defined from the azimuthal separation of the sense wires and the field planes is 0.88 cm. The cells are tilted at $35^0$ with respect to the radial direction to account for the Lorentz angle of the electrons in the magnetic field such as the drift direction is azimuthal. Figure 3.13 shows the arrangement of the wires in a cell.

The active volume of the COT is 43 cm from the beam line going to 133 cm. If tracks have $|\eta| < 1$ they pass all 8 super-layers. Tracks with $|\eta| < 1.3$ pass through 4 or more super-layers. The gas mixture used in the chamber is Argon-Ethane-$CF_4$ (50:45:15) bubbled through isopropyl alcohol. The maximum drift distance is 100 ns which has a maximum drift distance of 0.88 cm.

### 3.2.2 Time of Flight

The Time of Flight detector is used to precisely measure the time a particle needs to travel from the interaction point to the time of flight detector [45]. It is primarily used to perform particle identification of pions and kaons using their different time

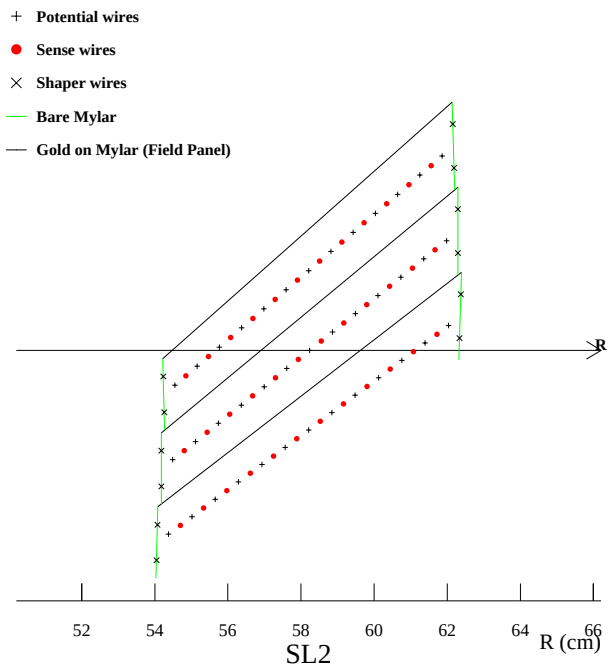


Figure 3.13: Three COT cells, where the sense, potential, shape wires and Au-mylar layers can be seen.

of flight in the detector, providing an accuracy of 100 ps. Figure 3.14 shows the separation power of the detector for pions, kaons and protons. The TOF covers the range of $|\eta| < 1.2$ and consists of 296 scintillator bars (4x4x179.5 cm$^2$) as a cylinder directly outside the COT. There is a photomultiplier tube at each end that together with the read-out electronics they measure the time, when the collected charge is above the threshold. The charge is integrated within a time window of 10 ns.

### 3.2.3 Calorimeters

The calorimeters play a a very crucial role in the CDF measurements. They perform precision energy measurements of the electromagnetic and hadronic objects. In

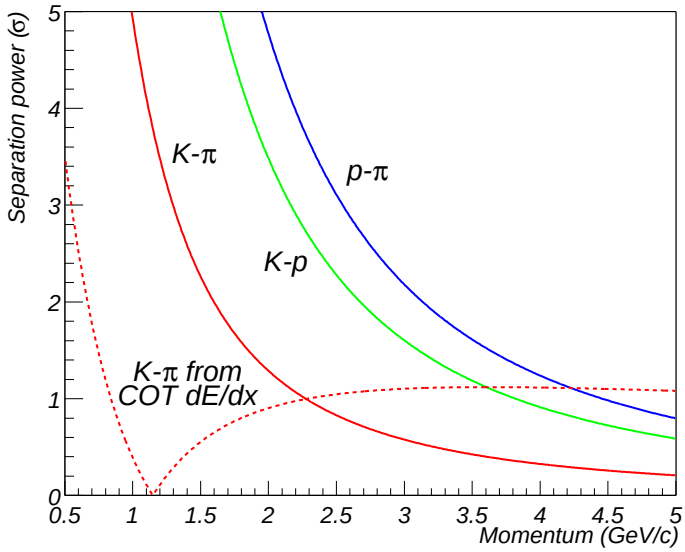


Figure 3.14: Separation power of the TOF detector for pions, kaons and protons vs the momentum.

the calorimeter volume, the incident objects being totaly absorbed, leave information about their energy and their position. In the process of absorption showers are generated by the cascades of the interactions.

Incident electromagnetic particles i.e. electrons and photons, are fully absorbed in the electromagnetic EM calorimeter. The construction of the EM calorimeters takes advantage of the short electromagnetic shower shape to measure energy and position. At high energy it makes little difference whether the cascade started with an electron or a photon. As the cascade develops the number of particles increases; the electrons lose energy with the bremsstrahlung process and the photons with pair production (see Figure 3.15). When the energy of the charged particles degrades to the regime dominated by ionization loss the cascade stops. The electromagnetic cascade depends on the density of the electrons in the absorber medium. Therefore the longitudinal dimensions are described, in a material dependent way, by the radiation

length $X_0$; approximately, $X_0[gr/cm^2] = 180A/Z^2$. In the early stage of the cascade the lateral spread is characterized by the typical angle of the bremsstrahlung emission $\theta_{brem} \sim p_e/m_e$ and the multiple scattering in the absorber. The later process causes the gradual widening of the absorber as the energy decreases. Finally the cascade occupies a cylinder of radius $R \approx 2\rho_M$, where $\rho_M \simeq 21X_0/\epsilon \simeq 7A/Z$ is the Moliére Radius. While the high-energy part of the cascade is dominated by the value of the $X_0$, the low-energy tail is characterized by the critical energy $\epsilon$ in the medium. The critical energy is defined as the energy loss of the electrons by collisions in the medium per unit $X_0$.

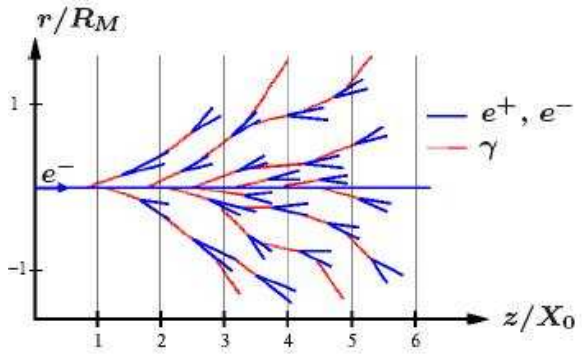


Figure 3.15: Schematic of an electromagnetic shower.

Incident hadrons are nearly fully absorbed by the hadronic calorimeter. The size of the hadronic calorimeters is such that they contain the widely fluctuating shape of the hadronic showers. In passing through matter a hadron can build a shower through multiple interactions. The showering process is dominated by a succession of inelastic hadronic interactions, characterized by multiple production and particle emission originating from the decay of exited nuclei(i.e p+nucleus$\rightarrow \pi^+ + \pi^- + \pi^0 +$

$K^- + ... +$ nucleus*). A considerable part of the secondary particles are $\pi_0$'s which propagate electromagnetically without any further nuclear interactions. The two processes give a very different shower composition for an incident hadron (see Figure 3.16. The hadronic multiplication process is measured in the scale of the interaction length $\lambda$. The $\lambda$ is defined as the mean free path that a particle undergoes before interacting.

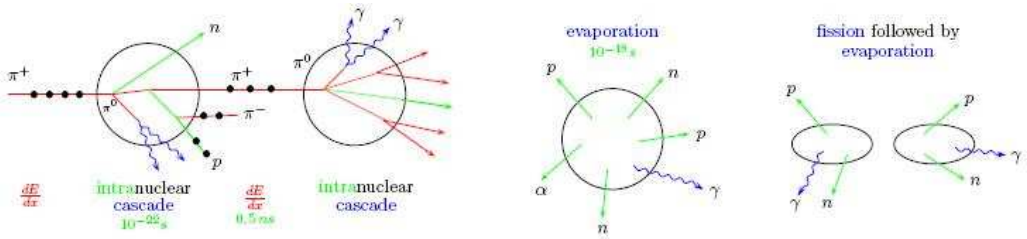


Figure 3.16: Schematic of hadronic interactions within the hadronic shower.

In the CDF detector the calorimetric system consists of electromagnetic and hadronic sections in the the central and the plug regions [39], [46]. The central calorimeter is a scintillator sampling system with tower segmentation. Each wedge consists of a lead-scintillator EM part followed by a steel-scintillator hadronic part. It covers the pseudorapidity range $|\eta| < 1.1$ and $|\eta| < 1.3$ with the endwall hadronic calorimeter. The plug calorimeters cover the $1.1 < |\eta| < 3.6$ area. There is an electromagnetic part with shower position detection, followed by the hadronic part. In both sections the active elements are scintillator tiles read-out by wave-length shifting fibers. The various calorimeter compartments are shown in Figure 3.17

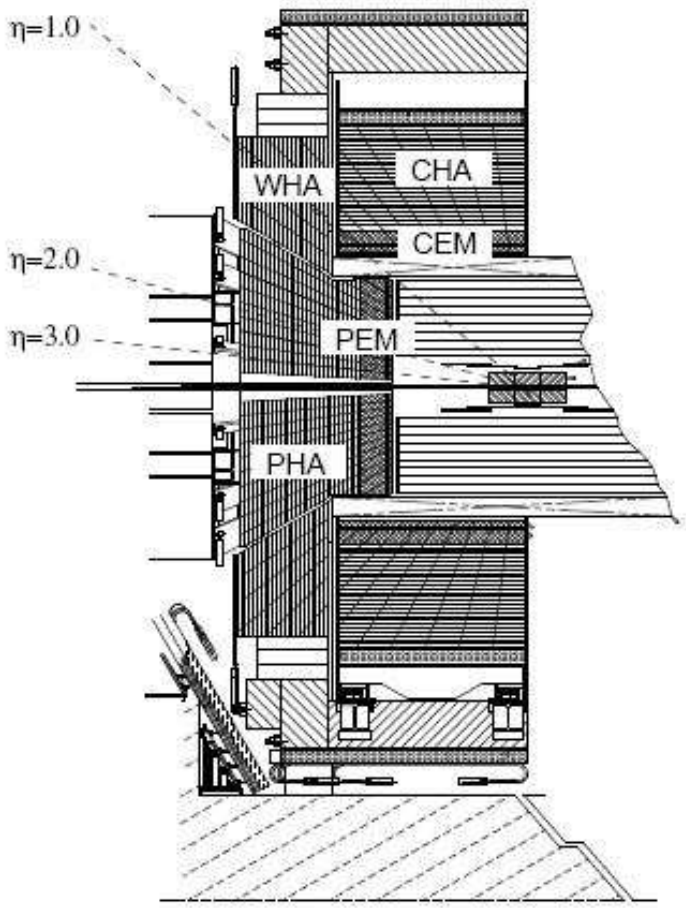


Figure 3.17: Schematic view of one half of the CDF detector, where the different calorimetric systems can be seen

### Central Electromagnetic Calorimeter

The Central Electromagnetic Calorimeter CEM is a lead-scintillator sampling system [39]. Its wedges are $15^0$ in azimuth and 0.11 in pseudorapidity and point to the interaction point. In each wedge the lead and the scintillator are alternating with an embedded two dimensional read-out strip at shower maximum. The total thickness of the CEM is 19 $X_0$ ($1\lambda$), where the absorber is 0.6 $X_0$ ($1\lambda$) and the active medium is 5

mm per unit. Wavelength shifters are located at the $\phi$ surface and direct the light to the PMTs (Hamamatsu R580). The energy resolution, as measured from test beams, is $\sigma(\mathrm{E})/\mathrm{E} = 14\%/\sqrt{\mathrm{E}} \oplus 1\%$. In about 5 $\mathrm{X}_0$ the Shower Maximum Detector (CES) is located consisting of gas chambers with wire and strip elements. The CES performs electron and photon identification using position measurements in combination with matching with tracks. It also uses the transverse energy profile to separate $\pi^0$ and photons. Its position resolution is 2 mm at 50 GeV. On the front face of the CEM the Central Preshower Detector (CPR) performs photon and soft electron identification and charged pion rejection. This is a gas detector that samples early showers and uses the coil and the trackers as radiator and active elements.

### Central and Endwall Hadronic Calorimeters

The Central CHA and Endwall WHA Hadronic Calorimeters are both steel-scintillator sampling systems [39]. The CHA consists of 4.5 interaction lengths, where the absorber is 1 inch and the active medium is 10 mm per unit. It is placed behind the CEM and performs hadronic jet measurements in the $|\eta| < 0.9$ ragion. Its energy resolution is $\sigma(\mathrm{E})/\mathrm{E} = 75\%/\sqrt{\mathrm{E}} \oplus 3\%$ GeV. The Endwall hadronic calorimeter covers the $0.9 < |\eta| < 1.3$ area. It is similar to the CHA and consists of 4.5 interaction lengths, where the absorber is 2 inches and the active medium is 10 mm per unit.

### Plug Upgrade Calorimeter

The Plug Upgrade calorimeter covers the $1.1 < |\eta| < 3.6$ region. It consists of an electromagnetic section PEM with a shower position detector followed by a hadronic section PHA [39]. Both of them use scintillator tiles as active element and are readout

by wavelength shifting fibers that carry the light to the PMTs. The schematic of the Plug Upgrade calorimeter is illustrated in Figure 3.18

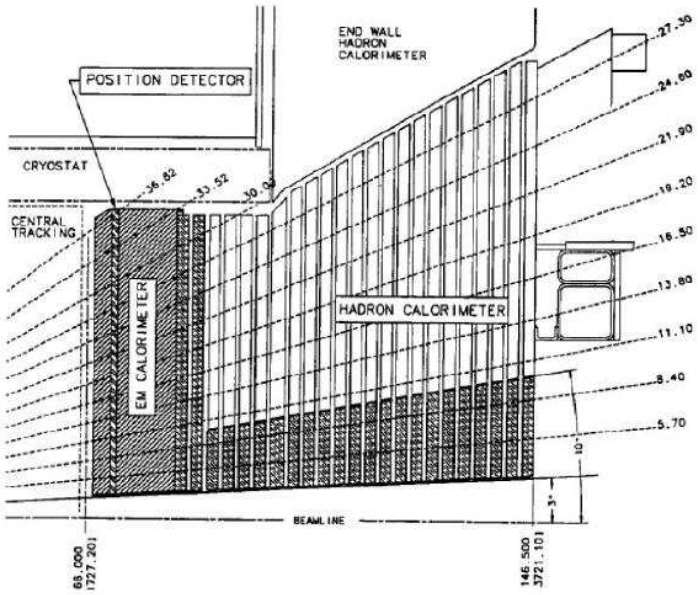


Figure 3.18: Schematic view of the upper part of the Plug Upgrade calorimeter.

The PEM is a lead-scintillator sampling system. Its thickness is 21 $X_0$, formed by 23 layers with $0.8X_0$ of absorber and 4.5 mm of active medium per unit. The energy resolution is approximately $16\%/\sqrt{E} \oplus 1\%$. The first term is due to sampling fluctuations and the PMTs' photostatistics and the second term is due to the non-uniformity of the calorimeter. The scintillator tails of the first layer act as a preshower detector. They are 10 mm thick and are readout separately from the rest of the tails in the detector. Information from this part of the detector enhances the $\gamma$ physics especially in the high $\eta$ region. The maximum shower detector is made of scintillator strips. It is located in 6 $X_0$ inside the PEM and covers a circular area of 2.6 m in

diameter at 1.8 m from the interaction point. It performs position measurements of the electron and photon showers and helps their separation from the $\pi^0$.

The PHA is a steel-scintillator device. It consists of 23 layers of 7 interaction lengths with 2 inches of absorber and 6 mm of active element per unit. Stainless disks are added to the inner $10^0$ cone to extend the coverage to $3^0$. Its thickness is increased with two more disks located behind the electromagnetic part. The energy resolution is approximately $74\%/\sqrt{\mathrm{E}} \oplus 4\%$. Its overall design is such that the $\eta - \phi$ segmentation would allow to effectively perform b, Z, W, $\gamma$ and jet physics.

### 3.2.4 Muon Systems

The muon detection system is very important for the physics performed in CDF. The W boson and therefore the top quark are identified through their decay to electron and muon leptons. Furthermore systematic effects are studied through calibration procedures of the Z boson and the J/$\psi$ particle decaying to muons. The muons are 207 times heavier than the electrons and emit little bremsstrahlung radiation a fact that makes them quite penetrating. Their track and momentum is primarily measured in the tracking systems but their identification is done in the muon systems as they are the only charged particles that make it through thick absorber layers. The material of the calorimeters and the magnet function as the necessary absorber to stop all other charged particles.

The muon system in the CDF consists of drift chambers and scintillator layers covering a pseudorapidity range up to 1.5. The absorbing material for these systems is the calorimeter steel, the magnetic return yoke and additional steel absorbers. In

detail it consists of the Central Muon Detector CMU, the Central Muon Upgrade chambers CMP with scintillator counters CSP, the Central Muon Extension CMX with scintillator counters CSX, the Barrel Muon Chambers BMU and scintillator counters BSU and toroid scintillator counters (TSU).

All the muon systems function similarly. In each muon system the rectangular shaped drift chambers are filled with Ar:$C_2H_6$ (50:50) gas mixture at atmospheric pressure. A positive high voltage is applied to the sense wire so that the chamber performs in a proportional regime. The charge pulse, produced as a result of ionizing radiation from the muons, is then read out on the end of the wire, amplified, shaped, and eventually sent to TDC. In the case of CMU and BMU ganged wires at both ends of the ganged wire are being read out. The amount of charge collected on each side is proportional to the distance from the end of the wire to the ionization point. The charge collected on the wire is encoded into the pulse width in this case. This can later be used for z-position reconstruction using charge division. The light in the scintillators, produced in response to the ionizing radiation, is collected via WLS fibers and is then sent further to PMT. The pulses from the photomultiplier tube are eventually converted to the TDC hits which are read out by the data acquisition system and are used for trigger and further processing.

**Central Muon Detector**

The Cental Muon Detector CMU is embedded in the central calorimeter wedges, at their outer radius [39]. It uses the $5.5\lambda$ of absorber formed by the central hadronic calorimeter. It covers a pseudorapidity range up to 1 and polar angle of $360^0$. It

consists of 3 layers of 16 channels (4 wide x 4 high) in each wedge. The 16 rectangular cells have dimensions 6.35×2.68×226 cm with a 50 $\mu$m wire in the center. A schematic view of the CMU detector is shown in Figure 3.19. The first and the third layer have a small $\phi$ offset with respect to the second and forth. The two adjacent layers are readout together. With the use of a TDC, the drift time on the radially aligned wires give a measure of the track momentum. The charge collected by the end of each wire is encoded into a pulse by an Amplifier-Shaper-Discriminator card and is used to perform z localization of the muons. The maximum drift time of the drift chamber is 800 ns and the minimum detectable transverse momentum is 1.4 GeV/c.

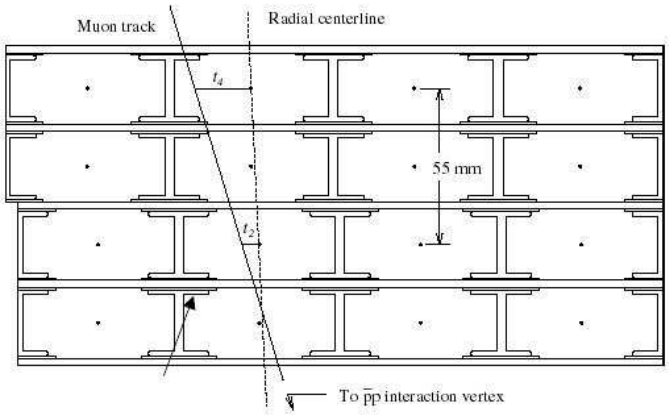


Figure 3.19: Schematic view of the CMU detector.

### Central Muon Upgrade

The Central Muon Upgrade CMP covers a pseudorapidity range up to 1 providing confirmation of the CMU tracks with reduced non-muon background [39]. It is installed outside of 60 cm of steel and consists of 4 layers with alternate half-cell staggering. They are single-wired drift cells in the $55^0 < \theta < 90^0$ region. A schematic

of the ancillary function of the CMP detector is illustrated in Figure 3.20.

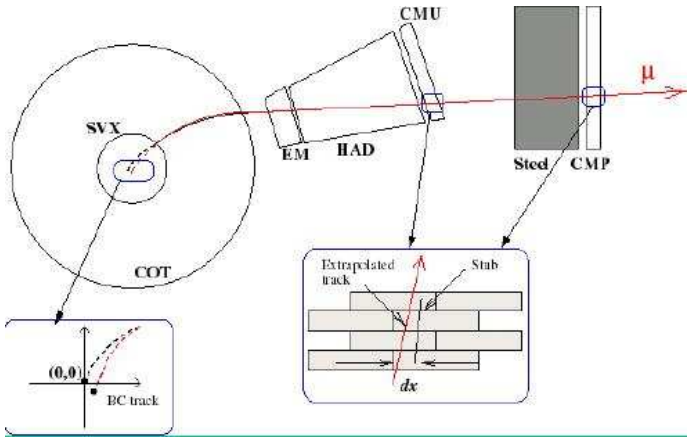


Figure 3.20: Schematic view of the tracking and identification of a muon in the $|\eta| < 1$ region by the CMU and CMP detectors

The drift chambers are rectangular and fixed in length in the z direction forming a box around the central detector. The pseudorapidity therefore varies in $\phi$ as shown in Figure 3.21. It provides information only in the transverse plane and not in the the z direction due to its geometry.

The tubes are made of aluminium. They have a single wire in the middle and field shapening cathodic strips at the top and bottom. They are 2.5×15 cm and 640 cm long and their walls are 0.26 cm thick. The maximum drift time is about 1500 ns.

Scintillator counters CSP are installed in the outer surface of the CMP chambers. They are rectangular in shape with dimensions 2.5×15×320 cm. They cover two CMP chambers in width and half in length. They are readout by phototubes located at z=0.

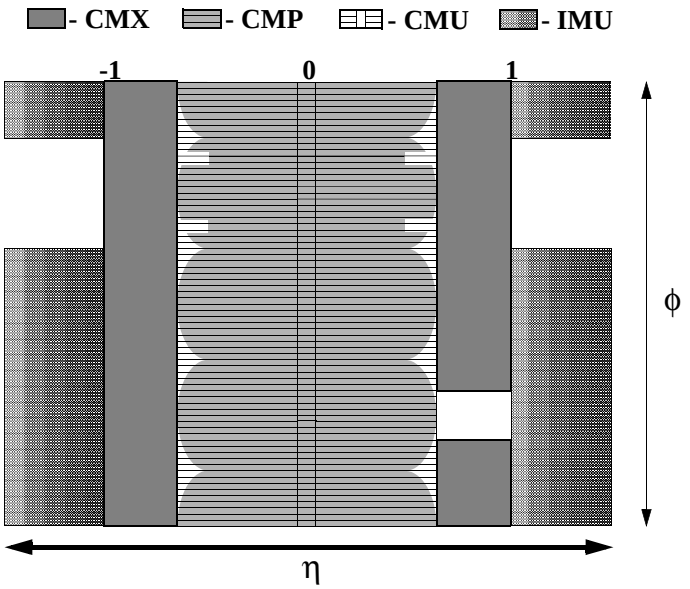


Figure 3.21: Location of the central muon upgrade components in azimuth $\phi$ and pseudorapidity $\eta$ for Run II.

### Central Muon Extension

The Central Muon Extension CMX covers a pseudorapidity range $0.6 < |\eta| < 1.0$ and extents the polar angle coverage from $42^0$ to $55^0$ [39]. It consists of conical sections of drift tubes that are arrayed with their wires coplanar with the beam. It forms a logical extension of the CMP and uses no additional absorbing material as in the large angle that it is located the muons pass through more material than they do in the central system. There are 4 layers of 12 tubes for each $15^0$ $\phi$ sector. Successive layers have a half-cell offset to reduce ambiguities and each layer consists of two physical layers of drift tubes partially overlapping. The drift tubes are the same as for the CMP except that they are 180 cm long. The maximum drift time is 1600 ns. In the west side, the two wedges that for RUN I were used for the Main Injector shielding are now part of the CMX and are called "keystone". The bottom

$90^0$ of the CMX penetrates the floor of the collision hall is also part of the CMX and is called "miniskirt". The geometry of this latter part differs from the rest of the chamber and is a plane of chambers forming a flattened cone.

The CSX trapezoidal scintillator counters are completing the CMX detector and are 2 cm thick. They are located in the internal and external part of the CMX chambers. The MSX are also trapezoidal scintillator counters covering the part of the "miniskirt" that is closer to the interaction point. Figure 3.22 shows a graphical view of the CMX drift tubes and the CSX counters.

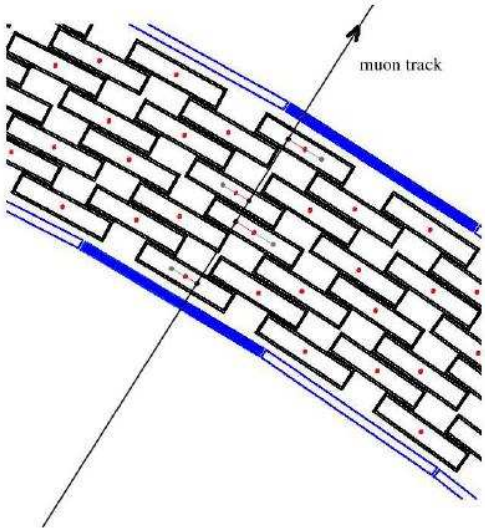


Figure 3.22: Graphical view of part of the CMX drift tubes and the CSX counters. A penetrating muon track is illustrated

### Barrel Muon Detector

The Barrel Muon Detector extends the pseudorapidity coverage to 1.5 covering the range $1.0 < |\eta| < 1.5$ [39]. It consists of 4 layers that are parallel to the beamline and

placed at the radius 3.6 m. They are 3.6 m long, 2.5 cm deep and 8.4 cm wide with each chamber covering $1.25^0$ in azimuth. The full azimuthal coverage of the detector is $270^0$. The second and fourth stacks are staggered azimuthally by a half-cell relative to the first and third. Scintillator counters called BSU are mounted on the outside part of the chamber and are 1.5 cm thick. The scintillators are 166 cm long, and 16.6 cm wide. They cover two BMU chambers in azimuth and one-half chamber in the z direction. BSU-Front covers three-fourths of azimuth, and $1.0 < |\eta| < 1.25$. BSU-Rear covers the same three-fourths of azimuth, and $1.25 <$ |eta| $< 1.5$. Two rings (east and west) of 72 trapezoidal counters perpendicular to the beamline and placed inside the toroid steel cover $360^0$ and form the TSU, covering the range $1.3 < |\eta| < 1.5$. Figure 3.23 shows a graphical view of the BMU drift tubes and the BSU counters.

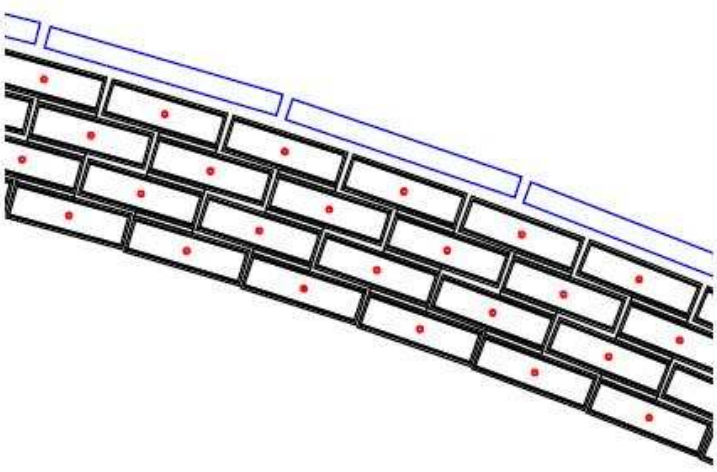

Figure 3.23: Graphical view of part of the BMU drift tubes and the BSU counters.

### 3.2.5 Trigger System

In the Tevatron the protons and antiprotons collide every 396 ns. These collisions produce a very large number of events that their vast majority are not interesting for the high energy physics studies. The goal of the triggering system is to select the interesting events and remove the minimum bias events. This a is very important procedure if one considers that the cross section of the minimum bias events is about 9 orders of magnitude bigger than that of the $t\bar{t}$ production. The triggering system should be efficient enough as it should reduce the data acquisition rate from 2.53 MHz to less than 75 Hz that is the tape writing speed.

The CDF triggering system consists of 3 Levels, that each one reduces the rate and passes the interesting information to the next one. The Level 1 system uses hardware and processes the information from the calorimeters, the muon detectors and the COT. It finds tracks of charged particles and combines them with information from the calorimeters and the muon detectors, counts physical objects and measures the total and missing transverse energy. The Level 2 system uses hardware and performs limited event reconstruction. The Level 3 system uses the full detector information and performs full event reconstruction. The diagram of the CDF triggering system is shown in Figure 3.24.

#### Level 1 Trigger System

The Level 1 is a hardware synchronous system that processes and makes a acceptance/rejection decision of an event in every beam crossing. The decision is made based on the number and the energy of the electrons, the photons, the muons, the jets

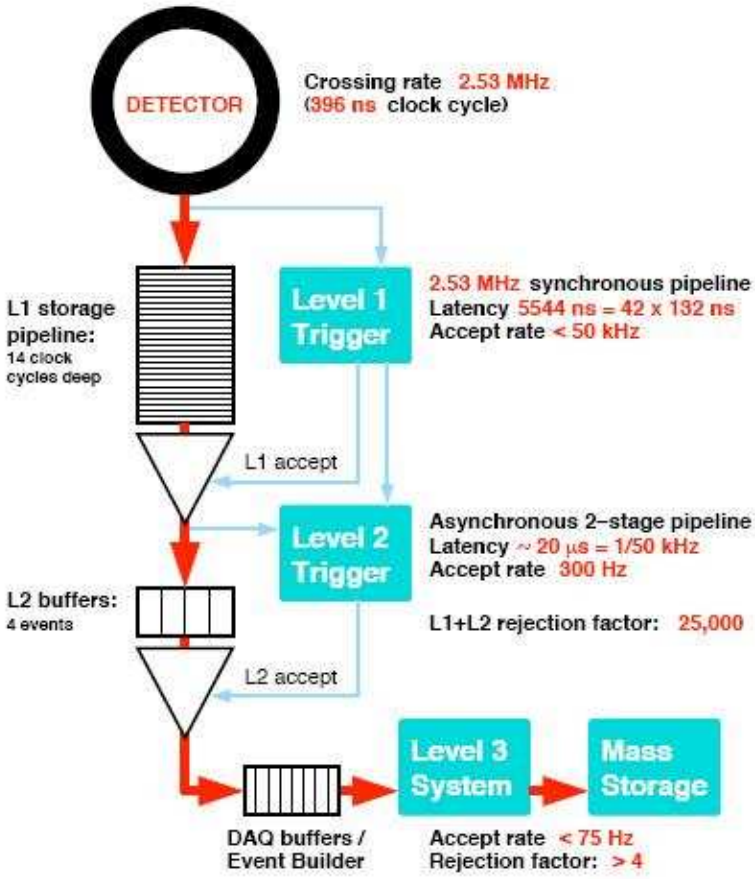


Figure 3.24: Diagram of the CDF triggering system

and the $\not\!\!E_T$ . The input information comes from the calorimeters, the muon detectors and the COT tracker. One of the most important tasks of this level is the track finding and the combination of the tracks with the information from the calorimeters and the muon detectors.

There are three synchronous processing streams. The L1CAL that finds electromagnetic (e/m) objects, the L1MUON that finds muon objects and the L1TRACK that carries the track information. The L1CAL performs two tasks: a) object trig-

gering to find e/m objects and jets by applying trigger threshold to the individual calorimeter trigger towers and b) global triggering to evaluate the $\sum \mathrm{E_T}$ and the $\not\!\!E_T$ after summing the energy from all the towers. The L1MUON provides single and dimuon objects from signal hits in the scintillators of the muon systems and are called primitives. For the wire chambers the primitives are deduced from patterns of hits or pair of hits on the wires and are used as muon stubs, depending on the chamber that they are found. The L1TRACK uses the information from the XFT and XTRP processes. The XFT - eXtremely Fast Tracker - identifies high momentum tracks from the COT. The specifications of the XFT are to have a very high tracking efficiency >96%, a momentum resolution $\Delta \mathrm{P_T}/\mathrm{P_T^2} < 2\%$, an azimuthal resolution >6 mrad and a low $\mathrm{P_T}$ cutoff set at 1.5 GeV/$\mathrm{c}^2$. The XTRP - eXTRaPolation Unit - receives the tracks from the XFT and distributes the tracking information to the 3 Level 1 subsystems, the level 2 processor and the SVT - Silicon Vertex Trigger -. The L1TRACK simply receives the tracking information from the XTRP. Finally the 3 level 1 subsystems deliver their information to a decision card forming the Global Level 1 that makes the final level 1 decision. The level 1 system makes a decision 5.5 $\mu$s after the collision and reduces the event rate to 50 KHz. The steps described above are illustrated in the block diagram of Figure 3.25.

**Level 2 Trigger System**

The level 2 triggering system consists of 4 asynchronous processors. The processing starts when an event is written to one of the four processors and while it is analyzed no event is accepted from the level 1 system. In level 2 a limited event reconstruction

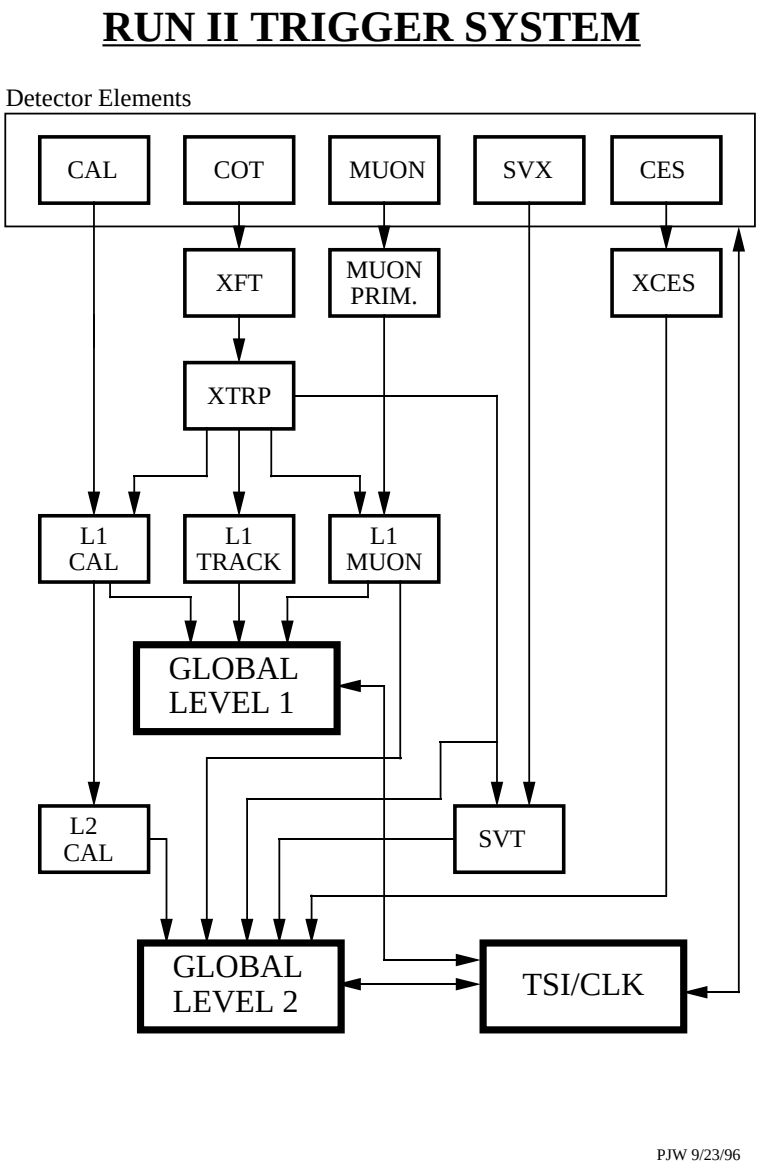


Figure 3.25: Block diagram of the CDF Level1 and Level2 triggering system.

is performed. The procedure is the following. Buffers receive level 1 information from the L1MUON and the XFT as well as from the XSEC that carries the e/m calorimetric shower maximum information. At the same time the L2CAL processes information from the calorimeters and the SVT finds tracks from the SVX. The L2CAL uses an

algorithm to reduce the jet trigger rate. The XSEC reduces the trigger rate of the electrons and the muons using the shower maximum information from the CES. The SVT uses the data from the SVX detector and combines it with the tracks from the XFT to obtain the impact-parameter information. It computes track parameters with resolution comparable to that of the offline analysis. When all data are collected they are processed by the four processors forming Global Level 2 and the final decision is made. The level 2 system makes a decision in about 20 $\mu$s and reduces the event rate to 300 Hz.

**Level 3 Trigger System**

The level 3 triggering system does a full event reconstruction in processor farms using the full detector information [47]. A schematic of the three levels of the CDF trigger is shown in Figure 3.26 As for the Level 1 and the Level 2 the event rate is very high it is impossible to perform a full event reconstruction at these stages. The role of the two first steps of the triggering system is to use small and predefined event segments and make decisions. While they are making their decisions, the event pieces are stored in about 140 FrontEnd FE crates. When the Level 2 makes a decision the event fragments are sent from the FE to the Event Builder EVB that assembles them to a data block. The Level 3 receives a complete but disordered data block from the EVB. Because of the low event rate the Level 3 has now the time to fully reconstruct the event and make the final trigger decision. The event is sent to the Event Server Logger that writes the data to the disks and deliver a small fraction to consumers for online monitoring.

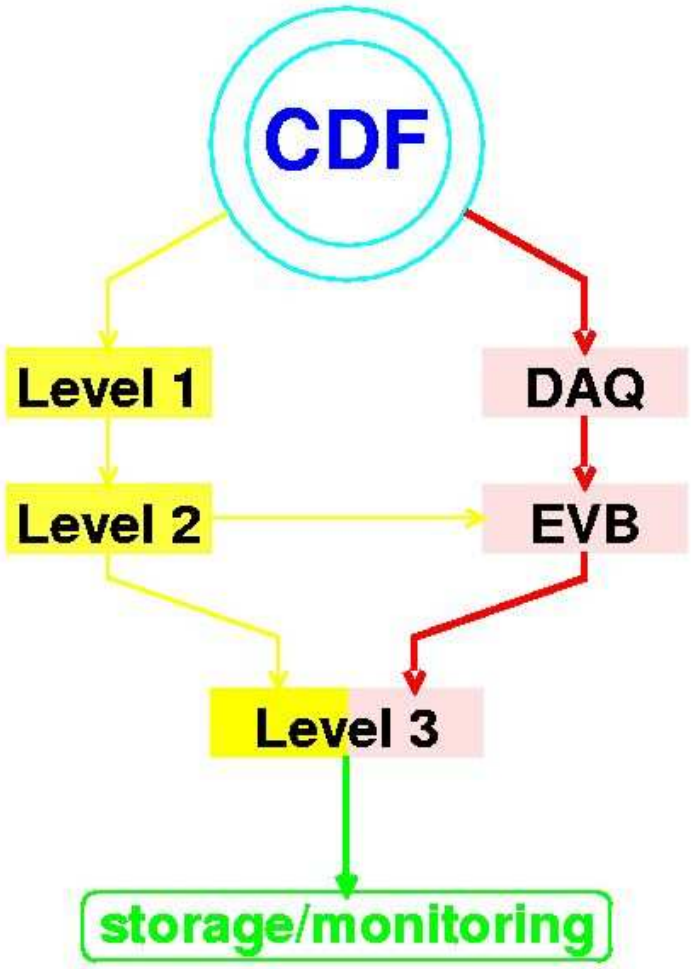


Figure 3.26: Schematic diagram of the three levele of the CDF trigger.

The event fragments are assembled in the EVB in two steps. First they are concentrated in 15 EVB crates and following they are sent to one of the 16 Level 3 subfarms where they are finally assembled and processed. Each of the 15 EVB crates reads data from a group of FE. The EVB has 3 components that are controlled by the Scanner Manager. There are 16 Level 3 subfarms that are the logical subdivisions of the Level 3 farm.

The Level 3 farm reconstructs the event and applies a software trigger. The input event rate is 300 Hz and the output and final rate is 75 Hz. It consists of 250 Linux PCs that are divided in 16 independent subfarms.

# Chapter 4

## Event Selection

This section describes the criteria used to select the $t\bar{t}$ to the dilepton channel events and the set of data and Monte Carlo samples that are used.

## 4.1 Dilepton Selection

The typical $t\bar{t}$ decay to the dilepton channel ($t\bar{t} \rightarrow bl\nu_l\bar{b}l'\bar{\nu_l'}$) consists of two leptons of high transverse momentum $P_T$ and opposite sign, at least two jets with high transverse energy $E_T$ and large missing transverse energy $\not\!\!E_T$ because of the two escaping neutrinos. The raw $\not\!\!E_T$ is defined as the negative vector sum of all the calorimeter towers, electromagnetic and hadronic.

$$\not\!\!E_T = -\sum_{\text{towers}} E_i \sin\theta_i n_i \tag{4.1}$$

where $E_i$ is the the energy deposited in the i tower of the calorimeter, $n_i$ is the transverse unit vector pointing to the tower of the vector and $\theta_i$ is the polar angle of the line pointing from the z coordinate of the event vertex to the $i_{th}$ tower. All towers

above a certain threshold are counted in the sum. The electromagnetic and hadronic towers that contain energy deposited from muons are excluded.

The data used for this analysis are triggered high $P_T$ leptons. The central electron and muon trigger requirements for the two first levels of the trigger tree is a cluster in the electromagnetic calorimeter or hits on the muon chambers combined with a track from the COT for both cases. The level 3 trigger requires $E_T$ or $P_T > 18$ GeV/c.

A set of tight cuts are used for the leptons, the jets and the event variables in order to identify as precisely as possible the $t\bar{t} \rightarrow$ dilepton events and remove the background processes that give similar dilepton final signatures.

To select the candidate $t\bar{t}$ events the following criteria were applied [48] :

- 2 leptons of $P_T$ >20 GeV/c. At least one lepton should be isolated
- 2 or more jets with $E_T$ >15 GeV/c and $|\eta| < 2.5$
- $\not\!\!E_T$ >25 GeV
- the angle between $\not\!\!E_T$ and any lepton or jet to be greater than $20^0$, if $\not\!\!E_T$ <50 GeV. This cut is named L-cut and aims to the rejection of events with mis-measured $\not\!\!E_T$ from jets pointing to the calorimeter cracks and of the $Z \rightarrow \tau\tau$ events.
- Z veto for the same flavor events with invariant mass in the 76-106 GeV/$c^2$ Z mass window. Z veto cut is defined as MetSig = $\not\!\!E_T / \sqrt{\sum E_T} > 4\sqrt{\text{GeV}}$, where the variable is named Met Significance. The $\sum E_T$ is calculated as the sum of the transverse energies in all the calorimetric towers, corrected for any muon

$P_T$. The cut MetSig $> 4\sqrt{\text{GeV}}$ results to a reduction of the total background by about 25% mainly at the DY channel.

- $H_T > 200$ GeV [49], where as $H_T$ is defined as the scalar sum of the transverse momentum of the two leptons and the jets plus the $\not\!\!E_T$ of the event. This cut has a strong discriminating power between the $t\bar{t}$ and the background events. It suppresses the background events with dilepton final states, as their initial state is usually lighter than that of the $t\bar{t}$.

- the two leptons should have opposite sign

Following, the detailed definitions of the criteria imposed to the leptons are described:

Central Electrons

- $E_T$: The transverse energy of the electrons measured as the energy deposited in the central electromagnetic calorimeter multiplied with $\sin\theta$, where $\theta$ is the polar angle between the best track pointing the EM cluster. The cut is set to $E_T$ >20 GeV/c.

- $P_T$: The track transverse momentum of the electrons as measured in the trackers by their curvature in the magnetic field. The cut is set to $P_T$ >10 GeV/c.

- Isolation: The energy in the cone $\Delta R = \sqrt{\Delta\eta^2 + \Delta\phi^2}$ around the electron cluster excluding the electron cluster divided by the transverse energy of the electron. The electrons can either be isolated or not, where they are considered isolated if they contain 90% of their total transverse energy within the cone.

Therefore the isolated central electrons should have Iso<0.1 and the opposite for the nonisolated.

- $E_{had}/E_{em}$: The ratio of the energy deposited in the hadronic over the electromagnetic calorimeter. The electrons are expected to deposit almost all of their energy in the electromagnetic calorimeter and almost none to the hadronic. Therefore this ratio should be very small. From test beams it has been found that $E_{had}/E_{em} < 0.055 + 0.00045E_{em}$, where $E_{em}$ is measured in GeV.

- E/P: The ratio of the transverse energy deposited in the calorimeter over the momentum measured in the tracker. The electrons radiate as they pass through the detector and the photons produced through the bremsstrahlung process deposit their energy in the calorimeter together with the electrons as they are almost collinear. The cut is set to E/P<2.

- $L_{shr}$: This variable compares the energy in the CEM tower adjacent to the seed tower. The cut is set to $L_{shr} < 0.2$.

- $Z_0$: This variable designates the intersection of the track with the beam axis in the r-z plane. The cut is set to $|z_0| < 60$ cm.

- $\chi^2_{strip}$: This is $\chi^2$ comparison between the CES shower profile and the same quantity measured from test beam electrons. It is required that $\chi^2_{strip}$ <10.

- $CES\Delta Z$: This is the distance between the track and the CES cluster, extrapolated in the r-z plane. It is required that $|\Delta Z| < 3.0$ cm.

- signed $CES\Delta X$: This is the distance between the track and the CES cluster,

extrapolated in the r-$\phi$ plane times the charge of the electron. It is required that $-3 < \Delta X < 1.5$ cm.

Plug Electrons

- $E_T$: It is required that $E_T$ >20 GeV/c. The energy and direction is taken from the PEM calorimeter cluster, where the z position is taken as that of the highest $P_T$ object. The direction of any matched track is not used.

- Fiducial $\eta$: To have the energy of the electron precisely measured the shower should deposit most of the energy in the active volume of the plug calorimeter. This requires that the electron is fiducial to the PES -Plug Electromagnetic Shower detector. This assures that the shower position is away from the tower boundaries. The detector $\eta$ of the best matching 2d PES cluster is used as a cut to determine the fiduciality. It is required that $1.2 < \eta < 2.0$.

- Isolation: It is required that Iso<0.1. Nonisolated plug electrons are not allowed for this analysis.

- $E_{had}/E_{em}$: It is required that $E_{had}/E_{em} < 0.05$.

- $Z_0$: This variable designates the intersection of the track with the beam axis in the r-z plane. The cut is set to $|z_0| < 60$ cm.

Muons

- $P_T$: The track transverse momentum of the muons as measured in the trackers by their curvature in the magnetic field. The cut is set to $P_T$ >20 GeV/c.

- Isolation: The energy in the cone $\Delta R = \sqrt{\Delta\eta^2 + \Delta\phi^2}$ around the muon cluster excluding the muon cluster divided by the transverse energy of the muon. The muons can either be isolated or not, where they are considered isolated if they contain 90% of their total transverse energy within the cone. Therefore the isolated muons should have Iso<0.1 and the opposite for the nonisolated.

- $E_{had}$: The energy that the muon deposits to the hadronic calorimeter. It is required that $E_{had} < 6, \max(0, 0.0028(P - 100))$ GeV. The cut value increases for muons with momentum P>100 GeV/c.

- $E_{em}$: The energy that the muon deposits to the electromagnetic calorimeter. It is required that $E_{em} < 2, \max(0, 0.0115(P - 100))$ GeV.

- $|\Delta X|$: The distance in the r-$\phi$ plane between the extrapolated track and the stub at the muon chamber radius. If the muon has a stub at the CMU or the CMP chamber, it is required that $|\Delta X| < 7$ cm and $|\Delta X| < 5$ cm respectively. Accordingly if it has a stub at the CMX then $|\Delta X| < 6$ cm.

- COT|d0|: The 2-dimensional impact parameter of the best matched track, with respect to the COT beam spot position, if the track did not use silicon hits. It is required that $|d0| < 0.2$ cm.

- SVX|d0|: The 2-dimensional impact parameter of the best matched track, with respect to the SVX beam spot position, if the track did use silicon hits. It is required that $|d0| < 0.02$ cm.

- $Z_0$: The cut is set to $|z_0| < 60$ cm.

Generally, it is required that at least one of the leptons in the dilepton pairs is isolated. The terminology used to distinguish the different kind of leptons is listed in Table 4.1:

| **Lepton Name** | **Description** |
|---|---|
| **CEM** | central isolated electrons |
| **NICEM** | central nonisolated electrons |
| **PHX** | plug isolated electrons |
| **CMUP** | isolated muons with a stub in both the CMU and CMP detectors |
| **NICMUP** | nonisolated muons with a stub in both the CMU and CMP detectors |
| **CMU** or **CMP** | nonisolated muons with a stub in the CMU or CMP detector |
| **NICMU** or **NICMP** | nonisolated muons with a stub in the CMU or CMP detector |
| **CMX** | isolated muons with a stub in the CMX detector |
| **NICMX** | nonisolated muons with a stub in the CMX detector |
| **CMIO** | isolated stubless muons |

Table 4.1: Terminology and description of the different lepton types.

It is finally required that at least one of the leptons in the dilepton pair is of the type CEM, PHX, CMUP and CMX.

## 4.2 Data and Monte Carlo Samples

The results presented in this study are obtained by using data collected by the CDF detector from December 2004 to March 2007 and are reprocessed with version 6.1.4 of the CDF reconstruction software. They correspond to an integrated luminosity of 1.8 $fb^{-1}$. The data taking is divided to run numbers according to the experiment runs. The data sets used, corresponding to the quoted time interval, are from run number 141544 to 237795. Only centrally triggered electrons and muons are used. Events triggered by plug electrons are ignored. For the MC samples, the

events are generated with version 6.1.4mc patch "c" in the range 141544-212133. This corresponds to the first 1 $fb^{-1}$ of data taking. Physics objects like, electrons, muons, jets and missing transverse energy are defined and classified with the standard TopEventsModule method, used by the CDF Top and Electroweak groups [50] and are saved in "topNtuple" format both for data and Monte Carlo events. The events are required to pass the version 17 of the good run list [51] - official CDF list that contains the run numbers that have been checked and validated based on the performance of the detector. Runs 222141, 222418, 229664, 230536, 231179, 231241, 231334, 233028, 236653, 235056 and 236040 are excluded.

The $t\bar{t}$ samples for top masses from 152 GeV to 200 GeV, generated with Pythia 6.216, were used. The sources of background in the $t\bar{t} \rightarrow$ dilepton channel are the following:

- diboson (WW/WZ/ZZ) to dilepton decays
- W$\gamma$ to dilepton decays
- DY (Z$\rightarrow \tau\tau$, Z $\rightarrow$ ee, Z $\rightarrow \mu\mu$) to dilepton decays
- Fakes from jets faking leptons

To model the main sources of background the following official CDF Monte Carlo samples were used [52]:

- itopww/itopwz/itopzz for the diboson WW/WZ/ZZ processes
- ztopt2 for Z$\rightarrow \tau\tau$
- ztopzb, ztop3p, xtoppb, ztop3p, ytop3p for Z$\rightarrow$ ee

- ztopzt, ztop8p, xtoppc, xtop8p, ytop7p for Z$\rightarrow \mu\mu$
- rewk28 and rewk29 for W(ev)$\gamma$ and W($\mu$v)$\gamma$ respectively

The fakes background is determined from the data. The diboson background samples were generated with Pythia 6.216 [53]. The DY processes were generated with Alpgen v2.10 [54] + PYTHIA v 6.325. The W$\gamma$ processes were generated with Baur [55].

# Chapter 5

## Background Studies

This section describes the background processes that contaminate the $t\bar{t}$ to dilepton signal. It reports the background expectations at 1.8 $fb^{-1}$. It demonstrates the lepton $P_T$ spectra of the background processes that are used for the top quark mass analysis.

## 5.1 Background Expectations

Extensive studies have been performed for the background estimation at 1.8 $fb^{-1}$ [48]. Table 5.1 summarizes the Standard Model expectations for the $t\bar{t}$ signal events - for $M_{top} = 175$ GeV/$c^2$- and backgrounds for this luminosity, for the different dilepton pairs. Table 5.2 summarizes the information for the different jet multiplicity (jet bins).

## 5.2 Diboson backgrounds

The diboson background is estimated using the MC samples referred to section 4.2. Applying the typical dilepton criteria we selected the diboson events. The

| Events per 1.8 fb$^{-1}$ after all cuts | | | | |
|---|---|---|---|---|
| Source | ee | $\mu\mu$ | e$\mu$ | $\ell\ell$ |
| WW | 1.44±0.26 | 1.64±0.29 | 3.27±0.55 | 6.35±1.05 |
| WZ | 0.62±0.11 | 0.46±0.08 | 0.40±0.07 | 1.48±0.24 |
| ZZ | 0.43±0.34 | 0.43±0.34 | 0.15±0.12 | 1.01±0.79 |
| W$\gamma$ | 0.15±0.16 | 0.00±0.00 | 0.00±0.00 | 0.15±0.16 |
| DY$\rightarrow \tau\tau$ | 0.68±0.33 | 1.38±0.53 | 2.44±0.82 | 4.50±1.34 |
| DY$\rightarrow ee + \mu\mu$ | 4.20±1.10 | 5.18±1.22 | 0.90±0.41 | 10.28±2.30 |
| Fakes | 3.08±1.43 | 5.58±2.28 | 5.61±2.68 | 14.28±5.37 |
| Total background | 10.60±2.08 | 14.68±2.90 | 12.77±3.17 | 38.06±7.44 |
| $t\bar{t}$ ($\sigma = 6.7$ pb) | 19.02±1.46 | 21.30±1.63 | 47.16±3.60 | 87.47±6.66 |
| Total SM expectation | 29.62±3.05 | 35.98±3.90 | 59.93±5.84 | 125.53±12.80 |
| GEN6 DATA | 27 | 39 | 59 | 125 |

Table 5.1: Summary table by lepton flavor content of background estimates, $t\bar{t}$ predictions and final candidate events in 1.8 fb$^{-1}$ of data. The quoted uncertainties are the sum of the statistical and systematic uncertainties.

$P_T$ distributions are presented in figure 5.1(a), (b) and (c) for WW, WZ and ZZ respectively.

## 5.3 Drell-Yan

### 5.3.1 $Z/\gamma* \rightarrow$ ee and $Z/\gamma* \rightarrow \mu\mu$

The DY background is estimated using high $\not\!\!E_T$ data events in the Z region ($76 < M_{ll} < 106$ GeV) [48]. In this region the majority of the data dilepton events comes from $Z/\gamma*$ decays. The DY contamination is estimated as the number of these events corrected for non-DY decays and increased by the remaining DY contamination in the DY continuum region. This background has therefore two contributions: a) events in the Z region $N_{in}$ that pass the Z veto cut (MetSig = $\not\!\!E_T / \sqrt{\sum E_T} > 4\sqrt{\text{GeV}}$) and b)

| Events per 1.8 fb$^{-1}$ vs Njet bins | | | | | |
|---|---|---|---|---|---|
| Source | 0j | 1j | $\geq$ 2j | $H_T$ | $H_T$, OS |
| WW | 95.81±8.93 | 26.57±2.93 | 9.97±1.71 | 6.61±1.09 | 6.35±1.05 |
| WZ | 7.85±0.68 | 7.84±0.58 | 2.97±0.42 | 2.26±0.36 | 1.48±0.24 |
| ZZ | 5.90±4.56 | 2.74±2.11 | 1.37±1.07 | 1.19±0.93 | 1.01±0.79 |
| W$\gamma$ | 18.71±4.78 | 5.18±1.44 | 1.44±0.54 | 0.15±0.16 | 0.15±0.16 |
| DY$\rightarrow \tau\tau$ | 2.41±0.57 | 11.15±1.87 | 8.79±2.98 | 4.50±1.34 | 4.50±1.34 |
| DY$\rightarrow ee + \mu\mu$ | 27.78±5.47 | 20.71±4.16 | 15.91±4.85 | 10.28±1.76 | 10.28±2.30 |
| Fakes | 60.60±17.07 | 42.83±12.86 | 30.08±9.32 | 21.22±7.21 | 14.28±5.37 |
| Total background | 219.06±27.47 | 117.02±17.48 | 70.54±14.25 | 46.21±8.51 | 38.06±7.44 |
| $t\bar{t}$ ($\sigma = 6.7$ pb) | 0.45±0.05 | 11.71±0.91 | 93.07±7.08 | 89.75±6.83 | 87.47±6.66 |
| Total SM expectation | 219.51±27.49 | 128.73±18.07 | 163.60±20.01 | 135.97±13.24 | 125.53±12.80 |
| GEN6 DATA | 218 | 140 | 175 | 139 | 125 |

Table 5.2: Summary table of background estimates, $t\bar{t}$ predictions and events in 1.8 fb$^{-1}$ of data for each jet bin after all cuts but before the $H_T$ and Opposite Charge requirements are applied and in the 2 jet bin after applying only the $H_T$ cut. The last column contains the candidate events with all cuts applied. The quoted uncertainties are the sum of the statistical and systematic uncertainties.

events outside the Z region $N_{out}$. The total number of DY events is:

$$N^{DY} = N_{in} + N_{out} \tag{5.1}$$

The $N_{out}$ contribution is estimated by deducting the number of data events $N^{DT}$ in the Z peak from the number of background events $N^{BG}$ in the same region. As $N^{BG}$ are considered all the non-DY background expectations - diboson, Z$\rightarrow \tau\tau$ and fakes. The events for both cases have been selected in the high $\not\!\!E_T$ region ($\not\!\!E_T$ >25 GeV) and are required to have pass the L-cut (definitions of cuts described in the Event Selection section). To estimate the $N_{out}$, the difference $N^{DT}$-$N^{BG}$ that refers to the events inside the Z peak has to be multiplied with the ratio $R^{out/in}$ of dilepton events outside over inside the Z peak. Therefore:

$$N_{out} = R^{out/in}(N^{DT} - N^{BG}) \tag{5.2}$$

The $N_{in}$ contribution is similarly estimated by deducting the number of data events

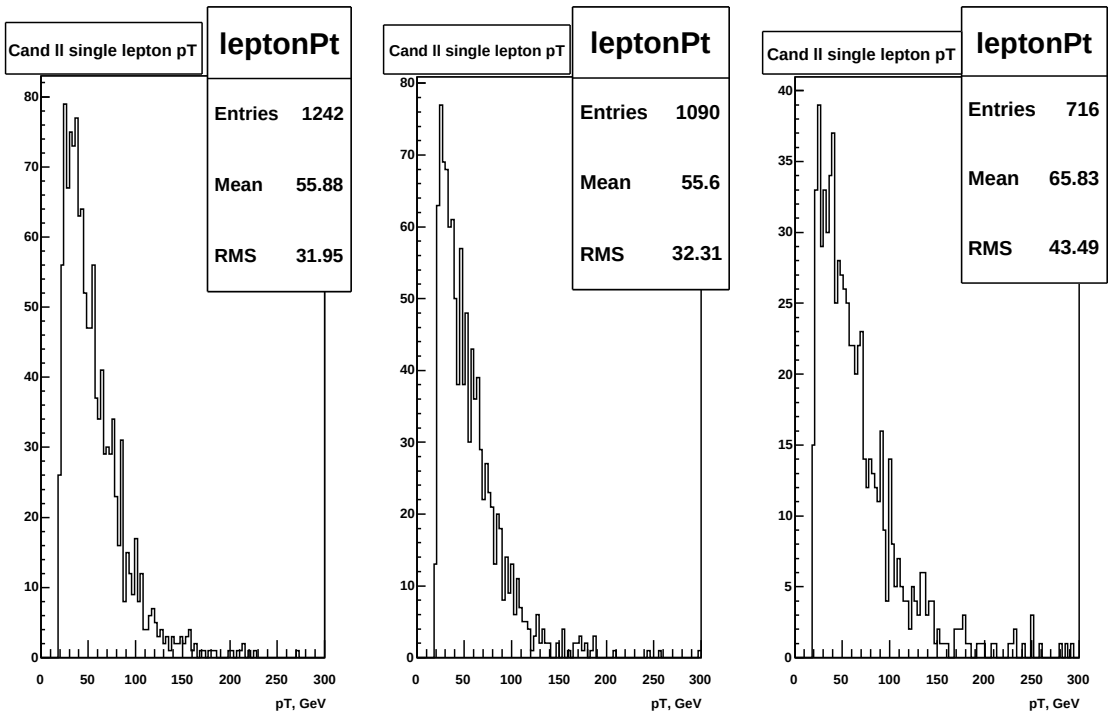


Figure 5.1: $P_T$ distributions for (a)ww, (b)wz, (c)zz

$N^{DT}$ in the Z peak from the number of background events $N^{BG}$ in the same region. For this case the events have been selected in the high $\not\!\!E_T$ region ($\not\!\!E_T$ >25 GeV), are required to have pass the L-cut but to fail the Z veto cut (MetSig = $\not\!\!E_T / \sqrt{\sum E_T}$ > $4\sqrt{\text{GeV}}$). To estimate the final $N_{in}$, the difference $N^{DT}$-$N^{BG}$ that refers to the events that fail the Z veto cut has to be multiplied with the ratio $R^{high/low}$ of dilepton events with high over low MetSig (Missing $E_T$ significance).

$$N_{in} = R^{high/low}(N^{DT} - N^{BG}) \tag{5.3}$$

Both the $R^{out/in}$ and $R^{high/low}$ are estimated using Monte Carlo DY/Z events.

The final $N^{DY}$ contamination is estimated by multiplying the $N_{in} + N_{out}$ with efficiencies for the $H_T$ and opposite sign cuts. These efficiencies are also estimated using Monte Carlo events.

Finally the DY contamination for DY$\rightarrow \mu\mu$ events to the e$\mu$ category is also taken into consideration. This effect appears when one very energetic final muon radiates a photon. The photon, that is collinear with the muon, deposits its energy in the EM calorimeter. Therefore the muon track associated with the energy in the EM from the photon is interpreted as an electron. The missed muon gives a significant $\not\!\!E_T$ to the event.

In order to have the most accurate representation of the DY transverse momentum distribution the Z decays to the full invariant mass spectrum, from 20 to 600 GeV, are considered. The processes $Z/\gamma* \rightarrow ee + 2p, 3p$ and $Z/\gamma* \rightarrow \mu\mu + 2p, 3p$ were selected to increase the statistics. The samples used are described in section 4.2. The $P_T$ distribution of the processes was formed after taking into account the cross-section of the different sub-processes. The $Z/\gamma* \rightarrow ee$ and $Z/\gamma* \rightarrow \mu\mu$ distribution is presented in Figure 5.2.

### 5.3.2 $Z/\gamma* \rightarrow \tau\tau$

The $Z/\gamma* \rightarrow \tau\tau$ background is estimated using the MC sample referred to section 4.2 by applying the typical dilepton criteria. The $P_T$ distributions is presented in Figure 5.3.

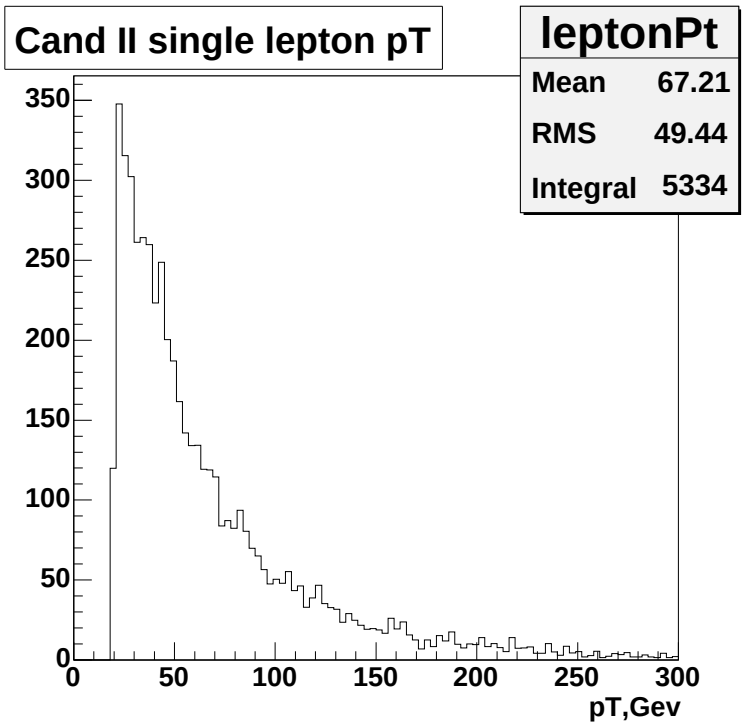


Figure 5.2: $P_T$ distributions for $Z/\gamma* \rightarrow ee$ and $Z/\gamma* \rightarrow \mu\mu$ events

## 5.4 Fakes background

Jets can fake an electron when they deposit a large amount of energy in the EM calorimeter and have a high $P_T$ track. They can fake a muon if their hadron activity produces pions or kaons with a later shower.

W+jet events can produce a "dilepton" final state when a jet fakes to be a lepton. If additionally these events are accompanied with more than two jets and large $\not\!\!E_T$ all the dilepton selection criteria are fulfilled. To evaluate this background contribution we weight the fakeable jets in the W+jets events with a fake rate probability. The fake rate is a lepton type dependent probability that a fakeable object, that is an

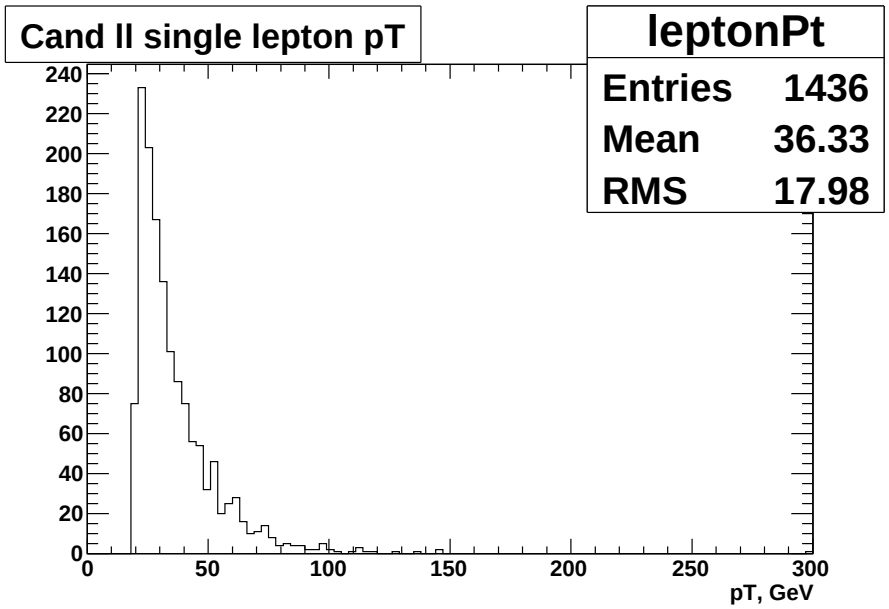


Figure 5.3: $P_T$ distributions for $Z/\gamma* \rightarrow \tau\tau$ $P_T$ distribution

object which shares some of the jets and some of the high $P_T$ lepton characteristics, can be reconstructed as a good lepton. The fake rates have been calculated from jet50 samples - QCD data samples that the trigger jet has raw $E_T$ >50 GeV [48].

A fakeable object [56] is narrowly defined as an EM object with HAD/EM energy deposition $< 0.125$ or a muon with E/p$< 1$. Depending on the geometrical region where the fakeable points to, we define separate fakeable categories for CEM and PHX electrons (TCEM and TPHX), and for CMUP, CMX, CMU/CMP and CMIO muons (TMUO, TCMX, LMUO and LMIO). For non isolated leptons (NCEM and NMUO), we require that the fakeable object is also non isolated. Using the JET50 QCD data sample, we calculated the fake rates reported in Table 5.3 and shown in Figure 5.4. The six variable-width $p_T$ bins ([20–30] GeV, [30–40] GeV, [40–60] GeV, [60–100] GeV,[100–200] GeV and $\geq$ 200 GeV) are chosen so as to have reasonable

| Fake Lepton | JET 50 Fake Rate | | | | | |
|---|---|---|---|---|---|---|
| | [20-30] GeV | [30-40] GeV | [40-60] GeV | [60-100] GeV | [100-200] GeV | $P_T > 200$ GeV |
| TCEM | 0.0455 ± 0.0038 | 0.0308 ± 0.0028 | 0.0209 ± 0.0017 | 0.0214 ± 0.0028 | 0.0465± 0.0121 | 0.0000 ± 1.0000 |
| NCEM | 0.0084 ± 0.0002 | 0.0060 ± 0.0003 | 0.0054 ± 0.0004 | 0.0040 ± 0.0009 | 0.0000 ± 1.0000 | 0.0000 ± 1.0000 |
| TPHX | 0.1019 ± 0.0061 | 0.0925 ± 0.0061 | 0.0987 ± 0.0048 | 0.1405 ± 0.0111 | 0.1410 ± 0.0394 | 0.0000 ± 0.0000 |
| TCMUP | 0.2514 ± 0.0321 | 0.3203 ± 0.0412 | 0.3125 ± 0.0321 | 0.5274 ± 0.0413 | 0.4571 ± 0.0842 | 0.0000 ± 1.0000 |
| TCMX | 0.4483 ± 0.0653 | 0.5952 ± 0.0757 | 0.6230 ± 0.0621 | 0.5926 ± 0.0669 | 0.3636 ± 0.1450 | 1.0000 ± 0.0000 |
| LMUO | 0.4759 ± 0.0415 | 0.3558 ± 0.0469 | 0.3692 ± 0.0423 | 0.4444 ± 0.0552 | 0.6000 ± 0.0980 | 0.0667 ± 0.0644 |
| LMIO | 0.1672 ± 0.0096 | 0.2230 ± 0.0179 | 0.2532 ± 0.0219 | 0.3593 ± 0.0316 | 0.2679 ± 0.0418 | 0.5266 ± 0.0364 |
| NMUO | 0.0481 ± 0.0013 | 0.0296 ± 0.0015 | 0.0197 ± 0.0016 | 0.0182 ± 0.0031 | 0.0306 ± 0.0123 | 0.0588 ± 0.0571 |

Table 5.3: JET50 fake rates vs lepton $P_T$ range for different feakeable objects.

statistics in each bin. To mitigate possible trigger biases, we require that there is at least one "trigger" jet of raw $E_T > 50$ GeV in the event and that the fakeable object is not reconstructed in a cone of $\Delta R < 0.4$ around the "trigger" jet. Real lepton contamination from W or Z bosons is assumed to be negligible and is not corrected for.

In order to represent the $P_T$ spectrum of the fakes background we use data and select events with one fakeable and one W lepton. The $P_T$ distribution of the fakes background is shown in Figure 5.5.

## 5.5 W$\gamma$

The contribution of W$\gamma$ background in the candidate region is about 0.4%. From the available MC samples only 1 event survives the dilepton selection. Therefore, this background is not included to the total $P_T$ distribution. The only reason that it is considered is that it has a significant contribution to the control (low jet multiplicity) regions.

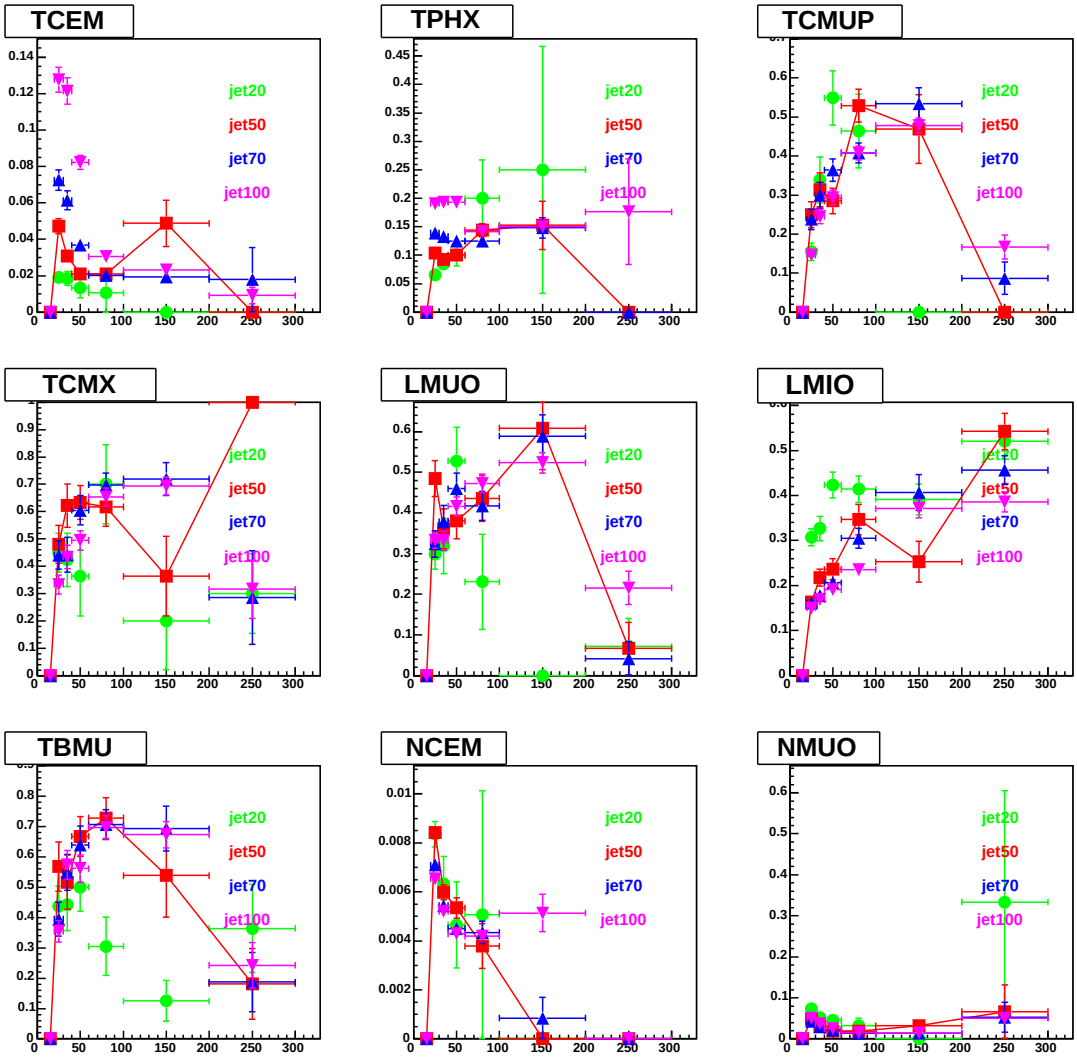


Figure 5.4: Fake rate estimates versus lepton $P_T$ for each fakeable category for 1.8 $fb^{-1}$. The JET50 fake rates, shown in red, are compared to the JET20 (green), JET70 (blue) and JET100 (magenta) fake rates. TBMU fakeable objects are not used in this analysis.

### 5.5.1 Combined background

The leptons' $P_T$ distributions from different background sources are combined to a total lepton $P_T$ distribution. The combination is performed by giving to each

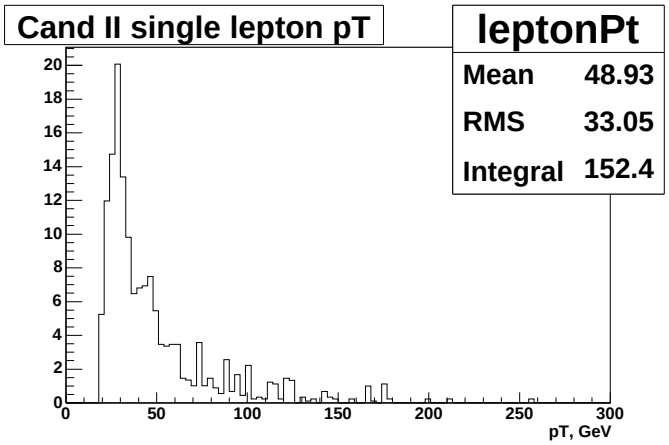


Figure 5.5: $P_T$ distributions for the fake background

background a relative weight according to the estimations presented in Table 5.1. The total background $P_T$ distribution is shown in Figure 5.6.

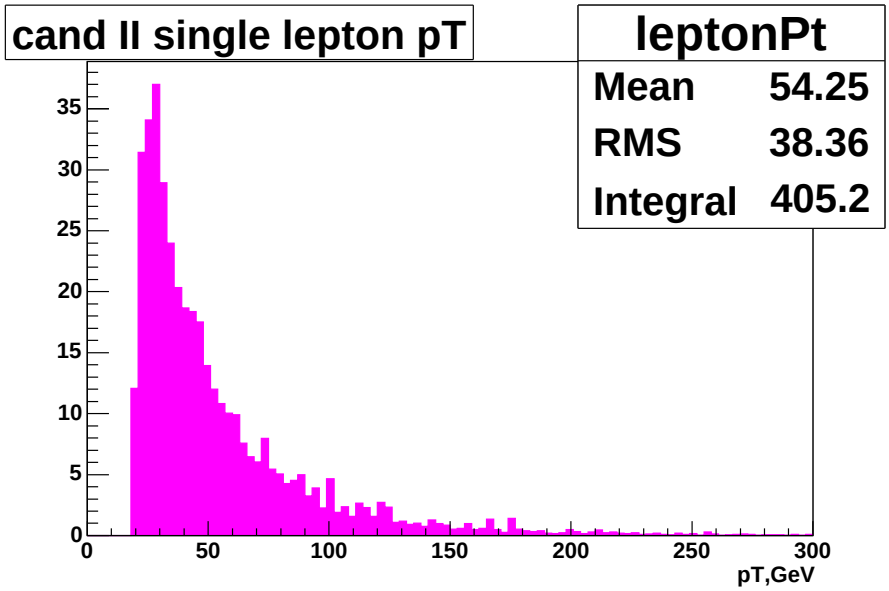


Figure 5.6: $P_T$ distributions for the combined background

The case where the sample consists of two leptons and only 1 jet is used to evaluate how well the background is estimated. This sample is mostly dominated from the background processes, as for the signal events 2 or more jets are required. Two kinematic variables are used for this reason: a) the leptons' $P_T$ spectrum the b) the event $\not{E}_T$ .

The data are compared with the total Standard Model expectation at the 1 jet bin to evaluate how well the total background $P_T$ distribution is estimated. In the 1 jet bin only 10% are top leptons while 90% are background leptons. From Table 5.1 one can observe that the estimated SM expectation is 128.81±17.85 events while there are 140 data events. Although the SM expectation agrees well, within error, with the data, there is still a 12 event deviation, a fact that reflects in Figure 5.7. A Kolmogorov-Smirnov test is performed to test how well the shape of the SM $P_T$ distribution agrees to that of the data. For this reason the SM expectation is normalized to the number of data events (see Figure 5.8). The KS test gives 0.8308. We therefore conclude that the data agree well with the SM expectation as seen from the $P_T$ spectra.

Accordingly, comparing the $\not{E}_T$ spectra at the 1 jet bin for the data and the total SM expectation it is seen that the agreement is still good. The comparison plot is illustrated in Figure 5.9. These tests indicate that the background estimations are within their error correct and that the kinematic distributions of the whole event variables but also of the final leptons are as expected from the data.

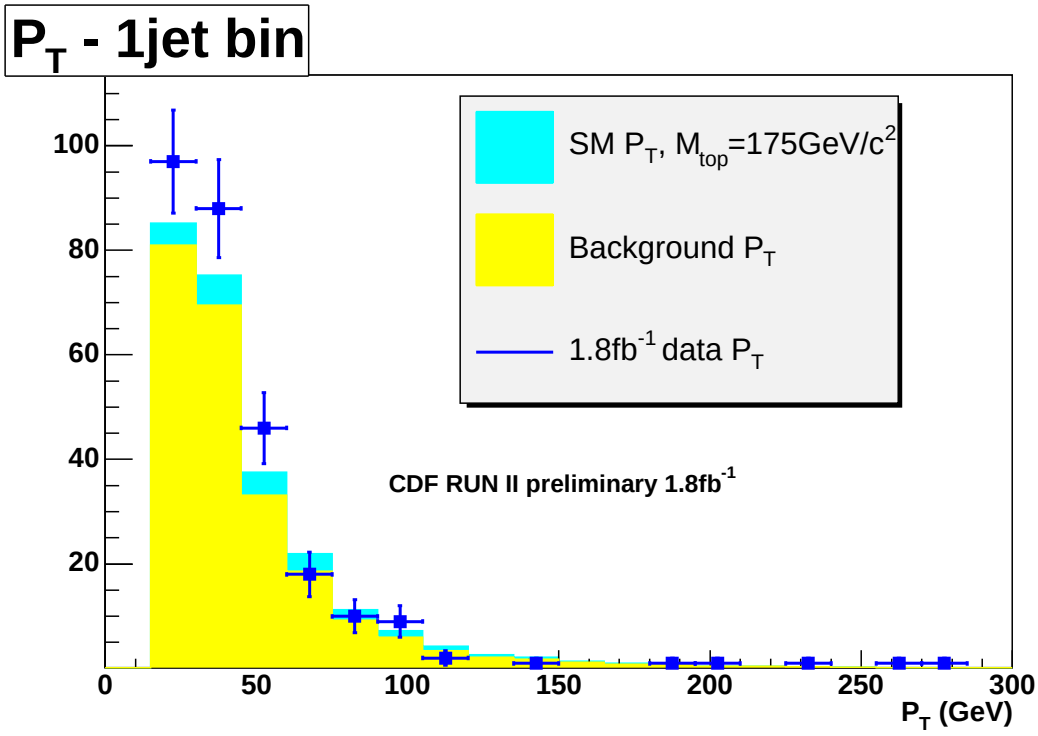


Figure 5.7: $P_T$ distributions for the combined background and the data in the control 1jet bin. The blue points are the data, the aqua histogram is the SM (top+background) expectation and the yellow histogram is the total background

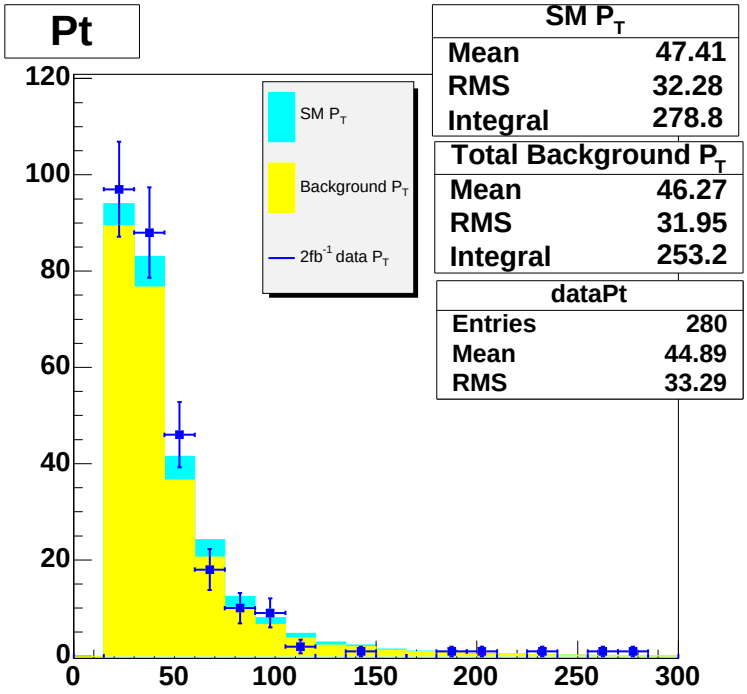


Figure 5.8: $P_T$ distributions for the combined background and the data in the control 1jet bin. The blue points are the data, the aqua histogram is the SM (top+background) expectation (for $M_{top} = 175$ GeV/$c^2$) and the yellow histogram is the total background. The SM model expectation is normalized to the number of data events.

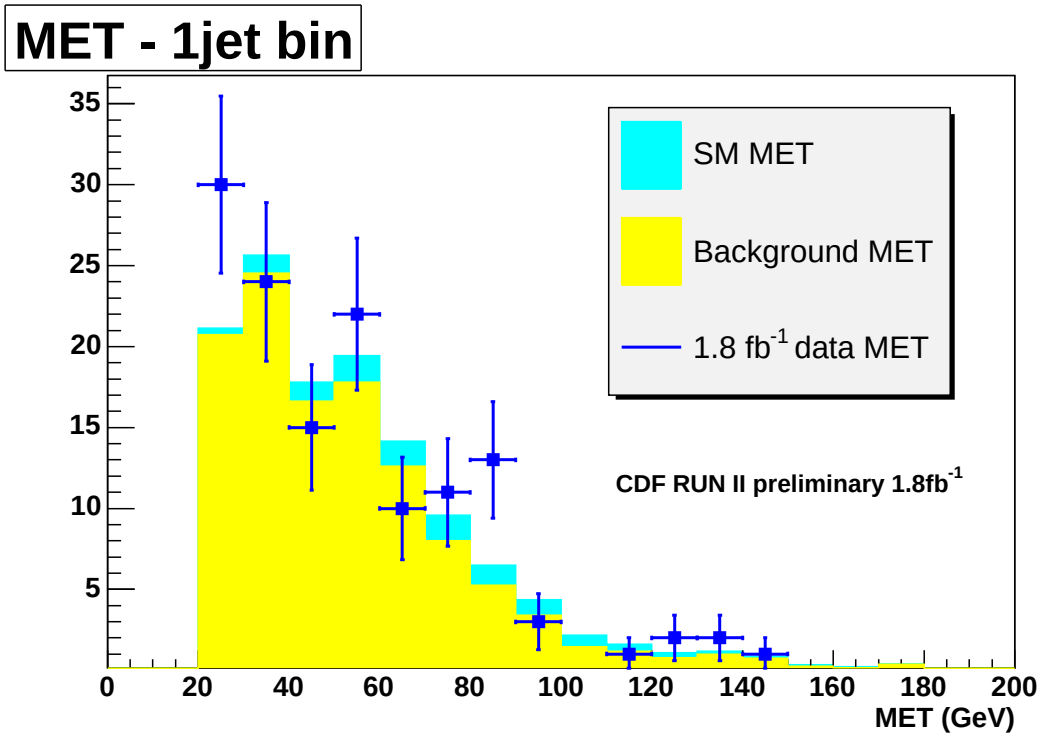


Figure 5.9: $\not\!\!E_T$ distributions for the combined background and the data in the control 1jet bin. The blue points are the data, the aqua histogram is the SM (top+background) expectation and the yellow histogram is the total background

# Chapter 6

## Lepton $P_T$ Sensitivity to the Top Mass

This section describes the sensitivity of the leptons $P_T$ to the top quark mass and the methods that are used for its measurement.

This analysis has been based upon the observation that the leptons' transverse momentum ($P_T$) is sensitive to the top mass [8], [9]. Figures 6.1 and 6.2 show that the dependence of the mean $P_T$ of the leptons on the top mass is linear.

$$P_T = \kappa + \lambda M_{top} \tag{6.1}$$

In Figure 6.1 the mean $P_T$ is derived from the lepton $P_T$ distributions of the mass signal templates generated for different input top masses. In Figure 6.2 each signal template has been combined to the total background template taking into account that the purity of the total sample, as calculated for $M_{top} = 175$ GeV/c$^2$, is $\rho \equiv \frac{\text{signal}}{\text{signal+background}} = 0.70$. Taking the extreme case that only signal exists the sensitivity $\frac{d\langle P_T \rangle}{dM_{top}}$ is $\lambda_S = (13.5 \pm 0.4)\%$. Including the background, as seen from Figure 6.2, the sensitivity is reduced to $\lambda_B = (9.4 \pm 0.3)\%$. This decrease of the slope

is expected since the background contaminates the Monte Carlo samples with events involving no top quarks and thus carrying no $M_{top}$ information. This can be seen by decomposing the $\langle P_T \rangle$ into a 'signal' $\langle P_T \rangle_S$ and a 'background' $\langle P_T \rangle_B$ part:

$$\langle P_T \rangle = \rho \langle P_T \rangle_S + (1 - \rho) \langle P_T \rangle_B \tag{6.2}$$

where $\rho$ is the purity of the sample as defined above. Using Equation 6.1 and the $\kappa_S$ and $\lambda_S$ values we can predict that the $\lambda_B = \rho \times \lambda_S = 9.4 \pm 0.4\%$. The predicted $\lambda_B$ is absolutely consistent with the value that was estimated directly from the samples.

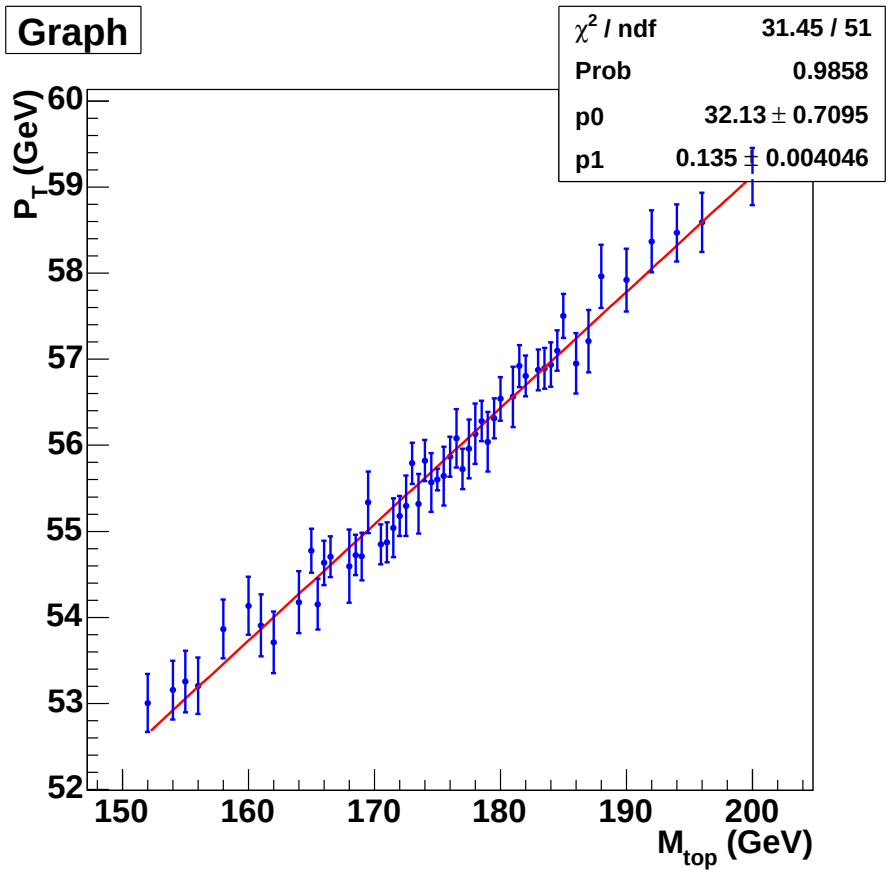


Figure 6.1: Mean lepton $P_T$ vs Top Mass from signal only $P_T$ distributions

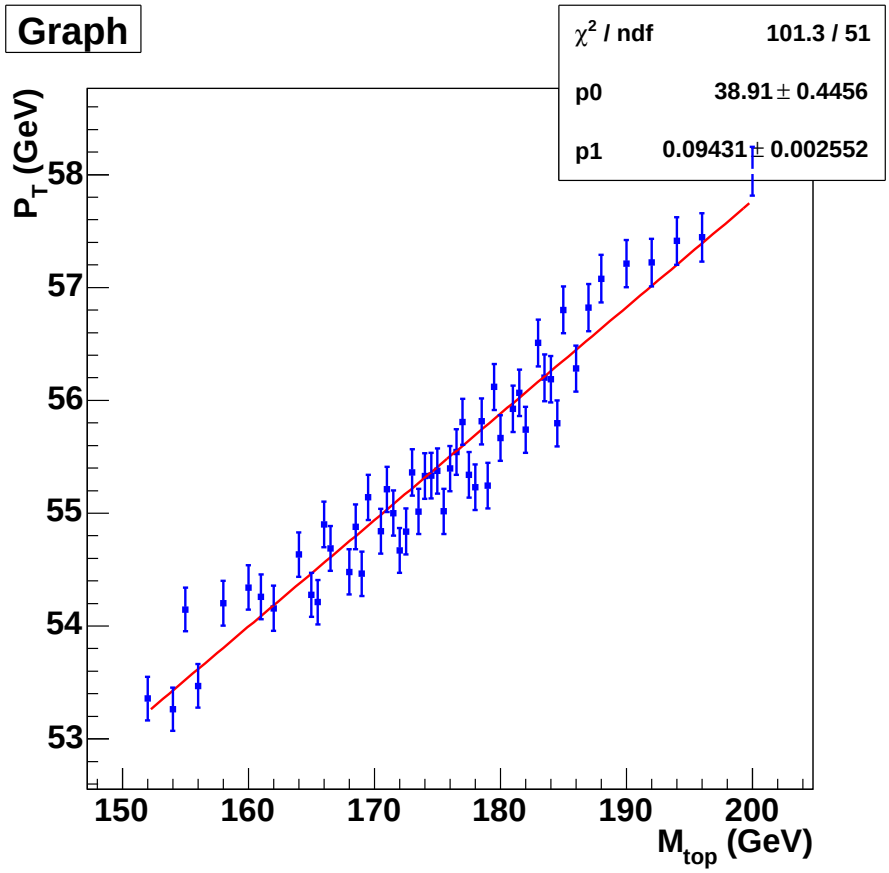


Figure 6.2: Mean lepton $P_T$ vs Top Mass from signal and background $P_T$ distributions

Going to a deeper level, the leptons' $P_T$ distributions are modeled with an analytical function to examine how this function depends on the top mass. Such a function can be the product of a Gamma times a Fermi function as seen in Equation 6.3:

$$F(P_T) = \frac{1}{\Gamma(p+1, c/q)} \left(\frac{P_T}{q}\right)^p e^{-\frac{P_T}{q}} \times \frac{1}{1+e^{c-P_T/b}} \tag{6.3}$$

This function models successfully the shape both of the signal and the background $P_T$ distributions as illustrated in Figures 6.3, 6.4. It has two free parameters p, q, where p is related to the expected rate of leptons with average $P_T$ and q can be

interpreted as the expected average $P_T$ per lepton. For the signal the p, q are mass dependent (see Eq. 6.4, 6.5) but for the background they are constant. The Fermi function models the leptons' $P_T$ cut, setting c=20GeV/c and b=0.1GeV/c. The p and q are parametrized as in the following equations

$$p = \alpha_1 + \alpha_2 M_{top} \tag{6.4}$$

$$q = \alpha_3 + \alpha_4 M_{top} \tag{6.5}$$

For the signal 53 $t\bar{t} \rightarrow$ dilepton samples generated with Pythia 6.2.16 are used, for top quark masses from 152 to 200 GeV/$c^2$. The 53 different lepton $P_T$ distributions are being fit simultaneously to find the optimum coefficients $\alpha_1, \alpha_2, \alpha_3, \alpha_4$ that form the p, q signal parameters, using the maximum likelihood method. The $\chi^2$/dof calculated for the total fit is 2.4. The background p, q parameters are not mass dependent. For consistency they are called $\beta_1, \beta_2$, where p=$\beta_1$ and q=$\beta_2$. Similarly the combined background lepton $P_T$ distribution is being fit and the optimum parameters are found for this template. Table 6.1 shows the results of the signal and background coefficients.

| signal coefficients | value |
|---|---|
| $\alpha_1$ | 1.565 ± 0.067 |
| $\alpha_2$ | -0.00278 ± 0.00037 $GeV^{-1}$ |
| $\alpha_3$ | 6.04 ± 0.25 |
| $\alpha_4$ | 0.0948 ± 0.0014 $GeV^{-1}$ |
| $\beta_1$ | -0.58± 0.25 |
| $\beta_2$ | 48.1± 8.5 $GeV^{-1}$ |

Table 6.1: Signal coefficients $\alpha_1, \alpha_2, \alpha_3, \alpha_4$ that form the mass dependent parameters p and q and background parameters $\beta_1, \beta_2$

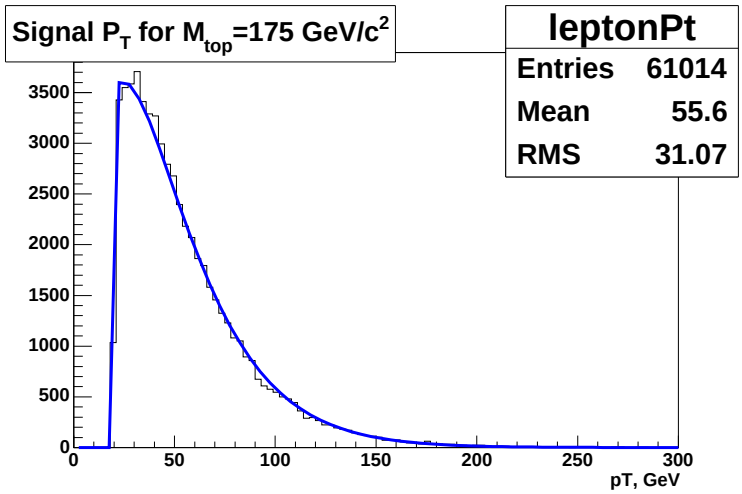


Figure 6.3: Lepton $P_T$ distribution for the signal, generated for top mass $M_{top}$=175GeV compared to the Gamma x Fermi fitting function

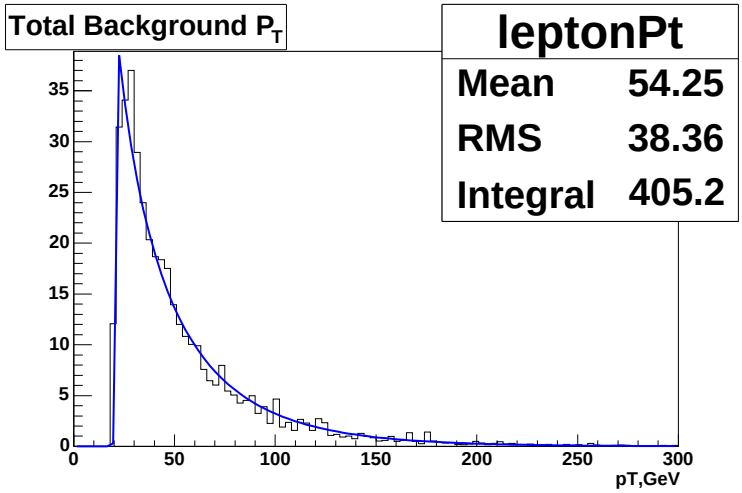


Figure 6.4: Lepton $P_T$ distribution for the combined background compared to the Gamma x Fermi fitting function

The parametrization of the background is validated with a Kolmogorov-Smirnov test. A lepton $P_T$ distribution is created, taking expectation values from the Gamma x Fermi function for different $P_T$ intervals and compare it to the standard background $P_T$ distribution. The new distribution is created by taking 100 $P_T$ expectation values

from 0 to 300 GeV with a step of 3 GeV. Figure 6.5 shows the background $P_T$ distribution (in red), the fit (in blue) and the new histogram from the Gamma x Fermi expectation values (in green). The Kolmgorov-Smirnov test gives 1 and the parametrization is considered successful.

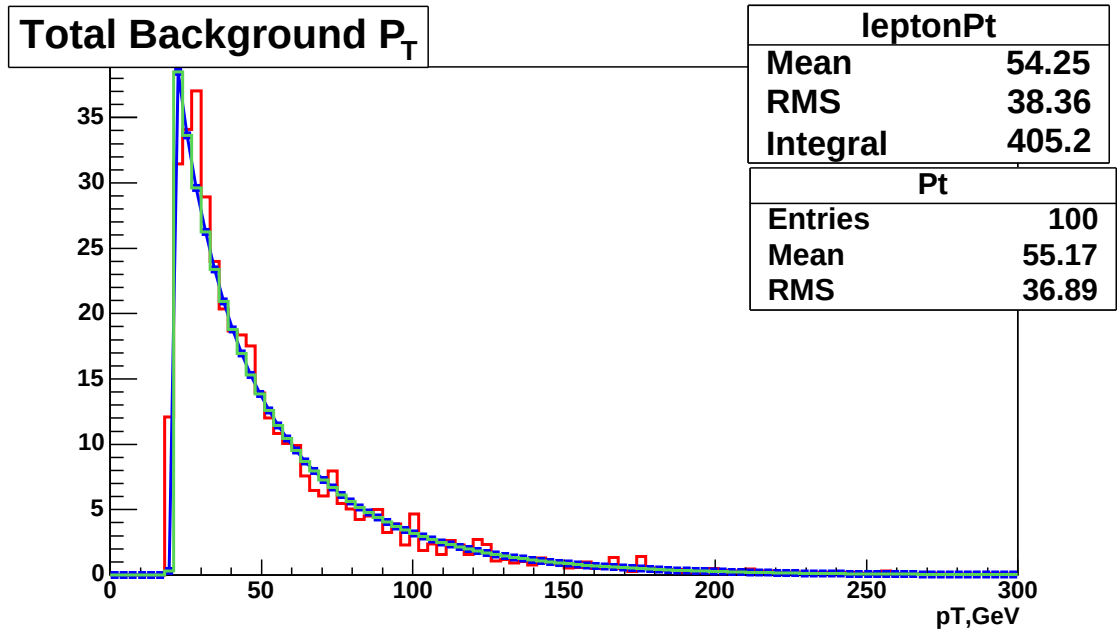


Figure 6.5: Lepton $P_T$ distribution for the combined background (red) compared to the histogram filled with the Gamma x Fermi expectations (green). The blue line represents the Gamma x Fermi fit to the total background.

## 6.1 The two methods for Top Mass Measurement

From the above discussion it follows that two methods can be established for measuring the top mass, both directly dependent to the sensitivity of the leptons' $P_T$ to the top mass. In the first method, the full shape of the signal and background lepton $P_T$ distributions is modeled using the Gamma x Fermi function while the mass is estimated by employing the likelihood minimization procedure. This method from

now on will be denoted as Likelihood (LH). The second method directly exploits the fact that the mean $P_T$ of the leptons is linearly dependent to the top mass as shown in Figure 6.2. This method from now on will be called Straight Line method (SL).

### 6.1.1 Likelihood Method (LH)

This method exploits the full shape of the leptons' $P_T$ distribution of the signal and the background. To arrive to a final mass estimation, $P_T$ values are compared with probability density functions (p.d.f.'s), for signal and background, within a likelihood minimization. The p.d.f's are the Gamma x Fermi functions that have been developed, using the shape parameters referred to in Table 6.1. The likelihood function finds the probability that a given sample of $P_T$ values is an admixture of top→dilepton and background decays with a certain top mass. A probability is assigned that a given $P_{T,i}$ value looks like signal and the probability that it looks like background by comparing it with the corresponding parameterized p.d.f's $P_s$, $P_b$. Also the probability that the number of background events $n_b$ is consistent with the a-priori SM expectation $n_b^{exp}$ is estimated (see Section 5) and similarly that the total number of signal and background events n is consistent with the number of data events N. The number of background events is constrained to its expected statistical uncertainty $\sigma_{nb}$ with a Gaussian. The total number of events is constrained with the use of a Poisson term. The total likelihood function takes the form:

$$\mathcal{L}(P_T) = \mathcal{L}_{shape}(P_T) \times \mathcal{L}_{Bg} \tag{6.6}$$

where,

$$\mathcal{L}_{shape}(P_T) = \frac{(\mathrm{n_s}+\mathrm{n_b})^{\mathrm{N}}\mathrm{e}^{-(\mathrm{n_s}+\mathrm{n_b})}}{\mathrm{N}} \prod_{\mathrm{i}=1}^{\mathrm{N}} \frac{\mathrm{n_s P_s}(\mathrm{P_T^i};\mathrm{M_{top}}) + \mathrm{n_b P_b}(\mathrm{P_T^i})}{\mathrm{n_s}+\mathrm{n_b}} \tag{6.7}$$

and

$$-ln\mathcal{L}_{Bg} = \frac{1}{2}\left(\frac{n_b - n_b^{exp}}{\sigma_{nb}}\right)^2 \tag{6.8}$$

The statistical uncertainty on the top mass is given by the difference between the minimization mass result and the mass at $-ln\mathcal{L}_{max} + 0.5$.

### 6.1.2 Straight Line Method (SL)

This method directly exploits the fact that the mean $\mathrm{P_T}$ of the leptons is linearly dependent to the top mass as shown in Figure 6.2. Equation 6.1 gives:

$$\mathrm{M_{top}} = \frac{\mathrm{P_T} - \kappa}{\lambda} \tag{6.9}$$

The mass that corresponds to a given mean $\mathrm{P_T}$ is found, using the parameters $\kappa_{\mathrm{B}} = 38.91 \pm 0.4\mathrm{GeV}$ and $\lambda_{\mathrm{B}} = 0.094 \pm 0.003$ from the linear fit shown in Figure 6.2. The corresponding statistical error is estimated from Equation 6.10, where $\mathrm{P_T^{rms}}$ is the RMS of the leptons' $\mathrm{P_T}$ distribution and N is the number of candidate leptons.

$$\delta(\mathrm{M_{top}})_{\mathrm{stat}} = \frac{1}{\lambda}\frac{\mathrm{P_T^{rms}}}{\sqrt{\mathrm{N}}} \tag{6.10}$$

### 6.1.3 Comparison of the two methods

The consistency of the two methods is tested by examining whether the shape fitting implementation can reproduce the mean $\mathrm{P_T}$ of the signal histograms. For this

reason the function 6.3 is integrated to determine the mean $P_T$ as a function of the top mass:

$$< P_T >= \int_0^\infty P_s\left(P_T; M_{top}\right) \frac{P_T}{q} dP_T = q\left[1 + p + \left(\frac{c}{q}\right) \frac{e^{-c/q}}{\Gamma(1+p, c/q)}\right] \qquad (6.11)$$

The p, q parameters are determined by the $\alpha_1, \alpha_2, \alpha_3, \alpha_4$ coefficients listed in Table 6.1. Figure 6.6 compares the estimation from this calculation (blue points) with the $P_T$ values estimated from Equation 6.1 (red points) using the fitting parameters $\kappa_S = 32.13 \pm 0.71$ and $\lambda_S = 0.135 \pm 0.004$. The exact values are listed in Table A.2 (Appendix). A very good agreement between the two methods is observed. Finally, the fitted mean $P_T$ of the total background is estimated. The Equation 6.11 is still applied, using the background shape parameters $\beta_1$ and $\beta_2$ listed in Table 6.1. The mean $P_T$ of the total background spectrum is 54.25±1.9 GeV and the shape parameters estimate a mean $P_T$ of 54.24 GeV.

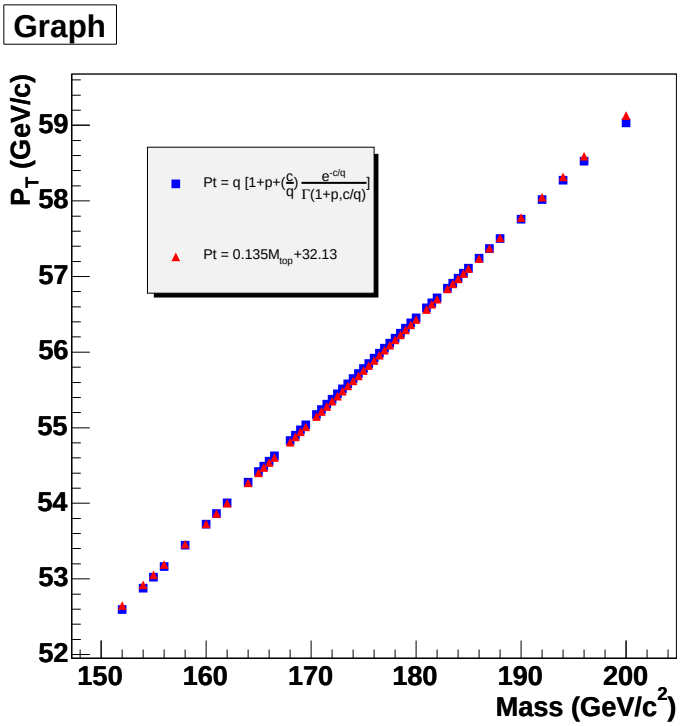


Figure 6.6: Consistency plot for the LH and and SL methods. The red points represent the $< P_T >$ values estimated from Equation 6.1. The blue point represent the $< P_T >$ values estimated from Equation 6.3.

# Chapter 7

## Statistical Studies

This section describes the studies that are performed in order to guaranty the validity of the two presented methods of measuring the mass of the top quark.

The statistical studies are performed with the use of simulated sets of lepton $P_T$ values, called pseudo-experiments (PE). From each generated top sample for top mass from 152 to 200GeV/$c^2$, we reconstruct a set of $P_T$ values randomly selected from the signal and background histograms. For the number of background events in each PE we take a random number from a gaussian distribution with mean the a-priori background expectation and sigma its corresponding uncertainty. This number is finally Poisson fluctuated. For the number of signal events we subtract from the total number of events the "random" number of background events. The simulated set of $P_T$ values are used to perform the statistical studies both for the LH and the SL method. For the studies 200 PE are performed, each corresponding to an integrated luminosity of $\mathcal{L} = 1.8\text{fb}^{-1}$.

The linearity tests examine if the methods return the input top mass value. For

this reason we plot the fitted mass $M_{fit}$ values and the residuals $M_{true} - M_{fit}$ versus the true mass values $M_{true}$. To check the spread in the fitted mass and the estimated statistical uncertainty from the PE, we generate pull distributions for each generated top mass sample according to the formula:

$$\text{Pull} = \frac{M_{true} - M_{fit}}{\sigma} \tag{7.1}$$

where $\sigma$ is the statistical uncertainty in the fitted mass. The pull distribution should have a mean value, within error, 0 and rms consistent with 1.

## 7.1 Statistical Studies for the LH method

According to the methodology described above we form 200 different sets of signal and background lepton $P_T$ values, for each of the generated top mass samples. The number of $P_T$ values forming each set corresponds to the 1.8 $fb^{-1}$ SM expectation. Following the likelihood minimization procedure we estimate the fitted mass value and the corresponding statistical uncertainty for each PE. We gaussian fit each ensemble of PEs for a given mass to estimate the most probable fitted mass and statistical error. The "sanity" tests are performed considering only signal situations and standard signal + background.

Figure 7.1 shows the fitted mass the residual, the pull and the pull rms vs the true mass, for the 53 different samples. For these plots the lepton $P_T$ values are taken only from the signal distributions; the background is considered to be 0. Figure 7.2 displays the same plots when background is included. The exact values per mass are shown in Table A.1 (Appendix A). For both cases the "sanity" tests are healthy.

In detail, the linearity plots $M_{fit}$ vs $M_{true}$ are linearly fitted giving a slope consistent with 1 and an intercept consistent with 0. The residual plots ($M_{true} - M_{fit}$) vs $M_{true}$ fluctuate around 0, with a minor deviation. The pull and pull rms vs $M_{true}$ graphs are fitted with an 1-parameter line and they fluctuate around 0 and 1 respectively. The deviation that appears in the pull tests is much smaller than the statistical fluctuation of the mass measurement, and therefore, no corrections are applied.

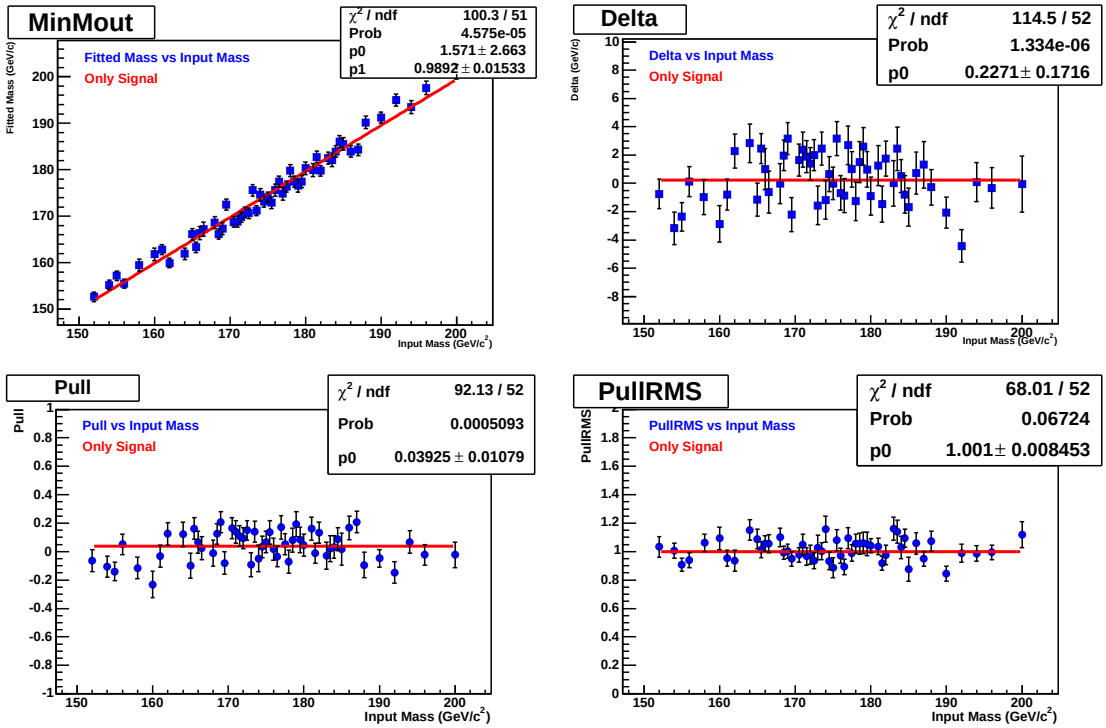


Figure 7.1: (a) fitted mass $M_{fit}$ (b) residual $M_{true} - M_{fit}$ (c) pull and (d) pull rms vs the true mass $M_{true}$. For these plots, 53 mass samples were used for a range from 152 to 200 GeV/$c^2$. Only signal $P_T$ distributions have been considered. All of the above results were obtained with the LH method.

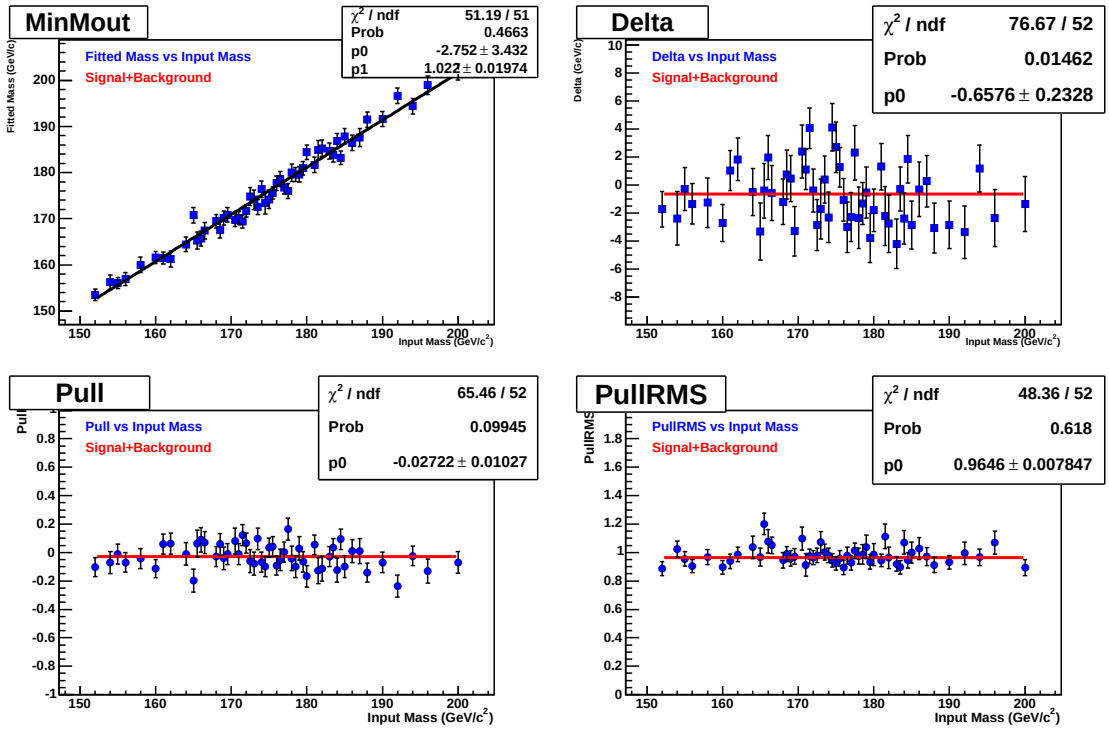


Figure 7.2: (a) fitted mass $M_{fit}$ (b) residual $M_{true} - M_{fit}$ (c) pull and (d) pull rms vs the true mass $M_{true}$. For these plots, 53 mass samples were used for a range from 152 to 200 GeV/$c^2$. Signal+background $P_T$ distributions have been considered. All of the above results were obtained with the LH method.

## 7.2 Statistical Studies for the SL method

Lepton $P_T$ distributions for signal only and signal plus background situations are formed, from the different mass samples. Figure 7.3 displays the fitted masses and the residuals vs the true mass, for the 53 different mass samples, considering only signal situations. Figure 7.4 displays the same plots for signal + background. In both cases the $M_{fit}$ vs $M_{true}$ and $(M_{true} - M_{fit})$ vs $M_{true}$ fits are within the expected values.

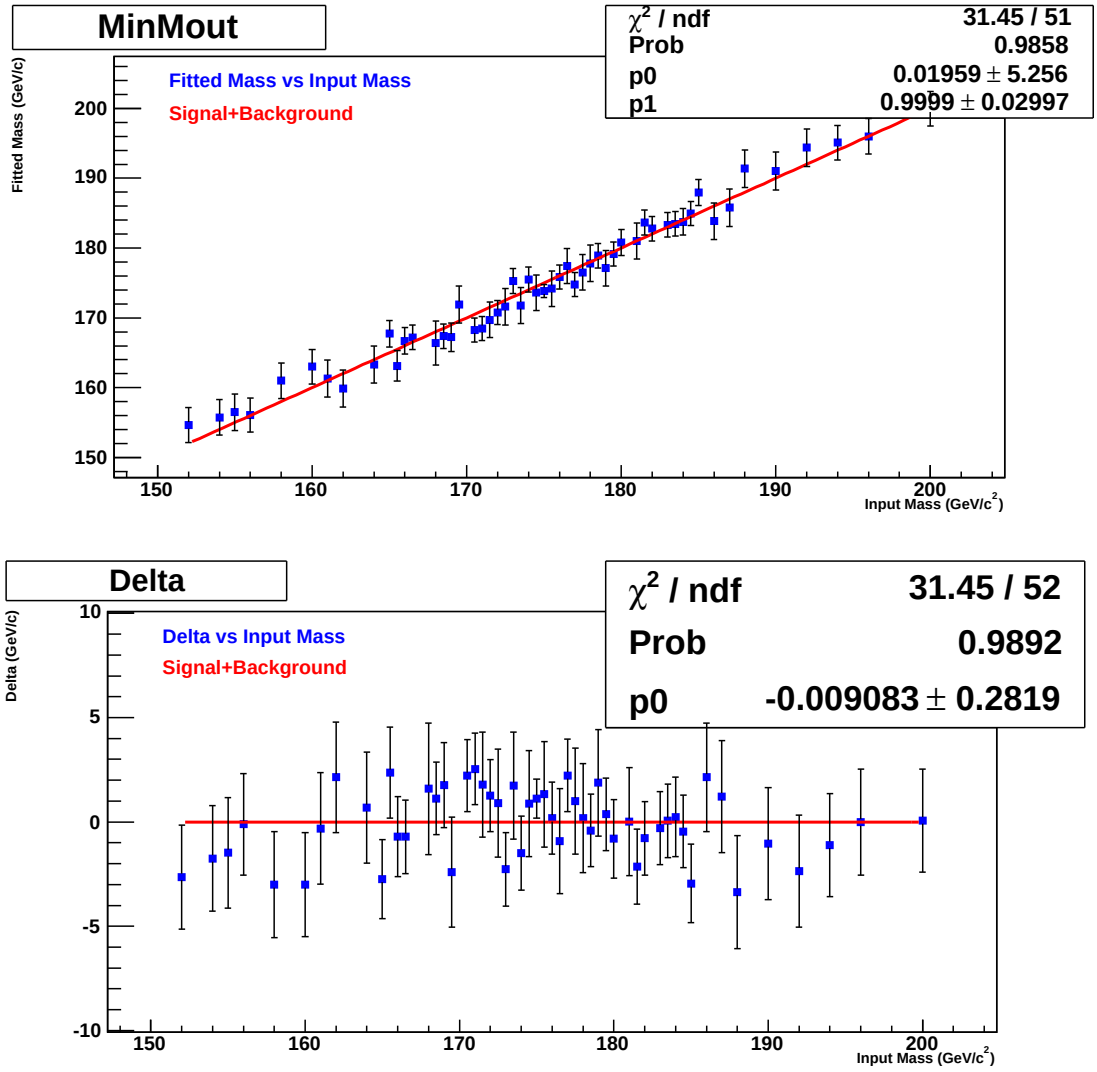


Figure 7.3: (a) fitted mass $M_{fit}$ and (b) residual $M_{true} - M_{fit}$ vs the true mass $M_{true}$. For these plots, 53 mass samples were used for a range from 152 to 200 GeV/$c^2$. Only signal $P_T$ distributions have been considered. All of the above results were obtained with the SL method.

## 7.3 Blind Samples

Figure 7.5 shows the residuals from 10 Pythia blind samples, for which the input mass is unknown. For each of the blind samples 13 PE at 1.2 $fb^{-1}$ were performed, so as to exhaust the statistics of the samples. The top mass was estimated with the

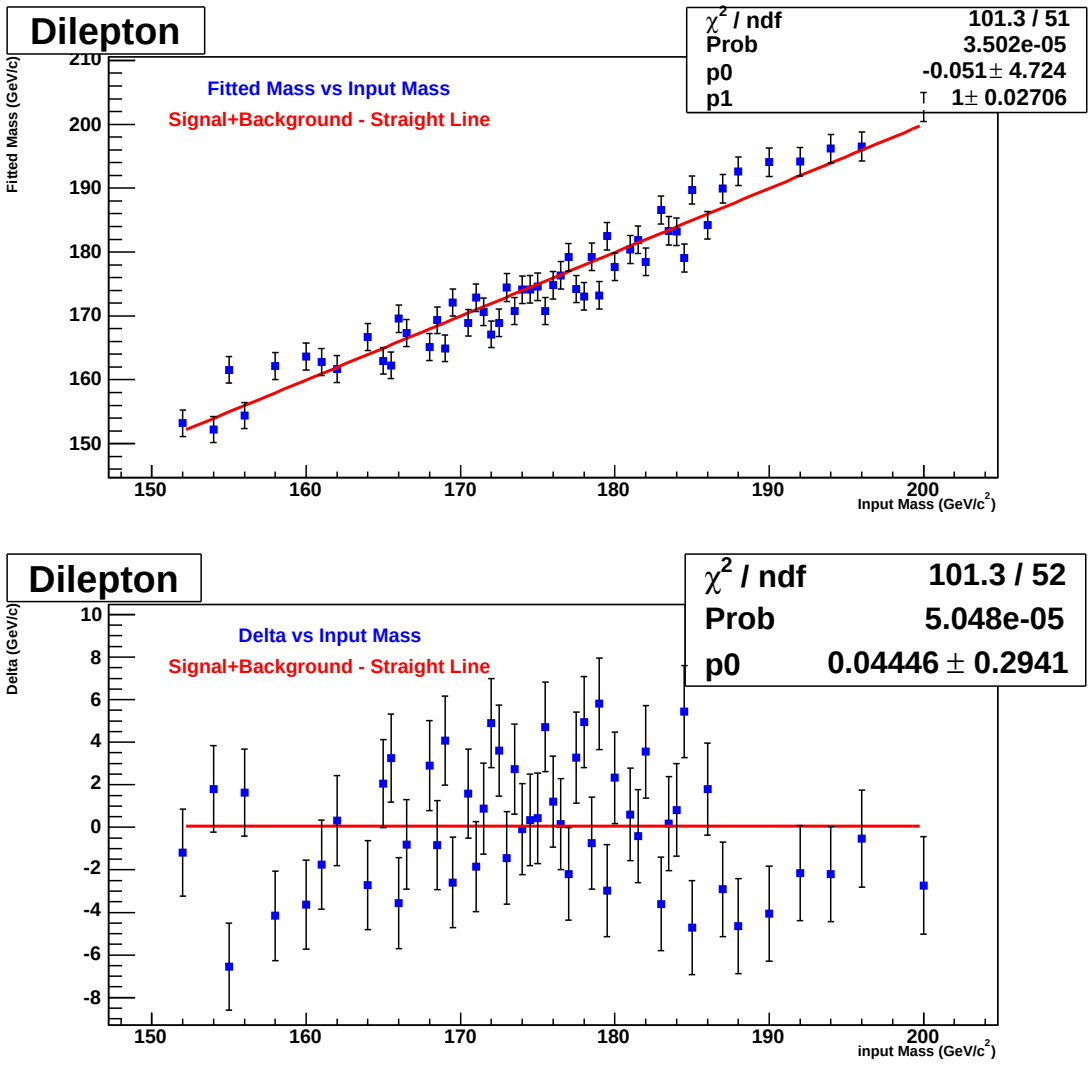


Figure 7.4: (a) fitted mass $M_{fit}$ and (b) residual $M_{true} - M_{fit}$ vs the true mass $M_{true}$. For these plots, 53 mass samples were used for a range from 152 to 200 GeV/$c^2$. Signal+background $P_T$ distributions have been considered. All of the above results were obtained with the SL method.

LH method. Given the statistics of the samples the mean $P_T$ is associated with an error of 0.8 GeV that propagates a statistical error of 9 GeV. Eight out of ten of the estimations are consistent with 0. Still, there are two values that are 2-3 s.d away from 0. Extended studies were performed to find if the origin of this deviation is an

overall bias to the method or is just a statistical effect. Three more Pythia blind samples were generated for this reason, the residuals of which fluctuate around 0 (see Figure 7.6). Additionally a "reverse" test was performed to test if the mean $P_T$ of the signal samples vs the estimated fitted mass give the sensitivity established by the known masses (see Figure 6.1). Indeed, as seen from Figure 7.7, for both of the cases that the mass was estimated only from the signal and the signal+background, the slope and the intercept are consistent with the corresponding known mass values for signal only ($\lambda = 0.135 \pm 0.004$ and $\kappa = 32.13 \pm 0.71$). In Figure 7.8 the mean $P_T$ of the signal+background distribution vs the estimated blind mass is illustrated. The slope and the intercept are also consistent with the corresponding known mass signal+background values ($\lambda = 0.094 \pm 0.003$ and $\kappa = 38.91 \pm 0.44$).

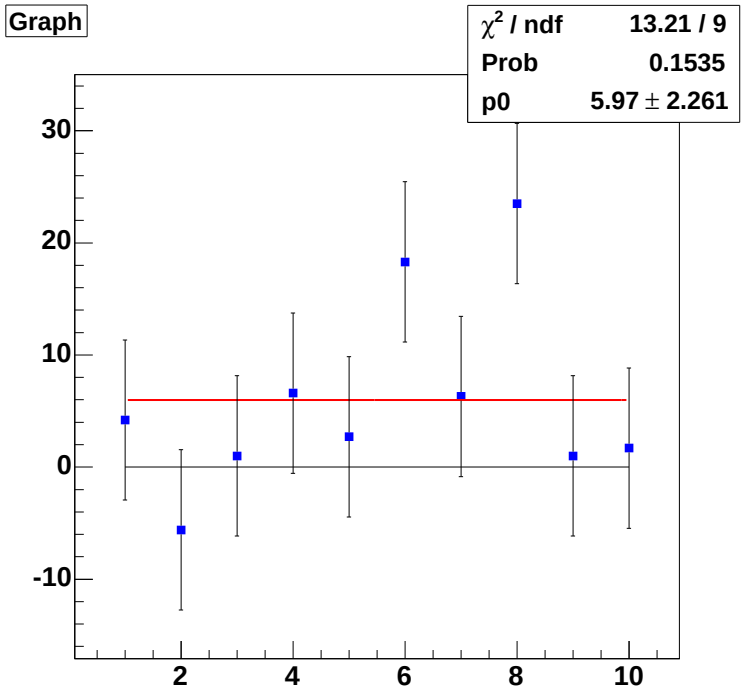


Figure 7.5: Residuals from the 10 blind samples

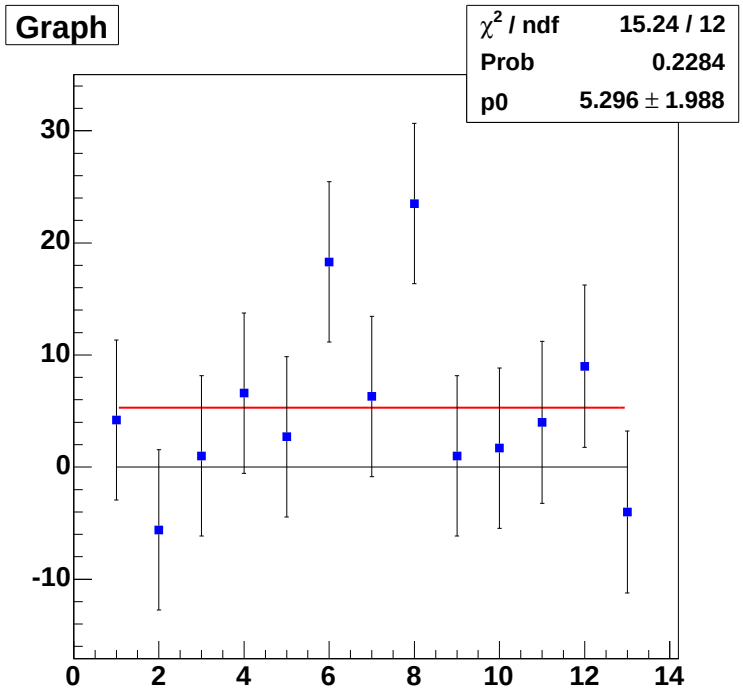


Figure 7.6: Residuals from the 13 samples

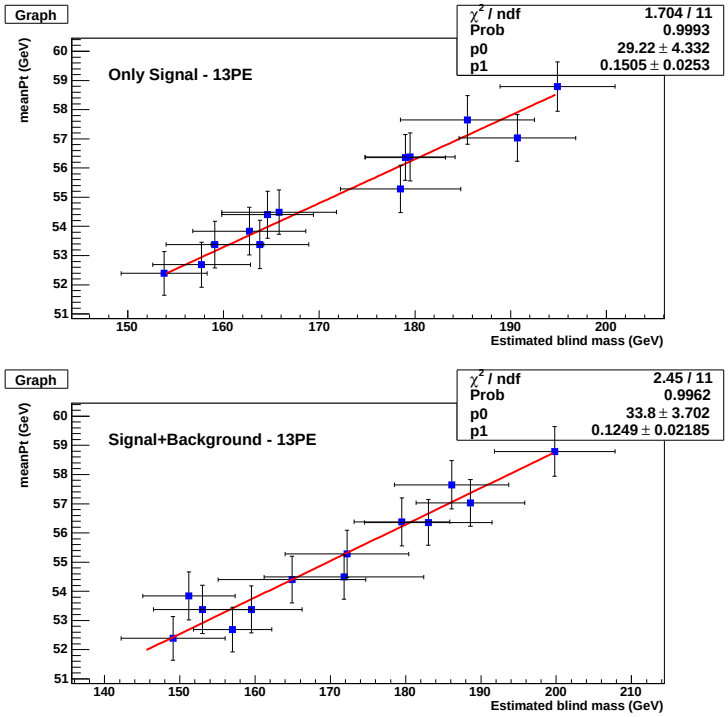


Figure 7.7: mean $P_T$ vs estimated $M_{top}$ for (a) signal, (b) signal+background. The results refer to 13 Pythia blind samples.

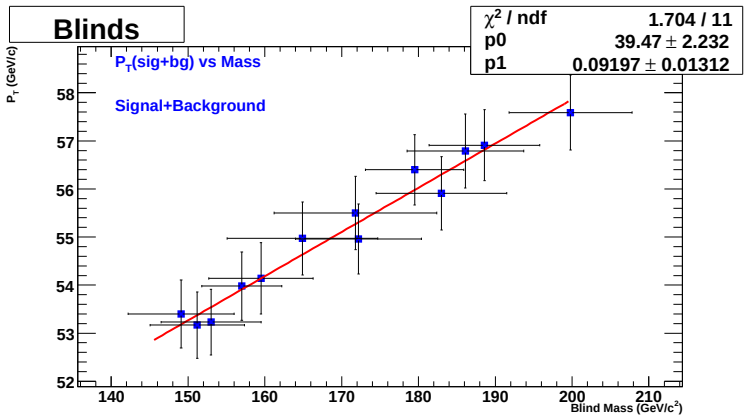


Figure 7.8: Signal+background mean $P_T$ vs estimated $M_{top}$. The results refer to 13 Pythia blind samples.

# Chapter 8

## Systematic Uncertainties

This section discusses the systematic uncertainties involved to the two methods of measuring the top mass.

The anticipated sources contributing to the total systematic uncertainty can be grouped into three main categories. The first group contains the uncertainties to the top mass related to the top signal. The second group involves the uncertainties related to the background. The third one deals with the leptons' $P_T$ scale uncertainty.

A. Signal related systematic uncertainty sources

- Gluon radiation in the initial state (ISR). This error is estimated by using the Pythia v 6.216 samples with "less" and "more" ISR and by performing comparison with the default Pythia v 6.216 sample. All three samples are generated for top mass $M_{top} = 175$ GeV/$c^2$.

- Choice of the Parton Distribution Functions (PDF) for the proton. This error is

estimated by using the Pythia v 6.216 samples that use the PDF sets MRST72 and MRST75 respectively. The comparison is performed with the default Pythia v 6.216 sample. All three samples are generated for a top mass of $M_{top}$ = 175 GeV/$c^2$.

- Choice of the MC generator. This error is estimated by using two different top samples that are generated with different generators. The Herwig v 6.510 sample [57] and the default Pythia v 6.216 sample are used for the comparison. Both samples are generated for a top mass of $M_{top}$ = 175 GeV/$c^2$.

B. Background related systematic uncertainty sources

- Uncertainty because of the background shape. It is considered that the shape of the DY and fake lepton $P_T$ distributions is not known accurately. The lack of this knowledge may cause to a differentiation of the total lepton $P_T$ background shape. This is evaluated by performing shifts on the number of DY and fake events, within their statistical uncertainty, and re-reconstructing the total background lepton $P_T$ distribution.

- Uncertainty because of the background scale, considering the number of background events is known with a 20% accuracy.

C. Scale uncertainty in the measurement of lepton's $P_T$.

- Uncertainty to the top mass because of the uncertainty in the measurement of the leptons' $P_T$. This is evaluated by performing comparisons of the Z $\rightarrow$ ee and Z $\rightarrow \mu\mu$ invariant masses to the Z mass measured at LEP. We use Z $\rightarrow$

dilepton decays from data received in the 0d/0h/0i periods and from the Pythia 6.216 Monte Carlo samples for $Z \rightarrow ee$ and $Z \rightarrow \mu\mu$ decays.

The systematic uncertainties to the top mass can be evaluated with two different methods, depending on how the top mass is estimated. For the LH method, the lepton $P_T$ distributions of the different sources are fit with the Gamma x Fermi function and the top mass that they correspond to is estimated by implementing the likelihood minimization procedure. The uncertainty corresponds to the difference of this mass from the mass of the nominal/default Pythia sample of $M_{top} = 175$ GeV/c$^2$. For the case that the SL procedure is followed, the uncertainty is estimated from Equation 8.1.

$$\langle P_T \rangle = \rho \langle P_T \rangle_{sig} + (1 - \rho) \langle P_T \rangle_{bg} \tag{8.1}$$

The $\langle P_T \rangle_{sig}$ and $\langle P_T \rangle_{bg}$ values depend on the shape of the signal and background $P_T$ distributions. The signal $P_T$ distribution depends on the top quark mass. The purity $\rho$ of the sample needs to be known, which is defined as the number of signal expected events with respect to the total number of expected events and complementary the number $1 - \rho$ of expected background events with respect to the total expectation. According to Table 5.2 the purity is evaluated to be $\rho = 0.70$. The systematic uncertainty to the top quark mass is estimated with Equation 8.2. This formula is derived from Equations 6.10 and 8.1 by applying error propagation.

$$\left(\delta M_{top}^{\langle P_T \rangle}\right)_{syst} = \frac{1}{\lambda} \times \sqrt{\rho^2 (\delta \langle P_T \rangle_{sig})^2 + (1-\rho)^2 (\delta \langle P_T \rangle_{bg})^2 + (1-\rho)^2 (\langle P_T \rangle_{sig} - \langle P_T \rangle_{bg})^2 \left(\frac{\delta n_{bg}}{n_{bg}}\right)^2} \tag{8.2}$$

where $\delta\langle P_T\rangle_{sig}$, $\delta\langle P_T\rangle_{bg}$ are the uncertainties of the mean $P_T$ on the signal and on the background respectively. The first term in Equation 8.2 represents the systematic error on the top mass that is related to the shape of the signal. The second term is similarly related to the uncertainty due to the background shape. The third term estimates the uncertainty related to the background scale, where $\delta n_{bg}$ is the uncertainty on the number of background events $n_{bg}$.

## 8.1 Signal related Systematic uncertainties

This section summarizes the systematic uncertainties that relate to the shape of the signal. The lepton $P_T$ distribution of the signal can be affected by the existence of initial state gluon radiation (ISR), the choice of the PDF in the top generator and finally the choice of the generator itself.

The scattered partons in the $p\bar{p}$ collisions can radiate gluons as seen in Figure 8.1. The gluons can be identified as jets coming from top decays, that is an additional problem especially in the Lepton+jets channel of the $t\bar{t}$ decay. The ISR effects have been studied using DY data [58] where no FSR from gluons exists. It has been proved that the leptons' mean $P_T$ are sensitive to the ISR radiation, a fact that can be quantified by measuring the mean $P_T$ at different $Q^2$ regions (different DY mass regions). For the top, the ISR activity is measured at $Q^2$ corresponding to a DY mass of $2\times M_{top} = 350$ GeV/$c^2$.

In our case the higher the ISR activity the higher the $P_T$ of the final leptons. For the study of this systematic uncertainty two Pythia samples have been used with "more" and "less" ISR. The "more" and "less" ISR are defined with the PARP(61)

and PARP(64) parameters within the Pythia [58], where:

- PARP(61): $\Lambda_{\mathrm{QCD}}$ value in ISR shower, where the difault is D=0.192 GeV
- PARP(64): K factor to the transverse momentum scale of the ISR evolution, used as a scale in $\alpha_{\mathrm{S}}$ and PDFs (D=1)

The following Table 8.1 lists the values of the parameters that are used for "more" and "less" ISR:

| Parameter | moreISR | lessISR |
|---|---|---|
| PARP61(D=0.192 GeV) | 0.384 | 0.100 |
| PARP64(D=1.0) | 0.25 | 4 |

Table 8.1: Pythia parameters for the "more" and "less" ISR samples.

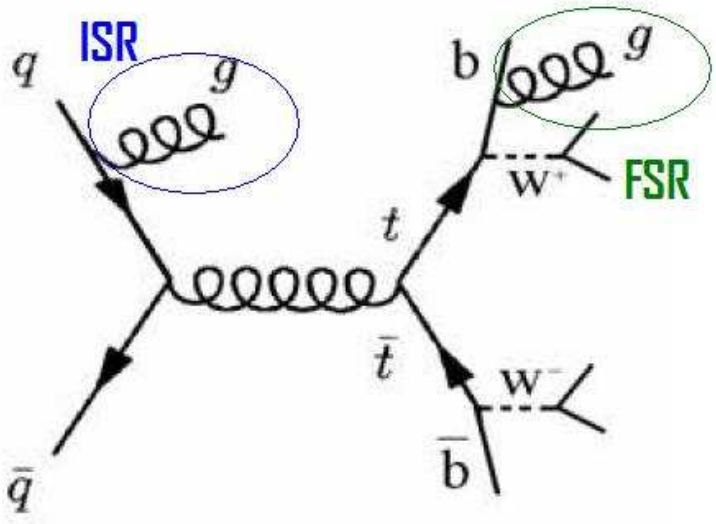


Figure 8.1: ISR and FSR gluon radiation in the production of a $t\bar{t}$ pair.

It is noted here that this analysis is not sensitive to the Final State gluon Radiation (FSR). Considering a top quark produced by a virtual gluon, if it is on its "mass shell" it cannot radiate anything (gluon or photon), otherwise energy-momentum conservation would be violated at the radiation emission vertex. If the quark is off its mass shell, then it will radiate –most likely a gluon, but could be also a photon since the top quark is charged– and the radiation will bring it back on its mass shell. In both cases the top quark, at the time of its decay, will be on its mass shell and therefore its decay products will receive the same amount of boost due the mother particle's (top) mass. Therefore, either radiation from the top quark is included or not, the correlation of any lepton kinematic quantity (e.g. the slope of $P_T$) with respect to the top mass must be the same.

The PDF - parton distribution function - models the distribution of partons inside the high momentum protons. The default Monte Carlo sample has been generated with the CTEQ5L PDF set [59]. To estimate the systematic uncertainty on the top mass because of the choice of the PDF, two more sets are used: a) MRST72 [60] that is a MRST set that uses the same $\alpha_S$ value with the CTEQ5L and b) MRST75 that is a MRST set that uses a different $\alpha_S$ value with the CTEQ5L. All samples have been generated for a top mass of $M_{top} = 175$ GeV/c$^2$.

As described above the systematic uncertainties are estimated using two different approaches. For the LH method, the leptons' $P_T$ distributions corresponding to the different systematics are fit with the Gamma x Fermi function. The shape parameters used are listed in Table 6.1 and the top mass is estimated using the likelihood minimization procedure. This mass is compared to the nominal Pythia mass that has

been estimated the same way (see Figure 8.2) and the difference gives the measure of the uncertainty. Table 8.2 summarizes the uncertainty on the top mass due to the different sources.

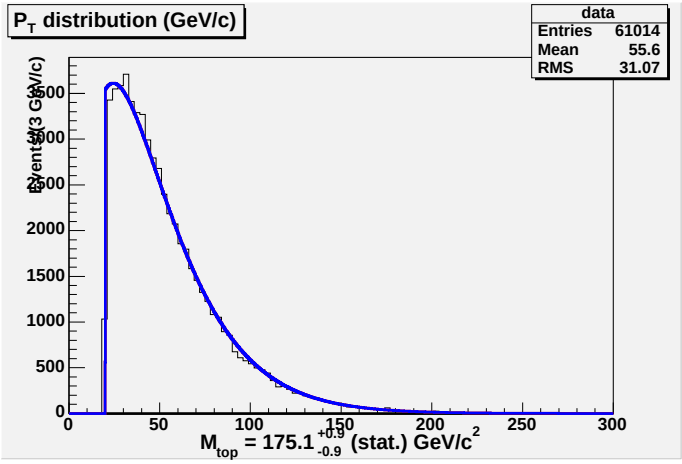


Figure 8.2: Fit to the Pythia $P_T$ distribution of $M_{top} = 175$ GeV/$c^2$ template. The LH minimization procedure gives a mass of 175±0.9 GeV/$c^2$

| source | $\delta M_{top}^{sig}$ (GeV) |
|---|---|
| ISR | 1.26 ± 1.41 |
| PDF | 0.650 ± 1.38 |
| Generator | 2.05 ± 1.48 |
| Total | 2.84 ± 2.50 |

Table 8.2: List of signal related systematic errors on the top mass according to the LH method. The error on the uncertainties comes from the statistics of the samples that were used for the estimation. The nominal top mass of 175 GeV/$c^2$ is considered.

For the SL method, in first approach, the difference of the leptons' $P_T$ due to a reason that may cause a systematic uncertainty is estimated. Then the total uncertainty on the mean $P_T$ is propagated to evaluate the corresponding uncertainty on the top mass. It is taken into account that the sensitivity of the $P_T$ to the top mass is $\lambda = 0.135$. Table 8.3 summarizes the uncertainty on the mean $P_T$ due to the different

sources:

| source | $\delta\langle P_T\rangle_{sig}$ (GeV) |
|---|---|
| ISR | $0.210 \pm 0.135$ |
| PDF | $0.130 \pm 0.135$ |
| Generator | $0.345 \pm 0.135$ |
| Total | $0.424 \pm 0.234$ |

Table 8.3: List of signal related systematic errors on the mean $P_T$ according to the SL method. The error on the uncertainties comes from the statistics of the samples that were used for the estimation. The nominal top mass of 175 GeV/$c^2$ is considered.

Using the Equation 8.2 we estimate that the signal related error on the $M_{top}$ with the SL method is:

$$\left(\delta M_{top}^{sig}\right)_{syst} = \frac{\delta\langle P_T\rangle_{sig}}{\lambda} = 3.1 \pm 1.7 \text{ GeV/c}^2 \tag{8.3}$$

fully consistent with the value obtained by the LH method.

## 8.2 Background related systematic uncertainties

This section summarizes the systematic uncertainties related to the scale and the shape of the background.

### 8.2.1 Background scale systematic uncertainty

From Tables 5.1 and 5.2 it is clearly seen that the background scale uncertainty is not, most probably, more than 10%. To be very conservative, an uncertainty of 20% is considered. To estimate the background scale uncertainty for the LH method, random samples of signal and background events corresponding to 1.8 $fb^{-1}$ of luminosity are used. The signal events were generated for top masses of 152, 175 and

200 GeV/c$^2$. The number of background events $n_{bg}$ are increased/decreased by this amount keeping the total number of events constant and the top mass is reestimated using the likelihood minimization procedure. Table 8.4 shows the estimated top mass and the number of signal and background events for each case. For top input mass of 175 GeV/c$^2$ the fitted mass deviates by about 800 MeV/c$^2$. For top input mass of 152 GeV/c$^2$ the deviation is about 200 MeV/c$^2$ and for the 200 GeV/c$^2$ it increases to about 2-3 GeV/c$^2$. Therefore the measurement is considered insensitive to the background scale. This conclusion is consistent with a similar result described in the Lepton + Jets analysis [9].

| Background expectation | $n_{s1}$ | $n_{bg1}$ | $n_{s2}$ | $n_{bg2}$ | $M_{top}$(GeV/c$^2$) |
|---|---|---|---|---|---|
| 20% high | 159.7 | 91.34 | 158±22 | 92.5 ±16 | 151.4 ± 19.4 |
| Default ($M_{top}$=152 GeV) | 174.94 | 76.12 | 171±20 | 79 ±14 | 151.2 ± 18.1 |
| 20% low | 190.19 | 60.90 | 185±19 | 64 ±11 | 151.1 ± 17.0 |
| 20% high | 159.7 | 91.34 | 158±22 | 93 ±17 | 175.32 ± 24 |
| Default ($M_{top}$=175 GeV) | 174.94 | 76.12 | 171±21 | 79 ±14 | 174.52 ± 22.0 |
| 20% low | 190.19 | 60.90 | 186±19 | 64 ±11 | 173.8 ± 20.0 |
| 20% high | 159.7 | 91.34 | 136±21 | 109 ±12 | 197.4 ± 31.3 |
| Default ($M_{top}$=190 GeV) | 174.94 | 76.12 | 153 ±20 | 92 ±13 | 194.2 ± 28 |
| 20% low | 190.19 | 60.90 | 170±25 | 74 ±11 | 191.5 ± 24.6 |

Table 8.4: The number of background events is increased/decreased by 20%. The starting number of signal and background leptons $n_{s1}$, $n_{bg1}$ and similarly the number of leptons $n_{s2}$, $n_{bg2}$ estimated by the fit. The $M_{top}$ is estimated by the likelihood minimization procedure. The quoted errors are statistical.

Using the SL method, the uncertainty because of the background scale is estimated from the third term of Equation 8.2

$$\left(\delta M_{top}^{bg,scale}\right)_{syst} = \frac{1}{\lambda} \times (1-\rho)\left(\langle P_T\rangle_{sig} - \langle P_T\rangle_{bg}\right)\left(\frac{\delta n_{bg}}{n_{bg}}\right) \tag{8.4}$$

Taking into account that the sensitivity of the mean $P_T$ of the signal+backgound

distributions to the top mass is $\lambda$=0.094 and that for the luminosity of 1.8 fb$^{-1}$ we expect $n_{bg} = 38.06 \pm 7.44$ events, the background scale uncertainty is estimated to be

$$\left(\delta M_{top}^{bg,scale}\right)_{syst} = 0.8 \pm 1.2 \text{ GeV/c}^2 \tag{8.5}$$

### 8.2.2 Background shape systematic uncertainty

The good agreement between the SM estimate and the data in the control 1-jet bin (dominated by background), as quantified by the high value given by the relevant KS test (Figure 5.8), gives us confidence that our, both background shape and scale estimates, are pretty reliable.

However, due to the complexity of the dilepton background it is important to evaluate the systematic uncertainty associated with the ambiguity of the background $P_T$ shape. The diboson and the $Z \rightarrow \tau^+\tau^-$ background $P_T$ shapes are derived directly from the Monte Carlo samples and are considered to be known accurately. Considering also that they represent less than 40% of the total background they are expected to have but a minor contribution to the uncertainty of the total background shape.

The fakes background is derived from the data and it is therefore considered that the $P_T$ shape is pretty accurate. On the other hand the fake lepton expectation has a systematic component coming from a $\pm$30% fake rate uncertainty [48]. The fakes expectation is increased/decreased by this amount and the total background is recalculated. For the LH method the new histograms are fitted with the GammaxFermi function and the new shape parameters that fit best the spectra are estimated. The function is integrated using Equation 8.6 to estimate the mean $P_T$ that corresponds

to the fitted curve.

$$< P_T >= \int_0^\infty P_s\,(P_T)\,\frac{P_T}{q} dP_T = q\left[1 + p + \left(\frac{c}{q}\right)\frac{e^{-c/q}}{\Gamma(1+p, c/q)}\right] \qquad (8.6)$$

Table 8.5 summarizes the mean $P_T$ of the combined background and from the fit for the three cases. The mean $P_T$ from the histogram and from the fit differ less than 20 MeV, a fact that once more makes us confident that the GammaxFermi parametrization works very well. Table 8.6 shows the fitted parameter values for the nominal case and for the cases that the fake expectation is increased/decreased by 30%. Figures 8.3 (a) and (b) show the $P_T$ spectra for the total background when the fake background expectation is increased and reduced by 30% respectively.

| Fake expectation | Bg $P_T$ (GeV) | $P_T^{fit}$(GeV) | $\delta\langle P_T\rangle_{bg,shape}$(GeV) |
|---|---|---|---|
| 30% high | 53.71 ±1.8 | 53.69 | -0.54±1.9 |
| Default | 54.25 ±1.9 | 54.24 | - |
| 30% low | 54.93 ±2.0 | 54.92 | +0.68±2.0 |

Table 8.5: Fake background $\langle P_T\rangle$ values and their differences from the default value for the 30% high and low cases.

| Fake expectation | p | q |
|---|---|---|
| 30% high | -0.612015 | 48.1097 |
| Default | -0.583288 | 48.0771 |
| 30% low | -0.546375 | 47.9822 |

Table 8.6: p and q parameters for the default, 30% high and 30% low fake background.

For the LH method, in order to estimate the systematic uncertainty because of the ambiguity in the shape of the fakes, a random sample of 251 signal (for $M_{top}$ = 175GeV) and background $P_T$ values is selected and the mass that they correspond is estimated using the likelihood method. The fitting parameters are changed as defined in Table 8.6 and the systematic uncertainty is taken as the difference between the

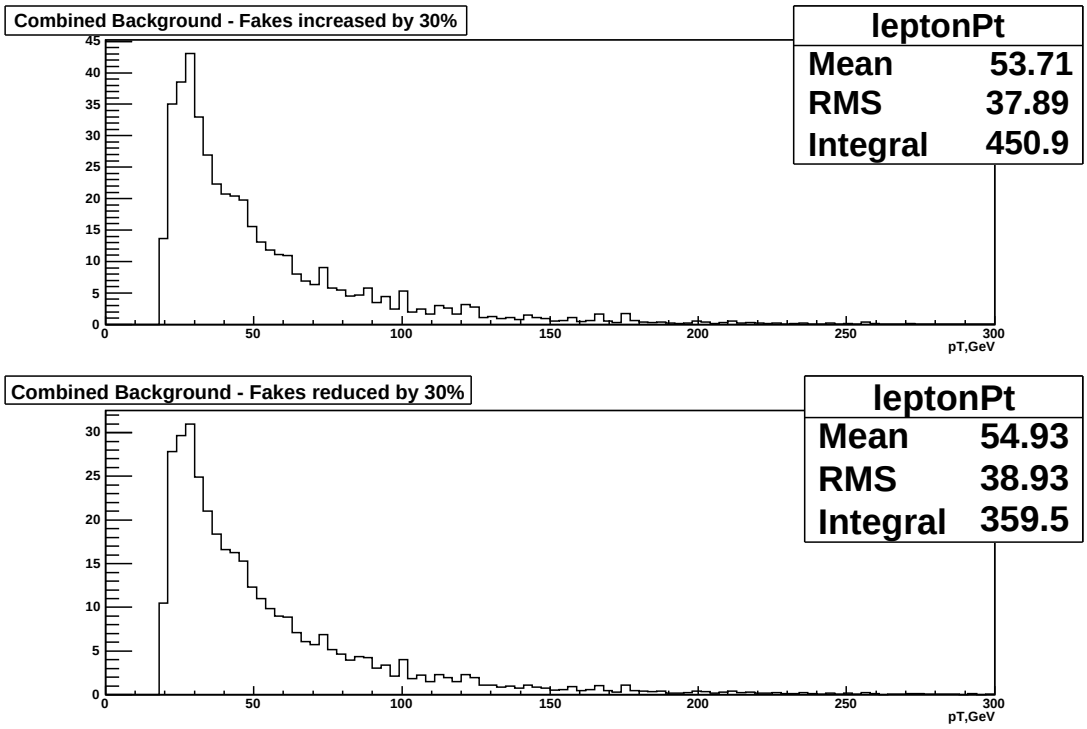


Figure 8.3: Combined background $P_T$ distribution when fakes expectation is (a) increased and (b) reduced by 30%.

nominal mass estimation and the altered estimation. The mass estimations are shown in Table 8.7.

| Fake expectation | Top Mass with LH (GeV) | Deviation (GeV) |
|---|---|---|
| 30% high | 176.25±22 | +1.73 |
| Default | 174.52±22 | - |
| 30% low | 172.49±22 | -2.03 |

Table 8.7: LH estimation of the top mass systematic uncertainty because of the ambiguity of the fakes shape. A sample of signal and background leptons, corresponding to 1.8 $fb^{-1}$, was used. The shape of the background was estimated using the parameters listed in Table 8.6.

For the SL method it is considered that the background contribution to the total SM expectation is 30% ($1 - \rho$=0.3) and that the sensitivity of the mean $P_T$ to the top mass is 9.4% (slope $\lambda = 0.094$). The background shape uncertainty because of

the fakes is estimated using Equation 8.7:

$$\left(\delta \mathrm{M}_{\mathrm{top}}^{\mathrm{bg,shape}}\right)_{\mathrm{syst}} = (1-\rho)\frac{\delta\langle \mathrm{P_T}\rangle_{\mathrm{bg,shape}}}{\lambda} \tag{8.7}$$

The propagated error to the top mass is -1.72 and +2.17 when increasing/decreasing by 30% the fakes expectation.

The DY background shape is the most complicated as DY events generated for $\mathrm{M_{ll}}$ in the range of [20-600] GeV are used to form the $\mathrm{P_T}$ distribution. The low, Zpeak and high $\mathrm{M_{ll}}$ samples are combined taking into consideration the different cross-sections and finally the different flavor contributions (ee, $\mu\mu$ and e$\mu$), according to the expectations derived from Table 5.1. The number of DY events is known with an accuracy of 23.5% [48]. Following the same procedure as for the fakes, the DY expectation is increased/decreased by 25% and the total background is recalculated. The new spectra are fit with the Gamma×Fermi function and the fitted mean $\mathrm{P_T}$ is estimated using Equation 8.6. Figures 8.4 (a) and (b) show the $\mathrm{P_T}$ spectra for the total background when the DY background expectation is increased and reduced by 25% respectively.

Table 8.8 summarizes the mean $\mathrm{P_T}$ of combined background distribution and the one from the fit, for the three cases. The mean $\mathrm{P_T}$ from the histogram and from the fit differ less than 20 MeV. Table 8.9 shows the fitted parameter values for the nominal case and for the cases that we increase/decrease the DY expectation by ±25%.

For the LH method, in order to estimate the systematic uncertainty because of the ambiguity in the shape of the DY a random sample of 251 signal (for $\mathrm{M_{top}}$ = 175 GeV/$\mathrm{c^2}$) and background $\mathrm{P_T}$ values are selected and the mass that they correspond is estimated using the likelihood method. The fitting parameters are changed

| DY expectation | $P_T$ (GeV) | $P_T^{fit}$(GeV) | $\delta\langle P_T\rangle_{bg,shape}$(GeV) |
|---|---|---|---|
| 25% high | 55.07 ±1.9 | 55.10 | +0.82±1.9 |
| Default | 54.25 ±1.9 | 54.24 | - |
| 25% low | 53.31 ±1.9 | 53.29 | -0.94±1.9 |

Table 8.8: DY background $\langle P_T\rangle$ values and their differences from the default value for the 25% high and low cases.

| DY expectation | p | q |
|---|---|---|
| 25% high | -0.584264 | 49.4383 |
| Default | -0.583288 | 48.0771 |
| 25% low | -0.57623 | 46.436 |

Table 8.9: p and q parameters for the default, 25% high and 25% low DY background.

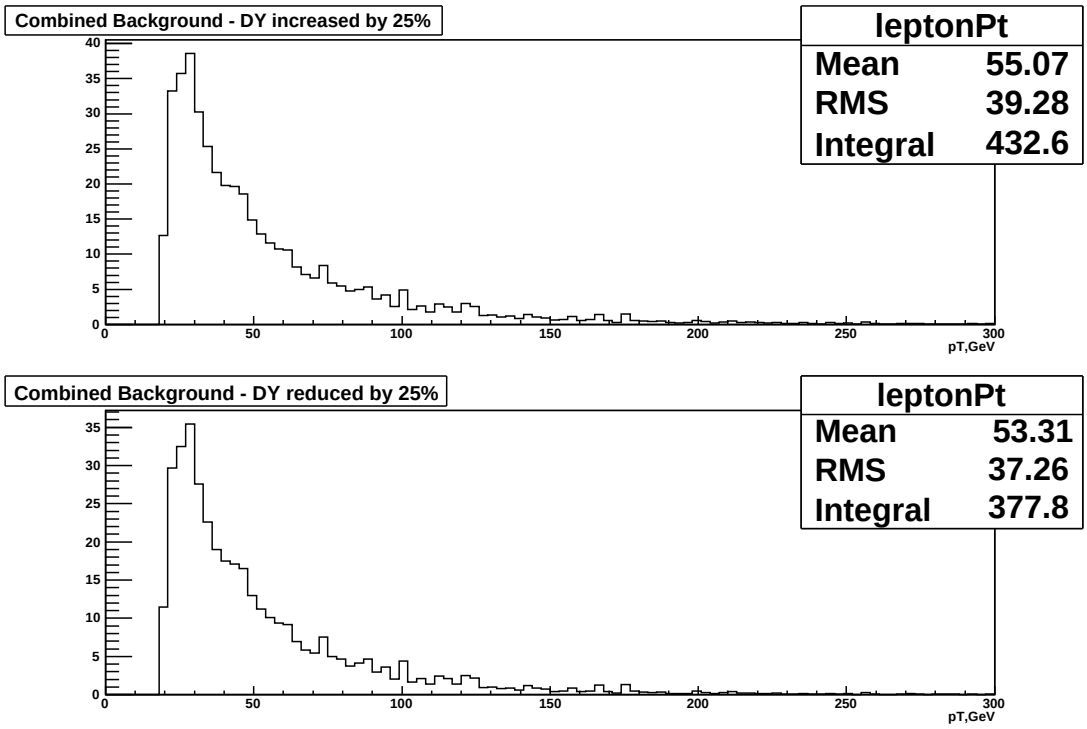


Figure 8.4: Combined background $P_T$ distribution when DY expectation is (a) increased and (b) reduced by 25%.

as defined in Table 8.9 and the systematic uncertainty is taken as the difference between the nominal mass estimation and the altered estimation. The mass estimations

are found in Table 8.10.

| DY expectation | Top Mass with LH (GeV) | Deviation (GeV) |
|---|---|---|
| 25% high | 172.22±22 | -2.3 |
| Default | 174.52±22 | - |
| 30% low | 177.24±22 | +2.72 |

Table 8.10: LH estimation of the top mass systematic uncertainty because of the ambiguity of the DY shape. A sample of signal and background leptons, corresponding to 1.8fb$^{-1}$, was used. The shape of the background was estimated using the parameters listed in Table 8.9.

For the SL method the propagated error to the top mass is +2.62 and -3 when increasing/decreasing by 25% the DY expectation. The total systematic error uncertainty is 3.4 GeV/c$^2$.

## 8.3 Leptons' $P_T$ scale uncertainty

In this section the uncertainty on the top mass due to the leptons' $P_T$ scale uncertainty [61] is evaluated. The idea behind this method is to calibrate the lepton transverse momentum ($E_T$ for electrons & $P_T$ for muons) against the mass of the Z boson, knowing that the Z mass is currently known from LEP measurements with ±2 MeV accuracy. This is justified as the $P_T$ spectra of leptons from Z boson decays have a large overlapping with these of leptons from top decays as shown in Figure 8.5.

Data and Monte Carlo $Z \rightarrow e^+e^-$ and $Z \rightarrow \mu^+\mu^-$ events with an invariant mass in the $60 \leq M_{inv} \leq 120$ GeV/c$^2$ window are selected. The invariant mass of the dilepton events is reconstructed using the information from the transverse momentum $P_{T1,2}$, the pseudorapidity $\eta_{1,2}$ and the azimuthal angle $\phi_{1,2}$ of each lepton, according to

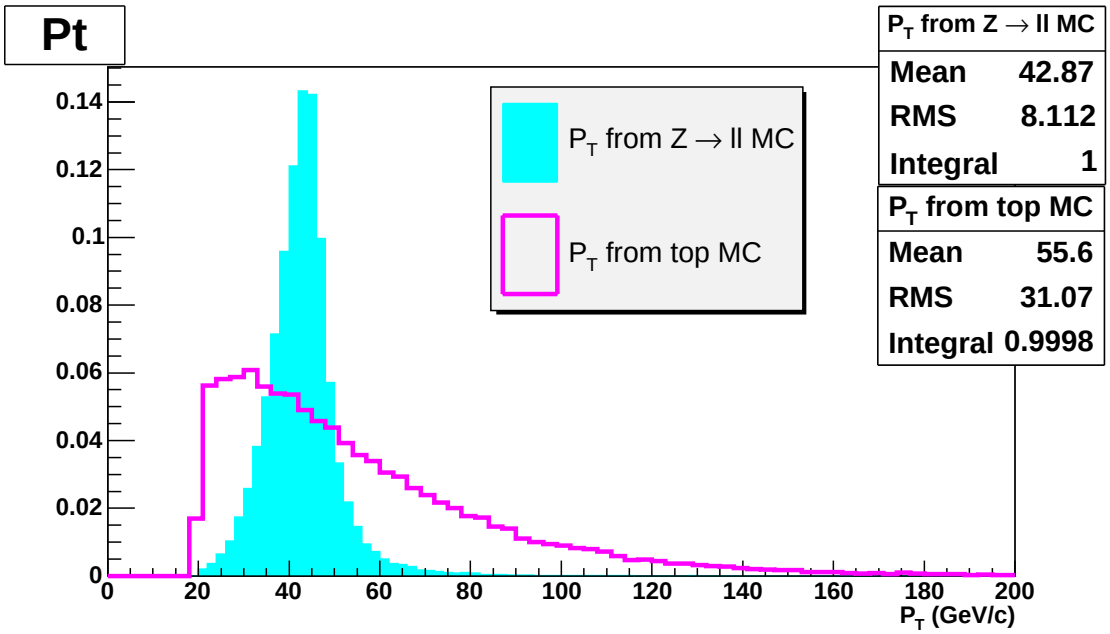


Figure 8.5: Lepton $P_T$ spectra from Z boson decays (aqua histogram) and top dilepton decays (pink histogram). A large overlap is observed.

Equation 8.8. The spectra for the electrons and the muons are fit to find the centroid $M_Z$ of the distributions, taking into account the background mainly in the low and high tails.

$$M_Z = \sqrt{2 \times \ P_{T1} \times \ P_{T2} \times \ [\cosh(\eta_1 - \eta_2) - \cos(\phi_1 - \phi_2)]} \tag{8.8}$$

The invariant mass of the $Z \rightarrow e^+e^-$ and the $Z \rightarrow \mu^+\mu^-$ data and MC events is reconstructed using only the leptons' $P_T$, eta and phi angle variables.

For this, the invariant mass spectra are fit with the following function:

$$F(M) = Ae^{-BM}\left\{\exp\left[-\frac{1}{2}\left(\frac{M - M_Z}{\Delta}\right)^2\right] + \frac{(\Gamma/2)^2}{(M - M_Z)^2 + (\Gamma/2)^2}\right\} \tag{8.9}$$

The choice of Equation 8.9, having 5 free parameters ($M_Z$, A, B, $\Gamma$, $\Delta$) is based on the following arguments:

- The Lorenzian function is necessary to describe the tails of the mass peak. It is driven by the Z resonance.

- The Gaussian function is necessary to describe the width of the mass peak: It appears too broad, with respect to its tails, to be only Lorenzian. The width of the Gaussian function is driven by the resolution in $P_T$ (for $\mu\mu$ events) and $E_T$ (for ee events).

- The exponential amplitude function is necessary to describe the observed damping of the high mass tail relative to the low mass tail. It is inspired by the exponential fall-off of the continuum Drell-Yan ($q\overline{q} \rightarrow \gamma* \rightarrow l^+l^-$) cross section with the invariant mass.

Figures 8.6, 8.7, 8.8 and 8.9 illustrate the results of the fits which are summarized in Table 8.11. The widths of the combined Gaussian+Lorenzian peaks listed in Table 8.11 are evaluated using the approximation:

$$\mathrm{FWHM} \approx \sqrt{\mathrm{FWHM_{Gauss}} \times \mathrm{FWHM_{Lorentz}}} \tag{8.10}$$

which is obviously exact for $\mathrm{FWHM_{Gauss}} = \mathrm{FWHM_{Lorentz}}$

| **Sample** | **Centroid** (GeV) | **Width** (GeV) | **Deviation** from $M_Z$ LEP=91.19GeV (MeV) |
|---|---|---|---|
| $\mathbf{Z \rightarrow e^+e^-}$**data** | 90.93±0.02 | 6.58±0.05 | 260±20 |
| $\mathbf{Z \rightarrow e^+e^-}$**MC** | 91.51±0.02 | 6.40±0.05 | -320±20 |
| $\mathbf{Z \rightarrow \mu^+\mu^-}$ **data** | 91.02±0.02 | 5.38±0.55 | 160±20 |
| $\mathbf{Z \rightarrow \mu^+\mu^-}$ **MC** | 91.15±0.02 | 5.02±0.04 | 40±20 |

Table 8.11: Results to the fits of the $Z \rightarrow l^+l^-$ data and MC.

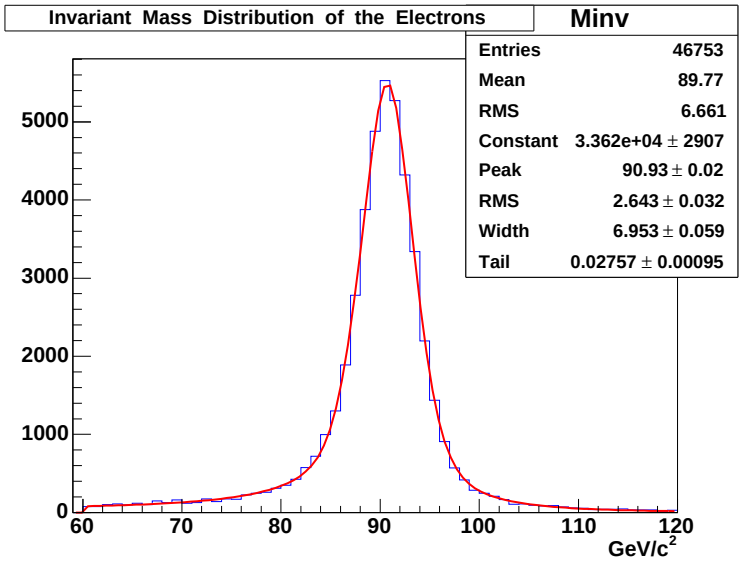


Figure 8.6: Fit of the model function to the $Z \rightarrow e^+e^-$ data.

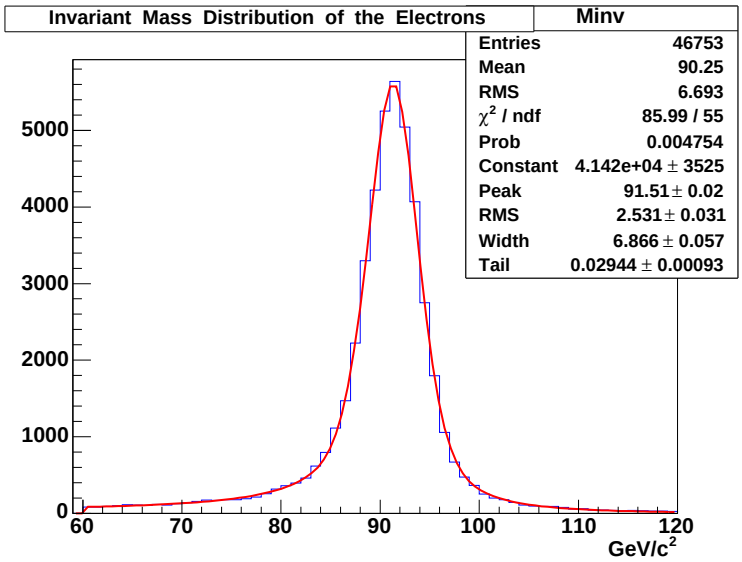


Figure 8.7: Fit of the model function to the $Z \rightarrow e^+e^-$ MC.

Assuming that the uncertainty on the Z invariant mass is due to the only uncertainty on the $P_T$ it is approximated that:

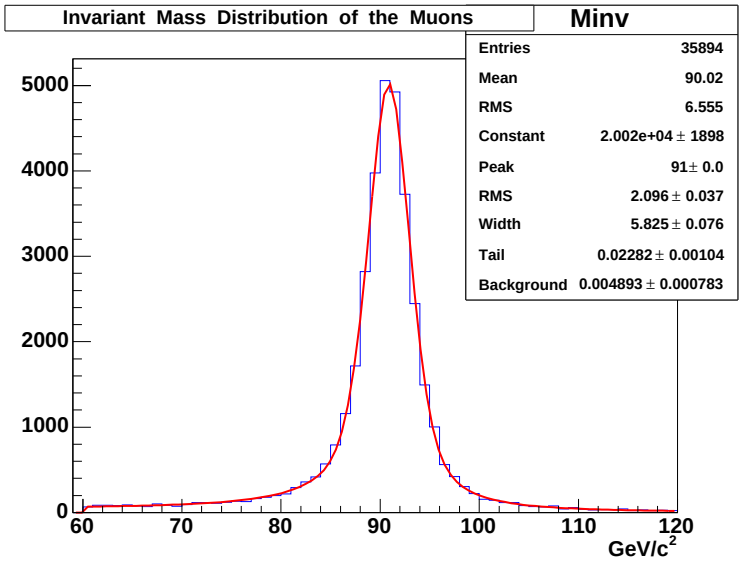


Figure 8.8: Fit of the model function to the Z $\rightarrow \mu^+\mu^-$ data.

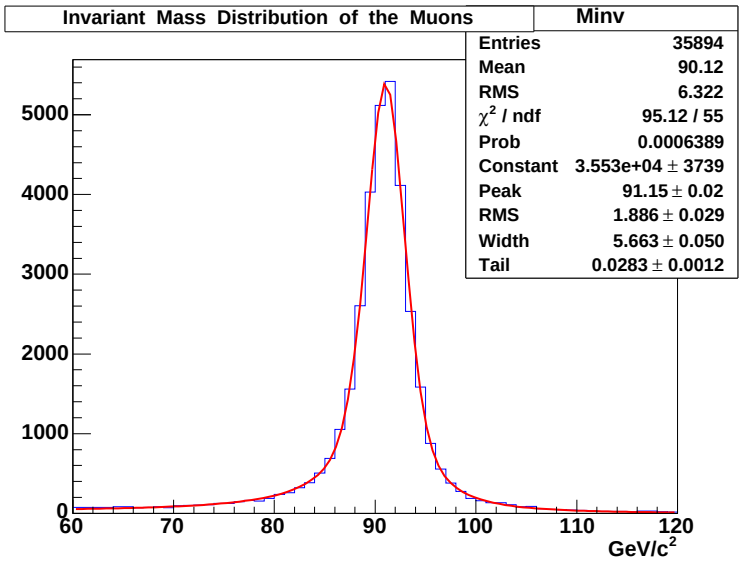


Figure 8.9: Fit of the model function to the Z $\rightarrow \mu^+\mu^-$ MC.

$$\frac{\Delta P_{T,Z}}{P_{T,Z}} = \frac{\Delta M_Z}{M_Z} \tag{8.11}$$

It is considered that there is no physical reason for the relative uncertainty on the $P_T$ measurement of the leptons coming from Z decays to be any different from the relative uncertainty of the $P_T$ measurement of the leptons coming from other processes. Therefore, taking into account that the mean $P_T$ of the $t\bar{t} \rightarrow$ dilepton signal distribution for $M_{top}$=175 GeV is 55.6±0.13GeV and for the combined background is 54.25±1.9 GeV we propagate the uncertainty on the Z mass from Z→dilepton decays to evaluate the corresponding uncertainty on the mean $P_T$ of the $t\bar{t} \rightarrow$ dilepton and background decays according to the following Equations:

$$\frac{\Delta P_T^{sig}}{P_T^{sig}} = \frac{M_Z^{LEP} - M_{FIT}}{M_Z^{LEP}} \tag{8.12}$$

$$\frac{\Delta P_T^{bg}}{P_T^{bg}} = \frac{M_Z^{LEP} - M_{FIT}}{M_Z^{LEP}} \tag{8.13}$$

Table 8.12 shows the deviations on the Z mass, estimated as described above. The Table also lists the uncertainties on the mean $P_T$ measurement for the top signal and for the background, estimated from Equations 8.12 and 8.13 respectively. The numbers refer to electrons and muons for data and MC.

| **Sample** | **Zmass deviation (MeV)** | $\Delta P_T^{sig}$ **(MeV)** | $\Delta P_T^{bg}$ **(MeV)** |
|---|---|---|---|
| $\mathbf{Z \rightarrow e^+e^-}$**data** | 260±20 | 158.5±12.2 | 154.7±13.0 |
| $\mathbf{Z \rightarrow e^+e^-}$**MC** | -320±20 | -195.1±12.2 | -190.4±13.7 |
| $\mathbf{Z \rightarrow \mu^+\mu^-}$ **data** | 160±20 | 97.5±12.2 | 95.2±12.4 |
| $\mathbf{Z \rightarrow \mu^+\mu^-}$ **MC** | 40±20 | 24.4±12.2 | 23.79±12.0 |

Table 8.12: Uncertainty on the $P_T$ measurement for the top signal and the top background for electros and muons. Data and MC uncertainties are treated separately.

In the signal distributions 48.7% of the leptons are electrons and 51.3% are muons. The corresponding numbers for the total background are 44.7% for the electrons and

55.3% for the background.

Therefore the total uncertainty on the $P_T$ measurement for the signal and the background, as estimated from the data is:

$$\left(\Delta P_T^{sig}\right)_{data} = 0.487 \times 158.5 + 0.513 \times 97.5 = 127.2 \pm 8.6 \text{ MeV} \tag{8.14}$$

$$\left(\Delta P_T^{bg}\right)_{data} = 0.447 \times 154.7 + 0.553 \times 95.2 = 115.8 \pm 9.0 \text{ MeV} \tag{8.15}$$

The total uncertainty on the $P_T$ measurement for the signal and the background, as estimated from MC is:

$$(\Delta P_T^{sg})_{mc} = 0.487 \times (-195.1) + 0.513 \times 24.4 = -82.5 \pm 8.6 \text{ MeV} \tag{8.16}$$

$$\left(\Delta P_T^{bg}\right)_{mc} = 0.447 \times (-190.3) + 0.553 \times 23.79 = -98.2 \pm 9.0 \text{ MeV} \tag{8.17}$$

The final error on the top mass because of the leptons $P_T$ scale uncertainty is derived from Equation 8.18. The estimates for the slope $\lambda = 0.094$ and the purity $\rho = 0.70$ are taken into account.

$$\left(\delta M_{top}^{\langle P_T \rangle}\right)_{syst} = \frac{1}{\lambda} \times \sqrt{\rho^2 (\delta \langle P_T \rangle_{sig})^2 + (1-\rho)^2 (\delta \langle P_T \rangle_{bg})^2} \tag{8.18}$$

Therefore the uncertainty on the top mass from the data and the MC is estimated to be:

$$\left(\delta M_{top}^{\langle P_T \rangle}\right)_{data} = 1017 \pm 150 \text{ MeV/c}^2 \tag{8.19}$$

$$\left(\delta M_{top}^{\langle P_T \rangle}\right)_{mc} = 690 \pm 120 \text{ MeV/c}^2 \tag{8.20}$$

As the uncertainties on the top mass from data and MC are not correlated they are linearly added to get the final error:

$$\left(\delta M_{top}^{\langle P_T \rangle}\right)_{syst} = 1.7 \pm 0.2 \text{ GeV/c}^2 \tag{8.21}$$

## 8.4 Final systematic uncertainty to the top mass

To estimate the total systematic uncertainty to the top mass the partial errors are added in quadrature. Table 8.13 summarizes the uncertainties for the LH and SL methods.

| Source of systematic | error-LH (GeV) | error-SL (GeV) |
|---|---|---|
| Signal | 2.84±2.5 | 3.1±1.7 |
| Background scale | 0.2±0.0 | 0.8±1.2 |
| Background shape | 3.2±0.0 | 3.4±0.0 |
| lepton $P_T$ scale | 1.7±0.2 | 1.7±0.2 |
| Total | 4.6±2.5 | 5.0±2.1 |

Table 8.13: Partial and total systematic errors for the two methods.

# Chapter 9

## Results

### 9.1 Top mass result in the dilepton channel

The dilepton selection on the 1.8 $fb^{-1}$ data gives 125 dilepton events. The 250 leptons of this dataset have a mean $P_T$=52.96±1.97 GeV/c. Figure 9.1 illustrates the mean $P_T$ of the data in comparison with the Standard Model signal+background expectation. The Kolmogorov-Smirnov test, which gives 0.95, verifies that there is a good agreement.

Table 9.1 presents the results of the fit to the 1.8 $fb^{-1}$ data using the Likelihood Method (LH). Figure 9.2 illustrates the fit to the data (blue line). The red line is the fit to the signal and the black line the fit to the background.

| Background expectation | $n_{s1}$ (leptons) | $n_{bg1}$ (leptons) | $n_{s2}$ (leptons) | $n_{bg2}$ (leptons) | $M_{top}$ (GeV/$c^2$) |
|---|---|---|---|---|---|
| Default | 174.94 | 76.12 | 171±21 | 78 ±14 | 156 $^{+22}_{-19}$ |

Table 9.1: The standard model expectations for the top signal and background leptons are denoted with $n_{s1}$, $n_{bg1}$ and the number of leptons estimated by the fit with $n_{s2}$, $n_{bg2}$ respectively. The $M_{top}$ is estimated by the likelihood minimization procedure. The quoted errors are statistical.

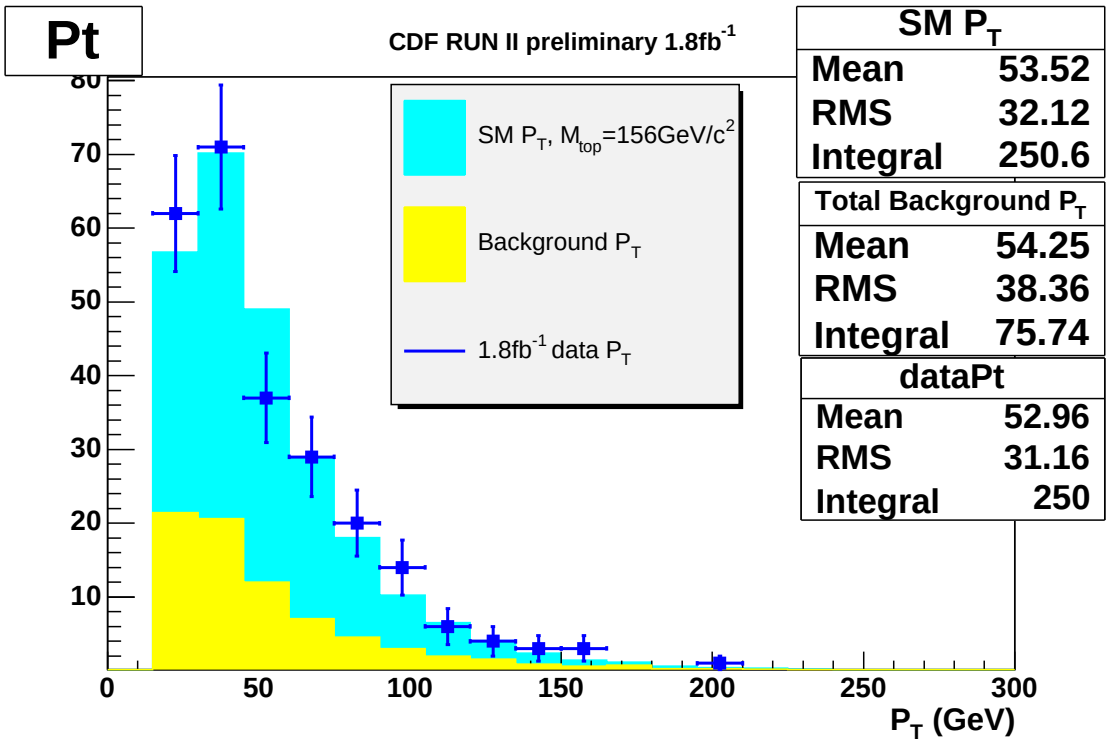


Figure 9.1: $P_T$ distributions of: leptons in the dilepton data (blue points), signal & background SM estimate (aqua histogram) and total background (yellow histogram). The expected top signal is for a top mass of 156 GeV/$c^2$

The LH method gives $M_{top} = 156^{+22}_{-19(stat)} \pm 4.6_{(syst)}$ GeV/$c^2$.

Using the standard Equation 6.2, the Straight Line method estimates that $M_{top}$=$149 \pm 21_{(stat)} \pm 5_{(syst)}$ GeV/$c^2$.

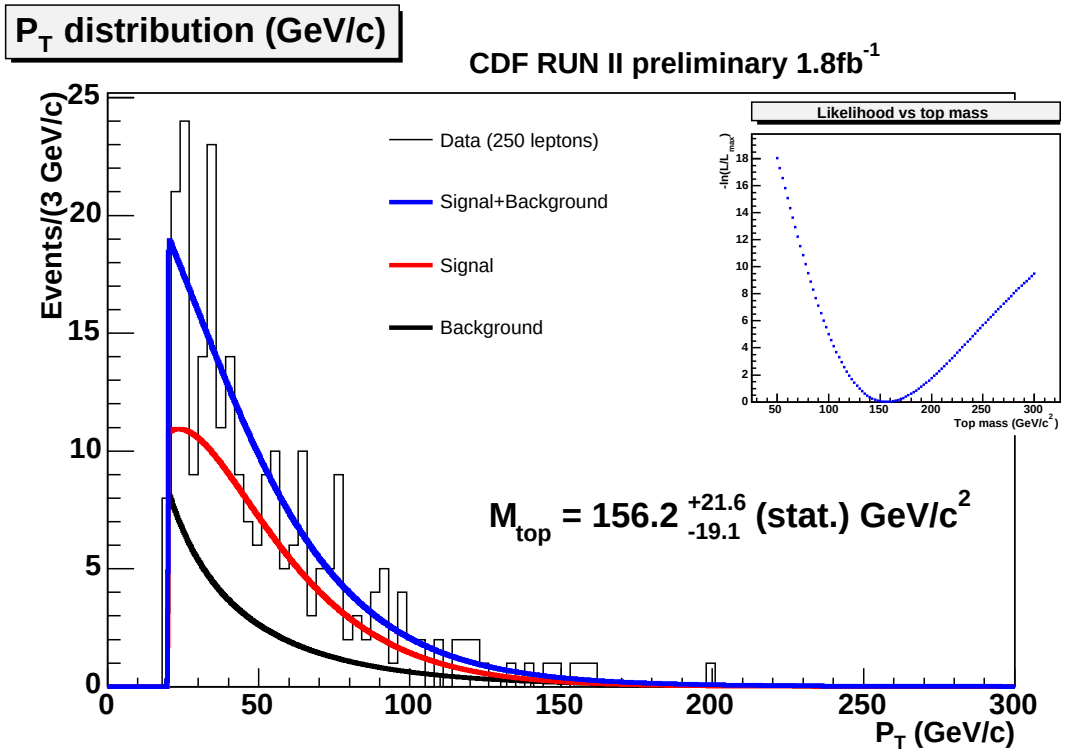


Figure 9.2: Fit to the 1.8 fb$^{-1}$ data

## 9.2 Top mass results from the different dilepton flavors

Additionally, the top mass for ee, $\mu\mu$ and e$\mu$ events was estimated separately. Figures 9.3, 9.4 and 9.5 illustrate the mean $P_T$ of the data in comparison with the Standard Model signal+background expectation for the three cases. The top mass estimates corresponding to the different dilepton flavor datasets are listed in Table 9.2. The LH fits are shown in Figures 9.6, 9.7 and 9.8. Combining the three results we get a top mass of 151.4 $\pm$ 18.8 GeV/$c^2$, i.e consistent with the top mass estimated from the full sample.

| dilepton type | ee | $\mu\mu$ | e$\mu$ |
|---|---|---|---|
| Mass (GeV) | 144.5$\pm$41 | 189.7$\pm$55 | 146.9 $\pm$23 |

Table 9.2: Top mass with the LH for the ee, $\mu\mu$ and e$\mu$ events

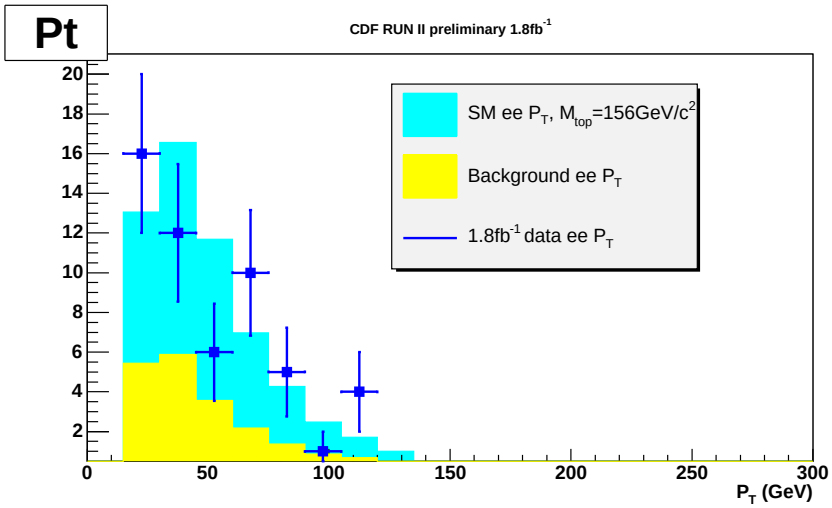


Figure 9.3: $P_T$ distributions of: leptons in the ee dilepton data (blue points), signal & background SM estimate (aqua histogram) and total background (yellow histogram). The expected top signal is for a top mass of 156 GeV/$c^2$

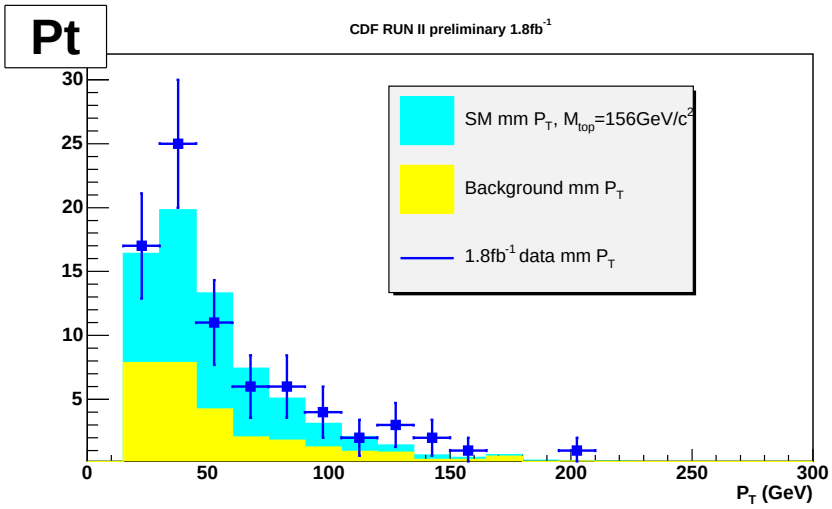


Figure 9.4: $P_T$ distributions of: leptons in the $\mu\mu$ dilepton data (blue points), signal & background SM estimate (aqua histogram) and total background (yellow histogram). The expected top signal is for a top mass of 156 GeV/$c^2$

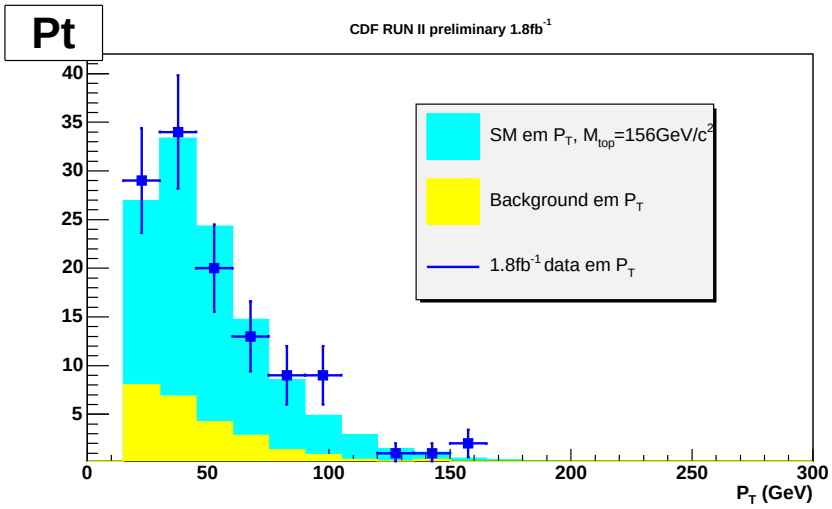


Figure 9.5: $P_T$ distributions of: leptons in the e$\mu$ dilepton data (blue points), signal & background SM estimate (aqua histogram) and total background (yellow histogram). The expected top signal is for a top mass of 156 GeV/$c^2$

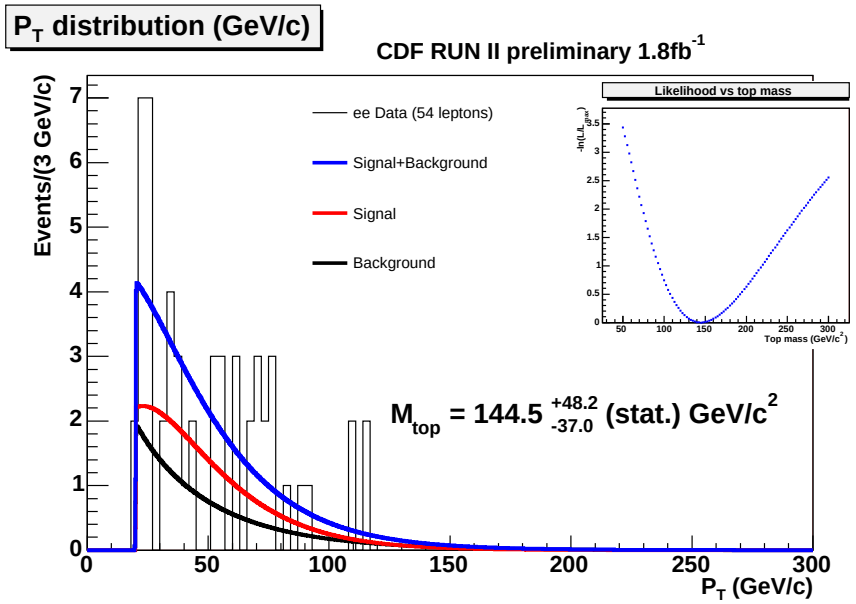


Figure 9.6: Fit to the 1.8 fb$^{-1}$ ee data events.

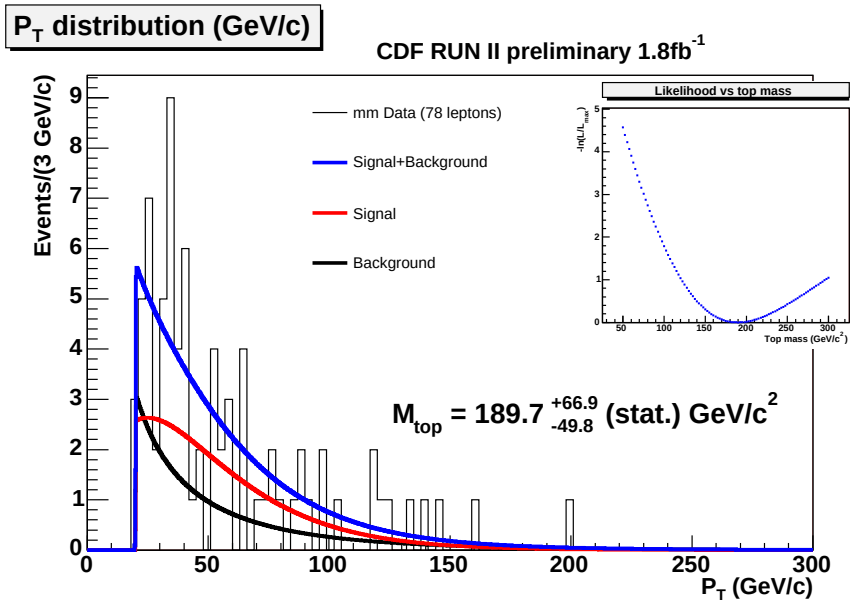


Figure 9.7: Fit to the 1.8 fb$^{-1}$ $\mu\mu$ data events.

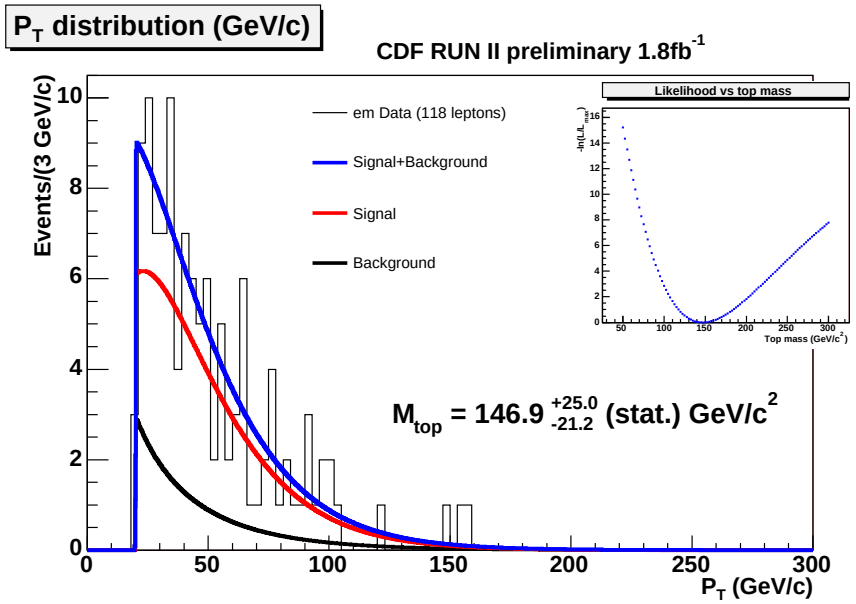


Figure 9.8: Fit to the 1.8 fb$^{-1}$ e$\mu$ data events

## 9.3 Combined top mass from the dilepton and lepton+jets channels

A measurement of the top quark mass using the leptons' $P_T$ information has also been successfully used in the lepton+jets channel for an integrated luminosity corresponding to 340 $pb^{-1}$ [9]. This analysis was very thoroughly established and was approved by the CDF experiment. As it has already been explained at the beginning of this dissertation, one of the most important reasons that the leptons' $P_T$ was selected for the measurement of the top quark mass is that it is a common variable both the dilepton and the lepton+jets channels. This gives the opportunity to combine and compare the results.

In the dilepton channel, as it has been shown, the method provides two independent and mutually compatible results for the LH and the SL implementations. In the lepton+jets channels the two implementations have also been successfully applied, but the SL result is considered as the main one as the LH method carries a large and asymmetric statistical uncertainty. To get a combined top mass result from the two channels two combinations are considered: (a) the dilepton LH & lepton+jets SL and (b) the dilepton SL & lepton+jets SL [62]. It is noted that the lepton+jets SL top mass result is:

$$M_{top}^{l+jets} = 220 \pm 47.4_{stat} \pm 9.4_{syst} \text{ Gev/c}^2 \tag{9.1}$$

and it is reminded that the dilepton LH and SL top mass results are respectively:

$$\mathrm{M}_{\mathrm{top}}^{\mathrm{DIL}} = 156 \pm 20_{\mathrm{stat}} \pm 4.6_{\mathrm{syst}}\ \mathrm{Gev/c^2}\ -\ \text{for LH} \tag{9.2}$$

$$\mathrm{M}_{\mathrm{top}}^{\mathrm{DIL}} = 149 \pm 21_{\mathrm{stat}} \pm 5_{\mathrm{syst}}\ \mathrm{Gev/c^2}\ -\ \text{for SL} \tag{9.3}$$

To find the total systematic error e of the combined result, the combined systematic errors from the different sources have to be estimated first, as shown in Tables 9.3 and 9.4. Their correlations are taken into consideration with the use of the Best Linear Unbiased Estimator "BLUE" [63],[64],[65]. A covariance matrix is formed

$$\mathrm{S_{ij}} = \sum_{\mathrm{sources}} \sigma_{\mathrm{i}}\sigma_{\mathrm{j}}\rho_{\mathrm{ij}} \tag{9.4}$$

where $\sigma_i$ and $\sigma_j$ are statistical uncertainties in the corresponding systematic errors from the two channels due to all sources with the indexes i,j referring to the channels DIL or LJ. The $\rho_{ij}$ are the correlation matrices given by:

$$\rho_{\mathrm{ij}}^{\mathrm{signal}} = \rho_{\mathrm{ij}}^{\mathrm{P_T}} = \begin{pmatrix} 1 & 1 \\ 1 & 1 \end{pmatrix}\ \text{full correlation} \tag{9.5}$$

$$\rho_{\mathrm{ij}}^{\text{Bg scale}} = \rho_{\mathrm{ij}}^{\text{Bg shape}} = \begin{pmatrix} 1 & 0 \\ 0 & 1 \end{pmatrix}\ \text{uncorrelated} \tag{9.6}$$

We find e by minimizing:

$$\chi^2(\mathrm{e}) = \delta^{\mathrm{T}}(\mathrm{e})\mathrm{S}^{-1}\delta(\mathrm{e}) \tag{9.7}$$

where

$$\delta(\mathrm{e}) = \begin{pmatrix} e_{LJ} - e \\ e_{DIL} - e \end{pmatrix} \tag{9.8}$$

$e_{LJ}$ and $e_{DIL}$ are the total systematic errors in the LJ and DIL channel respectively.

From Equation 9.4 and the correlation matrices in Equations 9.5 and 9.6 the "combined" systematic errors are estimated for each source, shown in Tables 9.3 and 9.4.

| Source | $\delta M_{top}^{syst}$ (GeV/$c^2$) | $\delta M_{top}^{syst}$ (GeV/$c^2$) | $\delta M_{top}^{syst}$ (GeV/$c^2$) |
|---|---|---|---|
| | DIL (LH) | L+jets (SL) | Combined |
| Signal | 2.8±2.5 | 1.9±3.0 | 2.4 |
| $P_T$ scale | 1.7±0.2 | 1.0±0.7 | 1.7 |
| Background normalization | 0.2±0.0 | 2.7±1.5 | 0.2 |
| Background shape | 3.2±0.0 | 8.4±6.7 | 3.0 |
| Total | 4.6 | 9.3 | 4.5 |

Table 9.3: The systematic errors on the top mass for the lepton+jets (SL) and the dilepton (LH) channels as well as their combined error

| Source | $\delta M_{top}^{syst}$ (GeV/$c^2$) | $\delta M_{top}^{syst}$ (GeV/$c^2$) | $\delta M_{top}^{syst}$ (GeV/$c^2$) |
|---|---|---|---|
| | DIL (SL) | L+jets (SL) | Combined |
| Signal | 3.1±1.7 | 1.9±3.0 | 3.1 |
| $P_T$ scale | 1.7±0.2 | 1.0±0.7 | 1.7 |
| Background normalization | 0.8±1.2 | 2.7±1.5 | 0.8 |
| Background shape | 3.4±0.0 | 8.4±6.7 | 3.3 |
| Total | 5.0 | 9.3 | 4.9 |

Table 9.4: The systematic errors on the top mass for the lepton+jets (SL) and the dilepton (SL) channels as well as their combined error

Finally the total systematic error is:

$$e = 4.5 \pm 2.5 \text{ GeV/c}^2 \; - \; \text{for DIL/LH and LJ/SL} \tag{9.9}$$

and

$$e = 4.9 \pm 2.1 \; \text{GeV/c}^2 \; - \; \text{for DIL/SL and LJ/SL} \tag{9.10}$$

The total correlation between the DIL/SL & LJ/SL systematics is 33% whereas between the DIL/LH & LJ/SL systematics is 40%.

The combined $M_{top}$ result is obtained by minimizing:

$$\delta^{T}(M_{top})S^{-1}_{M_{top}}\delta(M_{top}) \tag{9.11}$$

where

$$\delta(M_{top}) = \begin{pmatrix} M^{LJ}_{top} - M_{top} \\ M^{DIL}_{top} - M_{top} \end{pmatrix} \tag{9.12}$$

The top mass covariance matrix is:

$$S_{M_{top},ij} = e^{stat}_{i} e^{stat}_{j} \rho^{stat}_{ij} + e^{syst}_{i} e^{syst}_{j} \rho^{syst}_{ij} \tag{9.13}$$

with the correlation matrices

$$\rho^{stat} = \begin{pmatrix} 1 & 0 \\ 0 & 1 \end{pmatrix} \text{ uncorrelated} \tag{9.14}$$

$$\rho^{syst} = \begin{pmatrix} 1 & 0.333 \\ 0.333 & 1 \end{pmatrix} \text{ for the DIL/SL and LH/SL} \tag{9.15}$$

$$\rho^{syst} = \begin{pmatrix} 1 & 0.405 \\ 0.405 & 1 \end{pmatrix} \text{ for the DIL/LH and LH/SL} \tag{9.16}$$

The systematic uncertainties related with the signal and the $P_T$ scale are estimated at the "nominal" mass $M_{top}$=175 GeV/$c^2$ [9]. On the other hand, the systematic uncertainties related with the background (normalization and shape) are independent

of the top mass, like the background itself. Therefore, all systematic uncertainties are independent of the top mass.

The statistical uncertainties, however, depend on the top mass [9]:

$$e_{stat} = \frac{P_T^{rms}}{\lambda\sqrt{N}} = \frac{\zeta + \xi M_{top}}{\lambda\sqrt{N}} \tag{9.17}$$

where $\lambda$ is the slope of the total (signal+background) $\langle P_T \rangle$ with respect to $M_{top}$, $P_T^{rms}$ is the total (signal+background) RMS $P_T$ and N is the total number of signal+background leptons in the data. Equation 9.17 holds for the SL method, but is also a valid approximation for the parabolic statistical error in $M_{top}$ from the LH method, as it has shown in this dissertation and in [9] that the two methods give consistent results and errors. The linear coefficients of $P_T^{rms}$ wrt $M_{top}$ are shown in Table 9.5 [9].

| Coefficient | L+jets | DIL |
|---|---|---|
| $\zeta$ (GeV/c) | 25.14 | 20.05 |
| $\xi$ | 0.03981 | 0.07565 |

Table 9.5: Coefficients of linear dependence of $P_T^{rms}$ on $M_{top}$: $P_T^{rms} = \zeta + \xi M_{top}$

In order to remove the bias towards the smaller (DIL) $M_{top}$ value imposed on the combined $M_{top}$, the formula 9.17 is applied to correct the statistical uncertainty for the mass dependence in each channel:

$$e'_{stat} = \frac{\zeta + \xi M'_{top}}{\zeta + \xi M_{top}} \times e_{stat} \tag{9.18}$$

where $M_{top}$ is the original measurement and $M'_{top}$ is the combined result. The combination with the corrected statistical uncertainties is repeated. The correction-

combination procedure is iterated 3 times, until it converges to a diagonal correlation matrix as shown in Tables 9.6 for the DIL/SL & LJ/SL combination and 9.7 for the DIL/LH & LJ/SL combination.

| Iteration | Statistical Error GeV/c$^2$ | Systematic Error GeV/c$^2$ | Total Error GeV/c$^2$ | $M_{top}$ GeV/c$^2$ | $\rho^{M_{top}}_{LJ,DIL}$ |
|---|---|---|---|---|---|
| 0 | 19.2001 | 4.89912 | 19.8051 | 160.605 | 0.0144337 |
| 1 | 19.3885 | 4.89912 | 19.8813 | 162.874 | 0.00065239 |
| 2 | 19.4826 | 4.89912 | 19.968 | 162.936 | 2.934e-05 |
| 3 | 19.4851 | 4.89912 | 19.9703 | 162.938 | 1.3174e-06 |

Table 9.6: Iterative BLUE results for the DIL/SL & LJ/SL combination.

| Iteration | Statistical Error GeV/c$^2$ | Systematic Error GeV/c$^2$ | Total Error GeV/c$^2$ | $M_{top}$ GeV/c$^2$ | $\rho^{M_{top}}_{LJ,DIL}$ |
|---|---|---|---|---|---|
| 0 | 18.4268 | 4.45623 | 18.9968 | 165.552 | 0.0170148 |
| 1 | 18.5742 | 4.45623 | 19.027 | 167.319 | 0.000746204 |
| 2 | 18.6443 | 4.45623 | 19.0902 | 167.363 | 3.2529e-05 |
| 3 | 18.6461 | 4.45623 | 19.0917 | 167.364 | 1.4178e-06 |

Table 9.7: Iterative BLUE results for the DIL/LH & LJ/SL combination.

The final results for the combined mass and its uncertainties are:

$$M_{top}^{comb} = 162.9 \pm 19.5_{stat} \pm 4.9_{syst} \text{ Gev/c}^2 \tag{9.19}$$

for the DIL/SL and LJ/SL

$$M_{top}^{comb} = 167.4 \pm 18.6_{stat} \pm 4.5_{syst} \text{ Gev/c}^2 \tag{9.20}$$

## 9.4 Search for lepton flavor asymmetry

In RUN I (110 pb$^{-1}$) and the early period of RUNII (193 pb$^{-1}$) there was an indication of a lepton flavor asymmetry. In RUN I there were 0 ee+$\mu\mu$ events and 7 e$\mu$ events, while in RUN II (193 pb$^{-1}$) there were 4 ee+$\mu\mu$ and 9 e$\mu$ events. A study was performed using those data events to examine if there is a possible lepton flavor asymmetry [66]. By combining the events in both RUNI and RUNII it was calculated that the probability to observe 4 ee+$\mu\mu$ and 16 e$\mu$ events when no asymmetry exists is about 2%. At that time that result indicated that there might actually be an asymmetry, while the statistics were still very low. This effect was very stimulating as it raised suspicions for physics beyond Standard Model.

It was, thus, natural to examine if this effect was still there for the much larger set of data corresponding to the, up to now, integrated luminosity of 1.8 fb$^{-1}$. In this luminosity there are 66 ee+$\mu\mu$ and 59 e$\mu$ data events. The Standard Model expectation gives 65.6±4.95 ee+$\mu\mu$ and 59.93±5.84 e$\mu$ events as seen from Table 5.1. If one forms the ratio:

$$\mathrm{R} = \frac{\mathrm{e}\mu}{\mathrm{ee} + \mu\mu} \tag{9.21}$$

it is seen that there is no evidence of flavor asymmetry. Deducting the estimated number of background events from the data the ratio R=1.13±0.24. For the Standard Model $t\bar{t}$ signal prediction R=1.17±0.11. The two ratios are the same within the uncertainties. The fact that they appear slightly larger that 1 can be explained from the fact that the ee+$\mu\mu$ events have smaller acceptance with respect to the e$\mu$'s because of the cuts that are applied to the same flavor events to remove the Drell-Yan

contamination.

# Chapter 10

## Summary

This study presents two independent and mutually compatible methods for measuring the top quark from the transverse momentum of the leptons in the dilepton channel. The Likelihood method exploits the full $P_T$ shape of the signal and the background spectra. The distributions are modeled by a Gamma×Fermi function and the top mass is estimated using the likelihood minimization procedure. The Straight Line method exploits only the mean $P_T$ of the combined signal and background distribution. The mass is estimated using the established linear relation between the mean $P_T$ and the top mass. The two methods have been used to estimate the top quark mass from 1.8 $fb^{-1}$ of run II data. The LH method gives $M_{top}$=156 GeV/$c^2$ and the SL gives $M_{top}$=149 GeV/$c^2$. The methods described give the possibility to combine the top mass measurements from the dilepton and the lepton+jets channels. Therefore, by combining the LH and SL dilepton results with the lepton+jets SL one, a top mass of $M_{top}^{comb}$ = 167.4 Gev/$c^2$ and of $M_{top}^{comb}$ = 162.9 Gev/$c^2$ is estimated respectively.

The statistical error of the dilepton measurement is ± 20 GeV and it is expected to be reduced to less than 10 GeV by the end of RUN II (Figure 10.1). The statistical

error can be further improved by combining the dilepton and the lepton+jets channels and is expected to go down to 5-6 GeV (Figures 10.2, 10.3). Incorporating a similar D0 measurement could further reduce the overall statistical error to 3-4 GeV.

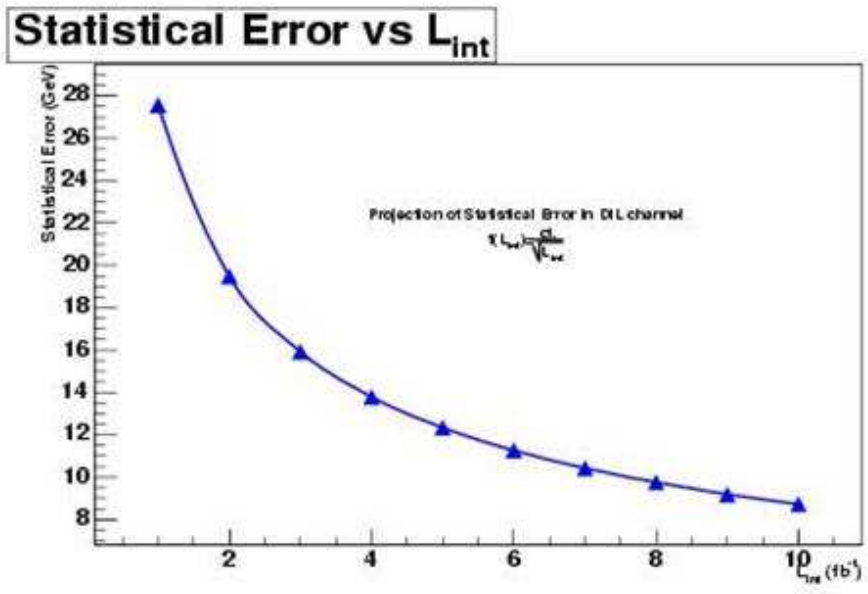


Figure 10.1: Projection of the statistical error as the integrated luminosity increases for the dilepton channel.

The total dilepton systematic error has been estimated to be 4.6 GeV and 5.0 GeV for the Likelihood and the Straight Line method respectively. The main contribution is due to the uncertainty of the Drell-Yan and Fakes shapes. As further refinements to the dilepton selection are planned, a better agreement between the Standard Model and data kinematic variables can be achieved. This will reduce the background shape systematic uncertainty. Furthermore, as new and more accurate Monte Carlo samples will be generated in the future, it is expected that also the signal driven systematics will be reduced. The refinements in the dilepton channel can reduce the systematic

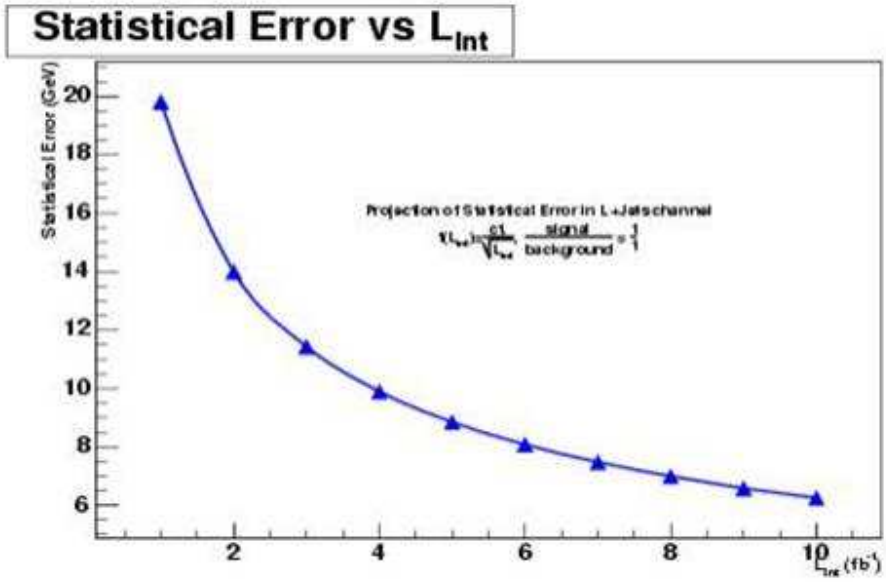


Figure 10.2: Projection of the statistical error as the integrated luminosity increases for the lepton+jets channel.

uncertainty to 2-3 GeV. The systematic error is also expected to be reduced in the lepton+jets channel to 2-3 GeV. Currently, in this channel, the major contribution is due to the fakes background whose estimation is greatly affected by the statistics [9]. Combining the two channels the systematic uncertainty can be reduced to 2 GeV. A possible combination of the CDF and D0 results, with this method, can give a total systematic of 1 GeV.

It should be reminded here that the advantage of this method is that it is not dependent on the jets, except from the cuts applied for the selection of the events. The top mass measurement does not carry therefore the jet energy scale uncertainty, that is presently the largest contribution for all other mass analysis. This analysis provides a very good preview of the accuracy that can be achieved with the LHC data. In LHC the $t\bar{t}$ cross section will be about 100 bigger and very soon there

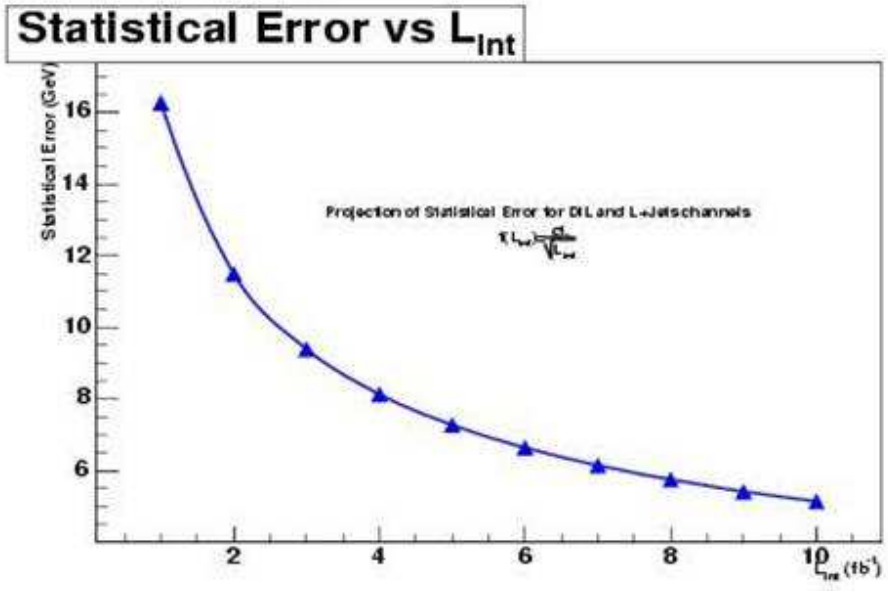


Figure 10.3: Projection of the statistical error as the integrated luminosity increases by combining the dilepton and the lepton+jets channels.

will be enough top pairs to make the statistical error insignificant with respect to the systematic. This method promises a very competitive or hopefully smaller systematic error with respect to the mass reconstruction methods.

Finally the LH top mass measurement of $M_{top} = 156 \pm 21$ GeV/c$^2$ has been included in the combined top mass measurement for the summer of 2007 (Figure 10.4). This includes three CFD dilepton measurements at 1.8 fb$^{-1}$, one CDF lepton+jets measurement at 1.7 fb$^{-1}$ and three D0 dilepton measurements at 1 fb$^{-1}$. The combined top mass result is $170.9 \pm 1.8$ GeV/c$^2$.

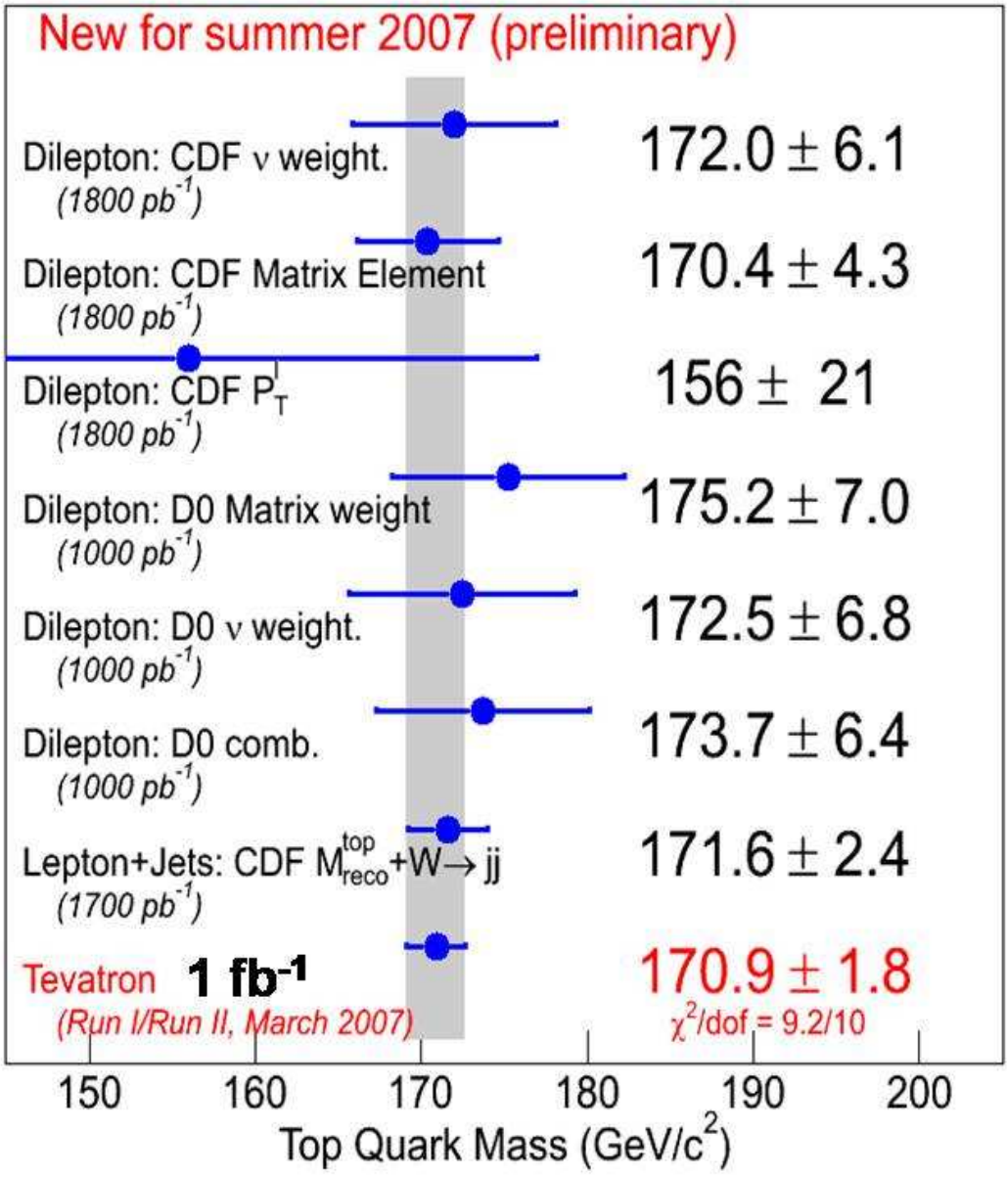


Figure 10.4: Top mass measurements at CDF and D0 measured the summer of 2007. The combined top mass is 170.9±1.8 GeV/$c^2$.

# Appendix A

## Appendix

| Input Mass (GeV) | Fitted Mass (GeV) | Pull | PullRMS | Residual (GeV) |
|---|---|---|---|---|
| 155 | 156.0490 ± 1.2321 | -0.0112 ± 0.0693 | 0.9543 ± 0.0513 | -0.2884 ± 1.5466 |
| 156 | 156.9040 ± 1.4427 | -0.0693 ± 0.0688 | 0.9052 ± 0.0452 | -1.3440 ± 1.4340 |
| 158 | 160.0100 ± 1.6969 | -0.0427 ± 0.0713 | 0.9675 ± 0.0515 | -1.2680 ± 1.7830 |
| 160 | 161.5780 ± 1.3399 | -0.1132 ± 0.0647 | 0.8958 ± 0.0463 | -2.7175 ± 1.3247 |
| 161 | 161.4690 ± 1.3140 | 0.0592 ± 0.0691 | 0.9381 ± 0.0515 | 1.0316 ± 1.4167 |
| 162 | 161.2850 ± 1.7164 | 0.0634 ± 0.0749 | 0.9859 ± 0.0514 | 1.8289 ± 1.5221 |
| 164 | 164.4410 ± 1.5467 | -0.0095 ± 0.0795 | 1.0364 ± 0.0785 | -0.5018 ± 1.6761 |
| 165 | 170.7550 ± 1.6981 | -0.1972 ± 0.0796 | 0.9689 ± 0.0627 | -3.3220 ± 2.0365 |
| 165.5 | 165.2880 ± 1.8519 | 0.0636 ± 0.0943 | 1.2007 ± 0.0749 | -0.4110 ± 1.9359 |
| 166 | 165.7160 ± 1.6443 | 0.0894 ± 0.0853 | 1.0780 ± 0.0822 | 1.9580 ± 1.5745 |
| 166.5 | 167.3990 ± 1.7573 | 0.0681 ± 0.0775 | 1.0518 ± 0.0583 | -0.5678 ± 1.9716 |
| 168 | 169.4770 ± 1.4795 | -0.0279 ± 0.0695 | 0.9458 ± 0.0549 | -1.2000 ± 1.6293 |
| 168.5 | 167.5280 ± 1.7158 | 0.0578 ± 0.0754 | 0.9893 ± 0.0535 | 0.7418 ± 1.7440 |
| 169 | 170.1580 ± 1.5042 | -0.0409 ± 0.0802 | 0.9586 ± 0.0546 | 0.4594 ± 1.6436 |
| 169.5 | 170.8120 ± 1.5732 | -0.0119 ± 0.0735 | 0.9728 ± 0.0531 | -3.3079 ± 1.7648 |
| 170.5 | 169.7510 ± 1.4288 | 0.0808 ± 0.0905 | 1.0977 ± 0.0795 | 2.3846 ± 1.9000 |
| 171 | 170.1700 ± 1.4336 | -0.0122 ± 0.0734 | 0.9123 ± 0.0800 | 1.1136 ± 1.4459 |
| 171.5 | 169.3850 ± 1.3902 | 0.1219 ± 0.0733 | 0.9740 ± 0.0508 | 4.0657 ± 1.4435 |
| 172 | 171.7200 ± 1.3904 | 0.0664 ± 0.0703 | 0.9644 ± 0.0503 | -0.4049 ± 1.5452 |
| 172.5 | 174.8070 ± 1.9793 | -0.0616 ± 0.0811 | 0.9800 ± 0.0502 | -2.8708 ± 1.8200 |
| 173 | 174.1240 ± 2.0960 | -0.0786 ± 0.0816 | 1.0739 ± 0.0735 | -1.7288 ± 2.1507 |
| 173.5 | 172.5510 ± 1.6280 | 0.0964 ± 0.0759 | 1.0015 ± 0.0564 | 0.3872 ± 1.6809 |
| 174 | 176.3900 ± 1.7906 | -0.0677 ± 0.0712 | 0.9793 ± 0.0513 | -2.3089 ± 1.7928 |
| 174.5 | 173.4290 ± 2.4371 | -0.0987 ± 0.0702 | 0.9447 ± 0.0489 | 4.1223 ± 1.7100 |
| 175 | 174.2130 ± 1.9661 | 0.0346 ± 0.0668 | 0.9242 ± 0.0470 | 2.7014 ± 1.8149 |
| 175.5 | 175.5630 ± 1.3115 | 0.0416 ± 0.0696 | 0.9583 ± 0.0552 | 1.2745 ± 1.4202 |
| 176 | 177.7160 ± 1.5589 | -0.0927 ± 0.0671 | 0.8946 ± 0.0511 | -1.0617 ± 1.5192 |
| 176.5 | 178.5850 ± 1.6535 | -0.0519 ± 0.0743 | 0.9787 ± 0.0585 | -3.0190 ± 1.7971 |
| 177 | 176.8130 ± 1.4858 | 0.0033 ± 0.0694 | 0.9282 ± 0.0507 | -2.2958 ± 1.7551 |
| 177.5 | 175.9870 ± 1.6275 | 0.1652 ± 0.0783 | 1.0120 ± 0.0531 | 2.3129 ± 1.9395 |
| 178 | 179.9650 ± 1.9049 | -0.0416 ± 0.0851 | 0.9748 ± 0.0554 | -2.3507 ± 2.1894 |
| 178.5 | 179.5860 ± 1.5568 | -0.0980 ± 0.0778 | 0.9867 ± 0.0684 | -1.3385 ± 1.5047 |
| 179 | 179.6040 ± 1.6992 | 0.0291 ± 0.0837 | 1.0395 ± 0.0833 | -0.5553 ± 1.8240 |
| 179.5 | 180.9720 ± 1.4796 | -0.0643 ± 0.0722 | 0.9338 ± 0.0502 | -3.7806 ± 1.7568 |
| 180 | 184.4130 ± 1.5808 | -0.1670 ± 0.0758 | 0.9854 ± 0.0790 | -1.8072 ± 1.5110 |
| 181 | 181.6770 ± 1.6706 | 0.0543 ± 0.0681 | 0.9437 ± 0.0442 | 1.3150 ± 1.6686 |
| 181.5 | 184.9070 ± 2.0342 | -0.1279 ± 0.0906 | 1.1130 ± 0.0870 | -2.2271 ± 2.1080 |
| 182 | 185.2490 ± 1.7776 | -0.1143 ± 0.0880 | 0.9628 ± 0.0757 | -2.7728 ± 2.0394 |
| 183 | 184.6970 ± 1.7099 | -0.0281 ± 0.0699 | 0.9198 ± 0.0504 | -4.2052 ± 1.7566 |
| 183.5 | 183.7810 ± 1.5109 | 0.0339 ± 0.0644 | 0.8965 ± 0.0483 | -0.2955 ± 1.5727 |
| 184 | 186.8400 ± 1.6615 | -0.1238 ± 0.0860 | 1.0713 ± 0.0822 | -2.3890 ± 1.8301 |
| 184.5 | 183.2110 ± 1.4455 | 0.0932 ± 0.0714 | 0.9456 ± 0.0546 | 1.8418 ± 1.6986 |
| 185 | 187.8750 ± 1.6444 | -0.0995 ± 0.0781 | 0.9994 ± 0.0749 | -2.8704 ± 1.7074 |
| 186 | 186.4260 ± 1.6727 | 0.0094 ± 0.0800 | 1.0273 ± 0.0759 | -0.3148 ± 1.9540 |
| 187 | 187.6070 ± 1.9482 | 0.0101 ± 0.0890 | 0.9716 ± 0.0635 | 0.2745 ± 1.8433 |
| 188 | 191.4780 ± 1.6813 | -0.1403 ± 0.0670 | 0.9130 ± 0.0558 | -3.0896 ± 1.7882 |
| 190 | 191.6170 ± 1.6372 | -0.0704 ± 0.0724 | 0.9310 ± 0.0486 | -2.8525 ± 1.6897 |
| 192 | 196.6550 ± 1.6517 | -0.2358 ± 0.0773 | 0.9943 ± 0.0786 | -3.3810 ± 1.8715 |
| 194 | 194.3880 ± 1.6782 | -0.0235 ± 0.0702 | 0.9661 ± 0.0582 | 1.1781 ± 1.6861 |
| 196 | 198.9440 ± 2.0457 | -0.1298 ± 0.0839 | 1.0705 ± 0.0814 | -2.3646 ± 2.0232 |
| 200 | 201.8240 ± 1.7645 | -0.0702 ± 0.0749 | 0.8923 ± 0.0562 | -1.3529 ± 1.9687 |

Table A.1: Mass estimation, pull and pullRMS values and residuals, as estimated from the 53 different mass samples after a gaussian fit to the corresponding distributions.

| input mass (GeV) | signal p | signal q | $< P_T^{fit} >$ (GeV) | $< P_T >$ (GeV) |
|---|---|---|---|---|
| 152 | 1.1426 | 20.4452 | 52.65 | 52.59 |
| 154 | 1.1371 | 20.6347 | 52.92 | 52.88 |
| 155 | 1.1343 | 20.7295 | 53.06 | 53.02 |
| 156 | 1.1315 | 20.8243 | 53.19 | 53.16 |
| 158 | 1.1259 | 21.0139 | 53.46 | 53.44 |
| 160 | 1.1204 | 21.2035 | 53.73 | 53.72 |
| 161 | 1.1176 | 21.2982 | 53.87 | 53.86 |
| 162 | 1.1148 | 21.3930 | 54.00 | 54.00 |
| 164 | 1.1092 | 21.5826 | 54.27 | 54.28 |
| 165 | 1.1065 | 21.6774 | 54.41 | 54.42 |
| 165.5 | 1.1051 | 21.7248 | 54.47 | 54.49 |
| 166 | 1.1037 | 21.7722 | 54.54 | 54.56 |
| 166.5 | 1.1023 | 21.8196 | 54.61 | 54.63 |
| 168 | 1.0981 | 21.9618 | 54.81 | 54.83 |
| 168.5 | 1.0967 | 22.0091 | 54.88 | 54.90 |
| 169 | 1.0953 | 22.0565 | 54.95 | 54.97 |
| 169.5 | 1.0939 | 22.1039 | 55.01 | 55.04 |
| 170.5 | 1.0912 | 22.1987 | 55.15 | 55.17 |
| 171 | 1.0898 | 22.2461 | 55.22 | 55.24 |
| 171.5 | 1.0884 | 22.2935 | 55.28 | 55.31 |
| 172 | 1.0870 | 22.3409 | 55.35 | 55.38 |
| 172.5 | 1.0856 | 22.3883 | 55.42 | 55.45 |
| 173 | 1.0842 | 22.4357 | 55.49 | 55.51 |
| 173.5 | 1.0828 | 22.4831 | 55.55 | 55.58 |
| 174 | 1.0814 | 22.5305 | 55.62 | 55.65 |
| 174.5 | 1.0800 | 22.5779 | 55.69 | 55.72 |
| 175 | 1.0786 | 22.6253 | 55.76 | 55.78 |
| 175.5 | 1.0772 | 22.6727 | 55.82 | 55.85 |
| 176 | 1.0759 | 22.7201 | 55.89 | 55.92 |
| 176.5 | 1.0745 | 22.7674 | 55.96 | 55.98 |
| 177 | 1.0731 | 22.8148 | 56.03 | 56.05 |
| 177.5 | 1.0717 | 22.8622 | 56.09 | 56.12 |
| 178 | 1.0703 | 22.9096 | 56.16 | 56.19 |
| 178.5 | 1.0689 | 22.9570 | 56.23 | 56.25 |
| 179 | 1.0675 | 23.0044 | 56.30 | 56.32 |
| 179.5 | 1.0661 | 23.0518 | 56.36 | 56.38 |
| 180 | 1.0647 | 23.0992 | 56.43 | 56.45 |
| 181 | 1.0619 | 23.1940 | 56.57 | 56.58 |
| 181.5 | 1.0605 | 23.2414 | 56.63 | 56.65 |
| 182 | 1.0592 | 23.2888 | 56.70 | 56.72 |
| 183 | 1.0564 | 23.3836 | 56.84 | 56.85 |
| 183.5 | 1.0550 | 23.4310 | 56.90 | 56.91 |
| 184 | 1.0536 | 23.4783 | 56.97 | 56.98 |
| 184.5 | 1.0522 | 23.5257 | 57.04 | 57.04 |
| 185 | 1.0508 | 23.5731 | 57.11 | 57.11 |
| 186 | 1.0480 | 23.6679 | 57.24 | 57.24 |
| 187 | 1.0452 | 23.7627 | 57.38 | 57.37 |
| 188 | 1.0425 | 23.8575 | 57.51 | 57.50 |
| 190 | 1.0369 | 24.0471 | 57.78 | 57.76 |
| 192 | 1.0313 | 24.2366 | 58.05 | 58.02 |
| 194 | 1.0258 | 24.4262 | 58.32 | 58.27 |
| 196 | 1.0202 | 24.6158 | 58.59 | 58.53 |
| 200 | 1.0091 | 24.9949 | 59.13 | 59.03 |

Table A.2: Estimation of the p, q parameters and estimation of the mean $< P_T^{fit} >$ from the integration the GammaxFermi Function, for the different top masses. The $< P_T >$ comes straight from the histograms.

# Bibliography


[1] F. Abe et al., "Observation of Top Quark Production in $p\bar{p}$ Collisions with the CDF Detector at Fermilab," *Phys. Rev. Lett. 74, 1995.*

[2] S. Abachi et al., "Observation of Top Quark," *Phys. Rev. Lett. 74, 1995.*

[3] Tevatron Electroweak Working Group, for the CDF and D0 Collaborations, "A combination of cdf and d0 results on the mass of the top quark," *hep-ex/0703034.*

[4] The CDF Collaboration, "Combination of top pair production cross section measurements with up to 760pb$^{-1}$," *CDF note 8148*, 2006.

[5] S. L. Glashow, "Partial symmetries of weak interactions," *Nucl. Phys., 22*, 1961.

[6] A. Salam and J. C. Ward, "Electromagnetic and weak interactions," *Phys. Lett., 13*, 1964.

[7] S. Weinberg, "A model of leptons," *Phys. Rev. Lett., 19*, 1967. p. 1264.

[8] N. Giokaris et al, "Probing the top quark mass in the dilepton and the lepton+jets channels using only lepton information," *JINR-E1-2005-104*, Jul 2005. 17pp.

[9] C. Vellidis et al, "Measurement of the top quark mass from the lepton transverse momentum in $t\bar{t} \rightarrow$ lepton+jets channel at the Tevatron," *CDFNote 8616.*

[10] D. J. Gross and F. Wilczek, "Asymptotically free gauge theories," *Phys. Rev., D8*, 1973. p. 3633.

[11] H. D. Politzer, "Asymptotic freedom: An approach to strong interactions," *Phys. Rept., 14*, 1974. p. 129.

[12] P. W. Higgs, "Broken symmetries and the masses of gauge bosons," *Phys. Rev. Lett., 13*, 1964. p. 508.

[13] R. Barate et al., "Search for the standard model higgs boson at lep," *Phys. Lett., B565*, 2003. p. 61.

[14] "First direct limit on the top quark lifetime," *CDF note 8104*, 2006.

[15] The CDF Collaboration, "Search for Electroweak Single-Top-Quark Production using Neural Networks with 955 pb-1 of CDF II data," *CDF note 8677*.

[16] The CDF Collaboration, "Multivariate Likelihood Search for Single-Top-Quark Production with 1.5fb-1," *CDF note 8964*.

[17] The CDF Collaboration, "Search for Single Top Quark Production in 955 pb-1 using the Matrix Element Technique," *CDF note 8588*.

[18] M. Cacciari et al., "The tt cross-section at 1.8 and 1.96 tev: A study of the systematics due to parton densities and scale dependence," *J. High Energy Phys., 0404*, 2004. p. 068. viii, xiii, 7, 8, 35.

[19] "The european physical journal c," *Review of Particle Physics, Vol. 15 Nov. 1-4 2000*.

[20] The CDF Collaboration, "A measurement of the $t\bar{t}$ cross section Using Dileptons," *CDF note 8103*.

[21] The CDF Collaboration, "Measurement of the cross section for $t\bar{t}$ production using event kinematics in $p\bar{p}$ collisions ar 1.96 TeV," *CDF note 8092*.

[22] Y. Kosukabe et al., "Measurement of the tt Production Cross Section in Vertex-Tagged Lepton+Jets Events," *CDF note 8110*.

[23] The CDF Collaboration, "Top Dilepton Cross Section in 1.2/fb using the DIL Selection," *CDF note 8802*, May 2007.

[24] The CDF Collaboration, "A measurement of the $p\bar{p} \rightarrow t\bar{t} \rightarrow b\bar{b}\ l^+\nu l^-\nu$ cross section in $1.1fb^{-1}$ using lepton + isolated track selection at 1.96TeV," *CDF note 8770*, June 2007.

[25] The CDF Collaboration, "A measurement of the $pp\bar{p} \rightarrow t\bar{t} \rightarrow b\bar{b}\ l^+\nu l^-\nu$ cross section in $1.1fb^{-1}$ using lepton + isolated track selection with identified b-jets at 1.96TeV," *CDF note 8912*.

[26] The CDF Collaboration, "Measurement of the ttbar production cross section in ppbar collisions at 1.96TeV using lepton+jets events with secondary vertex b-tagging," *CDF note 8795*.

[27] "Measurement of the top quark mass using the matrix element analysis technique in the lepton+jets channel with in-situ W→jj callibration," *CDF note 8375*.

[28] "http://www.fnal.gov/pub/news04/update_archive/update_9-10.html,"

[29] "http://www.fnal.gov/pub/news04/update_archive/update_10-1.html,"

[30] "http://www.fnal.gov/pub/news04/update_archive/update_10-15.html,"

[31] "The antiproton source rookie book,"

[32] "Tevatron rookie book,"

[33] "http://www-cdf.fnal.gov/,"

[34] F. Abe, et al. *Nucl. Instrum. Methods Phys. Res. A* **271***,387 (1988).*

[35] D. Amidei, et al. *Nucl. Instum. Methods Phys. Res. A* **350***, 73 (1994).*

[36] P. Azzi, et al. *Nucl. Instrum. Methods Phys. Res. A* **360***, 137 (1995).*

[37] "http://www-d0.fnal.gov/,"

[38] The D0 Collaboration, "The upgraded d0 detector," *Nucl.Instrum.Meth. A565 (2006) 463-537.*

[39] "The cdf ii detector, technical design report, fermilab-pub-96/390-e,"

[40] "http://www-cdf.fnal.gov/upgrades/silicon/cdf_runii_silicon.html,"

[41] S. Leone, "The intermediate silicon layers (isl) detector for the collider detector at fermilab, cdfnote 5129,"

[42] T. Affolder et al, "Cdf central outer tracker," *CDF note 6227.*

[43] K. Barkett, "Design and construction of the cdf central outer tracker," *CDF note 6227.*

[44] The CDF Collaboration, "The cdf central outer tracker," *CDF note 3944.*

[45] The CDF Collaboration, "A Time-of-Flight System form CDF," *CDF note 2573.*

[46] "http://www-cdf.fnal.gov/internal/upgrades/calorimetry.ps,"

[47] K. Anikeev et al, "EVB and Level3 for Aces," *CDF note 5793*, December 2001.

[48] Monica Tecchio, Victoria Giakoumopoulou, Naoki Kimura, Yuji Takeuchi, Dan Amidei, David Mietlicki, Chang-Seong Moon, Alexei Varganov, Hiromitsu Hatano, Andy Beretvas, "Top dilepton cross section in 2/fb using the DIL selection," *CDF note 8904*, July 2007.

[49] F .Abe et al., "Study of $t\bar{t}$ production in $p\bar{p}$ collisions using total transverse energy," *Phys. Rev. Lett, Vol. 75 Nov. 27 1995.*

[50] E. J. Thomson et al, "Top and Electroweak Event Classification Module for CDF RUN II," *CDF note 5947*, October 2003.

[51] www-cdf.fnal.gov/internal/dqm/goodrun/v17/goodv14.htm

[52] "http://www-cdf.fnal.gov/internal/physics/top/runiimc/topmc6/,"

[53] Torbjörn Sjöstrand, Leif Lönnblad, Stephen Mrenna, "Pythia 6.2 physics and manual," *hep-ph/0108264v1*.

[54] M.L. Mangano, M. Moretti, F. Piccinini, R. Pittau, A. Polosa, "Alpgen," *JJHEP 0307:001,2003, hep-ph/0206293*.

[55] R. Brun et al *CERN-DD-78-2-REV (unpublished)*.

[56] M. Tecchio et al, "Top Dilepton Cross Section Measurement using GEN5 DIL Selection," *CDF note 7851*, September 2005.

[57] G. Corcella, I.G. Knowles, G. Marchesini, S. Moretti, K. Odagiri, P. Richardson, M.H. Seymour and B.R. Webber, "Herwig 6.5," *JHEP 0101 (2001) 010 [hep-ph/0011363]; hep-ph/0210213*.

[58] Young-Kee Kim, Un-Ki Young, "Initial state gluon radiation studies on Drell-Young data for top-pair production in hadron collider," *CDF note 2573*.

[59] "http://www.phys.psu.edu/ cteq/cteq5table/,"

[60] "http://durpdg.dur.ac.uk/hepdata/mrs.html,"

[61] V. Giakoumopoulou, "Determination of the Lepton Et/Pt scale uncertainty from Z samples for the top quark mass studies," *CDF note 8632*.

[62] N. Giokaris, V. Giakoumopoulou, A. Manousakis-Katsikakis, C. Vellidis, "Top mass lepton+jets & dilepton combined result from the lepton $P_T$," *CDF note 8987*.

[63] Lyons L. et al. *NIM A270, 1988*.

[64] Lyons L. et al. *PRD 41, 3,1990*.

[65] Valassi A. *NIM A500, 2003*.

[66] V. Giakoumopoulou et al., "Evidence of lepton flavor asymmetry at high total transverse energy," *CDF note 6880*.